

The Jordan Journal of Earth and Environmental Sciences (JJEEES)

JJEEES is An International Peer-Reviewed Research Journal Issued by Higher Scientific Research Committee Ministry of Higher Education and Scientific Research and Deanship of Academic Research and Graduate Studies The Hashemite University.

EDITORIAL BOARD

Editor-in-Chief

Professor Abdul Rahim A. Hamdan
The Hashemite University

Editorial board

- **Professor Abdulkader M. Abed**
University of Jordan
- **Professor Hani N. Khoury**
University of Jordan
- **Professor Zuhair El-Isa**
University of Jordan

- **Professor Ahmad Abu Hilal**
Yarmouk University
- **Professor Sameh Gharaibeh**
Yarmouk University
- **Professor Issa Makhoul**
The Hashemite University

THE INTERNATIONAL ADVISORY BOARD

- **Prof. Sayed Abdul Rahman,**
Cairo University, Egypt.
- **Prof. Abdullah Al-Amri,**
King Saud University, Saudi Arabia.
- **Prof. Waleed Al-Zubair,**
Arabian Gulf University, Bahrain.
- **Prof. Ute Austermann-Haun,**
Fachhochschule und Lipp, Germany.
- **Prof. Ibrahim Banat,**
University of Ulster, UK.
- **Prof. Matthias Barjenbruch,**
Technisch Universitat Berlin, Germany.
- **Prof. Mohamed Boukhary,**
Ain Shams University, Egypt.
- **Prof. Mohammad El-Sharkawy,**
Cairo University, Egypt
- **Prof. Venugopalan Ittekkot.**
Center for Tropical Marine Ecology, Bremen,
Germany.
- **Prof. Christopher Kendall,**
University of North Carolina, U.S.A.
- **Prof. Elias Salameh,**
University of Jordan, Jordan.
- **Prof. V. Subramanian,**
Jawaharlal Nehru University, India.
- **Prof. Omar Rimawy,**
University of Jordan, Jordan.
- **Prof. Hakam Mustafa,**
Yarmouk University, Jordan.
- **Dr. Michael Crosby,**
The National Science Board, National Science
Foundation, Virginia, U.S.A.
- **Dr. Brian Turner,**
Durham University, U.K..
- **Dr. Friedhelm Krupp,**
Senckenberg Research Institute and Natural History
Museum, Germany.
- **Dr. Richard Lim,**
University of Technology, Australia.

EDITORIAL BOARD SUPPORT TEAM

Language Editor

Dr. Wael Zuraiq

Publishing Layout

MCPD. Osama AlShareet

SUBMISSION ADDRESS:

Professor **Abdul Rahim A. Hamdan**
Deanship of Academic Research and Higher Studies
Hashemite University, P.O. Box 330127, Postal Code 13133, Zarqa, Jordan.

Phone: +962-5-3903333 ext. 4151
E-Mail: jjees@hu.edu.jo , hamdan@hu.edu.jo



Hashemite Kingdom of Jordan



Hashemite University

Jordan Journal of
Earth and Environmental Sciences

JJEEES

An International Peer-Reviewed Scientific

Special Edition

<http://jjees.hu.edu.jo/>

ISSN 1995-6681

The Jordan Journal of Earth and Environmental Sciences (JJEES)

JJEES is An International Peer-Reviewed Research Journal Issued by Higher Scientific Research Committee Ministry of Higher Education and Scientific Research and Deanship of Academic Research and Graduate Studies The Hashemite University

Instructions to authors:

The Jordan Journal of Earth and Environmental Sciences (JJEES) is the national journal of Jordan in earth and environmental sciences. It is an internationally refereed journal dedicated to the advancement of knowledge. It publishes research papers that address both theoretical and applied valuable subjects and matters in both Arabic and English languages in the various fields of geoscience and environmental disciplines. JJEES is published quarterly by the Hashemite University. Submitted articles are blindly and rigorously reviewed by distinguished specialists in their respected fields. The articles submitted may be authentic research papers, scientific reviews, technical/scientific notes.

FORMATE GUIDE:

1. The research papers should be printed on one side of the paper, be double-line spaced, have a margin of 30 mm all around, and no more than 30 pages (7,500 words, font size 13). Authors should submit three copies of the paper and a floppy diskette 3.5 or a CD under (Winword IBM) or by e-mail. The title page must list the full title and the names and affiliations of all authors (first name, middle name and last name). Also, their addresses, including e-mail, and their ranks/positions must be included. Give the full address, including e-mail, telephone and fax, of the author who is to check the proof.
2. The research must contain the title and abstract, keywords, introduction, methodology, results, discussion, and recommendations if necessary. The system of international units must also be used. Scientific abbreviations may be used provided that they are mentioned when first used in the text. Include the name(s) of any sponsor(s) of the research contained in the paper, along with grant number(s).
3. Authors should submit with their paper two abstracts, one in the language of the paper and it should be typed at the beginning of the paper followed by the keywords before the introduction. As for the other abstract, it should be typed at the end of the paper on a separate sheet. Each abstract should not contain more than 200 words.
4. Captions and tables should be numbered consecutively according to their occurrence in the research with headings. When mentioned in the text, the same consecutive numbers should be used. Captions and tables must be typed on separate sheets of paper and placed at the end of the paper.
5. The author(s) should submit a written consent that he or she will not publish the paper in any other journal at the same time of its publication in JJEES. After the paper is approved for publication by the editorial board, the author does not have the right to translate, quote, cite, summarize or use the publication in the other mass media unless the editor-in-chief submits a written consent according to the policy of JJEES. Submitted material will not be returned to the author unless specifically requested.
6. **DOCUMENTATION:**

References:

- a. To cite sources in the text, use the author-date method; list the last name(s) of the author(s), then the year. Examples: (Holmes, 1991); (Smith and Hutton 1997).
- b. In the event that an author or reference is quoted or mentioned at the beginning of a paragraph or sentence or an author who has an innovative idea, the author's name is written followed by the year between two brackets. Example: Hallam(1990).
- c. If the author's name is repeated more than once in the same volume, alphabets can be used. Example: (Wilson, 1994 a; Wilson, 1994 b).
- d. Footnotes may be used to solve any ambiguity or explain something as in the case of a term that requires illustration. In this case, the term is given a number and the explanation is written in a footnote at the bottom of the page.
- e. If the number of authors exceeds two, the last name of the first author followed by et al. is written in the text. Example: (Moore et al.). Full names are written in the references regardless of their number.
- f. Prepare a reference section at the end of the paper listing all references in alphabetical order according to the first author's last name. This list should include only works that been cited.

Books:

Hunt, J. 1996. Petroleum Geochemistry and Geology. 2nd Ed., H. W. Freeman and Company, New York.

Chapter in a book:

Shinn E. A., 1983. Tidal Flat Environment, **In:** Carbonate Depositional Environments, edited by Scholle, P. A., Bebout, D. G., and Moore, C. H., The American Association of Petroleum Geologists, Tulsa, Oklahoma, U.S.A. pp. 171-210.

Periodicals:

Sexton, P. F., Wilson, P. A., and Pearson, P. N., 2006. Paleoecology of Late Middle Eocene Planktonic Foraminifera and Evolutionary Implication, *Marine Micropaleontology*, 60(1): 1-16.

Conferences and Meetings:

Huber, B. T. 1991. Paleogene and Early Neogene Planktonic Foraminifer Biostratigraphy of Sites 738 and 744, Kerguelen Plateau (southern Indian Ocean). In: Barron, J., Larsen, B., et al. (Eds.), Proceedings of the Ocean Drilling Program. Scientific Results, vol. 119. Ocean Drilling Program, College station, TX, pp. 427-449.

Dissertations:

Thawabteh, S. M. 2006. Sedimentology, Geochemistry, and Petrographic Study of Travertine Deposits along the Eastern Side of the Jordan Valley and Dead Sea, M. Sc. Thesis, The Hashemite University.

Unpublished:

Makhlouf, I. M. and El-Haddad, A. 2006. Depositional Environments and Facies of the Late Triassic Abu Ruweis Formation, Jordan, J. Asian Earth Sciences, England, in Press.

Illustrations:

- a. Supply each illustration on a separate sheet, with the lead author's name, the figure number and the top of the figure indicated on the reverse side.
 - b. Supply original photographs; photocopies and previously printed material are not acceptable.
 - c. Line artwork must be high-quality laser output (not photocopies).
 - d. Tints are not acceptable; lettering must be of reasonable size that would still be clearly legible upon reduction, and consistent within each figure and set of figure.
 - e. Electronic versions of the artwork should be supplied at the intended size of printing; the maximum column width is 143mm.
 - f. The cost of printing color illustrations in the Journal may be charged to the author(s).
7. Arranging articles in JJEES is based on the editorial policy.
 8. The author should submit the original and two copies of the manuscript, together with a covering letter from the corresponding author to the Editor-in-Chief.
 9. The editorial board's decisions regarding suitability for publication are final. The board reserves the right not to justify these decisions.
 10. In case the paper was initially accepted, it will be reviewed by two specialized reviewers.
 11. The accepted papers for publication shall be published according to the final date of acceptance.
 12. If the author chooses to withdraw the article after it has been assessed, he/she shall reimburse JJEES the cost of reviewing the paper.
 13. The author(s) will be provided with one copy of the issue in which the work appears in addition to 20 off prints for all authors. The author(s) must pay for any additional off prints of the published work.
 14. statement transferring copyright from the authors to the Hashemite University to enable the publisher to disseminate the author's work to the fullest extent is required before the manuscript can be accepted for publication. A copy of the Copyright Transfer Agreement to be used (which may be photocopied) can be found in the first issue of each volume of JJEES.
 15. Articles, communications or editorials published by JJEES represent the sole opinion of the authors. The publisher bears no responsibility or liability whatsoever for the use or misuse of the information published by JJEES.

Manuscript Submission:

Submit three copies of the manuscript (including copies of tables and illustrations) to the Editor-in-Chief

Professor **Abdul Rahim A. Hamdan**

Deanship of Academic Research and Higher Studies

Hashemite University, P.O. Box 330127, Postal Code 13133, Zarqa, Jordan.

Phone: +962-5-3903333 ext. 4151

E-Mail: jjees@hu.edu.jo , hamdan@hu.edu.jo

Submitted manuscript should not have been previously published or submitted for publications elsewhere while they are under consideration by JJEES. Research articles, communications, and technical notes are subject to critical review by competent referees. Manuscript submitted in Arabic should be accompanied by abstract and keywords in English.

Organization of the Manuscript:

The research papers should be printed on one side of the paper, be double-line spaced, have a margin of 30 mm all around, and no more than 30 pages (7,500 words, font size 13). Authors should submit three copies of the paper and a floppy diskette 3.5 or a CD under (Winword IBM) or by e-mail. The title page must list the full title and the names and affiliations of all authors (first name, middle name and last name). Also, their addresses, including e-mail, and their ranks/positions must be included. Give the full address, including e-mail, telephone and fax, of the author who is to check the proof.

The research must contain the title and abstract, keywords, introduction, methodology, results, discussion, and recommendations if necessary. The system of international units must also be used. Scientific abbreviations may be used provided that they are mentioned when first used in the text. Include the name(s) of any sponsor(s) of the research contained in the paper, along with grant number(s).

Copyright:

A statement transferring copyright from the authors to the Hashemite University to enable the publisher to disseminate the author's work to the fullest extent is required before the manuscript can be accepted for publication. A copy of the Copyright Transfer Agreement to be used (which may be photocopied) can be found in the first issue of each volume of JJEES.

Disclaimer:

Articles, communications or editorials published by JJEES represent the sole opinion of the authors. The publisher bears no responsibility or liability whatsoever for the use or misuse of the information published by JJEES.

Editorial Preface

It is my great pleasure to introduce the first special publication of the Jordan Journal of Earth and Environmental Sciences (JJEES), dealing with eight selected papers that have been presented in the International Conference on Materials in Jordan.

I have read the papers of this issue with lively interest, with real enjoyment, and with close attention and appreciation of its accurate and discreet coverage of materials in Jordan.

This special publication is intended to help the participants as well as colleagues in material sciences of different disciplines to work together on their common or interrelated problems and to use their work ideas and information presented at the conference. This document will be useful to many materials scientists.

Without the warm support and patient assistance of the editorial board this work could not have been completed. They cheerfully helped me in this publication.

Many special thanks go to Dr. Wael Zuraiq, the Dept. of English Language and Literature, who reviewed the language and MCPD. Osama Al-Shareet from the Computer Center, who prepared this special issue for the printer with great skill.

Editor-in-Chief,
JJEES,
Professor Abdul Rahim A. Hamdan,
Dept. of Earth and Environmental Sciences,
The Hashemite University,
Zarqa, Jordan.

Conference Preface

The International Conference on Materials in Jordan was held during the period from 4 - 6 March 2009 at the German / Jordanian University (GJU), Amman, Jordan (Humboldt Kolleg).

Preparation for the 1st International Conference on Materials in Jordan started on 12.4.2008 following the successful "Materials Workshop" held by the Jordanian Club of Humboldt Fellows (JCHF) at Goethe Institute/Amman which was followed by lectures in Jordan by the German Scientist Dr Nelia Wanderka from Berlin.

The efforts of HE Prof. Dr Khaled Toukan, chairman of Jordan Atomic Energy Commission (JAEC) who participated at the workshop, in addition to the efforts of Dr. Nelia Wanderka, were crucial to the success of the conference. The GJU joined the team of organizers; thus having a powerful team with a committee of 20 Jordanian scientists from various universities and research institutions. The efforts of the president of GJU Prof. Labib Khadra and its vice president (Humboldtian Prof. Dr. Ziad AlSaad) were extremely important to the success. Least and not last the executive committee members of JCHF Dr Ahmad Al Ajlouni and Dr. Lamia Khouri in addition to the dedication of other members of the club enabled holding a successful conference.

The valuable assistance by HE the ambassador of the German Embassy in Jordan Dr. Joachim Heidorn and the First Secretary and the Cultural Attachee of the Embassy Mr Carsten Fischer were valuable. The support of the Minister for Higher Education and Scientific Research (MoHESR), Secretary General of the Ministry Prof. Turki Obaidat combined with financial support from the "Scientific Research Support Fund/MoHESR, the Middle East Scientific Fund, Arab Potash Co, Jordan Ahli Bank" needed in addition to the crucial financial support from the Alexander von Humboldt Foundation enabled us to cover most of the financial expenses for the event. The conference co-hosting by Princess Sumaya University for Technology (PSUT) and the unlimited support extended by its president Prof. Hisham Gaseeb were important towards achieving the goals of the conference.

The conference was patronized by PM HE Eng. Nader Dahabi who deputized the Minister of Higher Education and Sci. Research Prof. Dr. Walid Maani in opening of the conference that was held at PSUT with the attendance of 279 people.

Important decisions emerged from the conference that include forming a committee for Int. Network to follow decisions and to continue the good work, to consider this conference as an important national and Int. event, to be the first and to be biannual conference. The Int. Committee was formed from: HE Prof. Khaled Toukan (Chairman, JAEC), Prof. Ziad Al Saad (VP of GJU, Jordan), Prof. Hani Houry (UJ, Jordan), Prof. Thomas Kelly (USA) Prof. Simon Ringer (Australia), Dr Nelli Wanderka (Germany), Prof. Jan Wastiels (Belgium), Nick Nugent (North Holland) Prof. Marwan S. Mousa , (Mu'tah Univ., Jordan).

Prof. Dr. Marwan S. Mousa
Director of ICMJ (Humboldt Kolleg)
President of the Jordanian Club of Humboldt Fellows
Dept. of Physics
Mu'tah University
Al-Karak, Jordan
email: mmousa@mutah.edu.jo , marwansmousa@yahoo.com

Conference Organizing Committee:

1. HE Prof. Dr. Khalid Toukan, Chairman of the Jordanian Atomic Energy Commission (Chairman of the Conference).
2. Prof. Dr. Labib Khadra, President of German Jordanian University GJU (Co-Chairman of the Conference).
3. Prof. Dr. Marwan S. Mousa, President of Jordanian Club of Humboldt Fellows (Director of the Conference).
4. Prof. Dr. Ziad Al Saad, Vice president GJU.
5. Dr Nelia Wanderka, Helmholtz-Center Berlin for Materials and Energy.

Conference Scientific Committee:

1. Prof. Dr. Hani Nicola Khouri, Jordan University
2. Prof. Dr. Mohammad El-Khateeb, Jordan University of Science and Technology
3. Prof. Dr. Tayel El-Hasan, Mu'tah University
4. Prof. Dr. Abdelaziz Khlaifat, Mu'tah University
5. Dr Khalid Al-Nawayseh, Arab Potash Co.
6. Dr Jamal Alali, Natural Resources Authority
7. Dr. Raed Ghanem, Al al-Bayt University
8. Dr. Mousa Gougazeh, Tafila Technical University
9. Prof. Dr. Ahmad M. Al-Ajlouni, Jordan University of Science and Technology
10. Dr. Yaseen Al-Sou'd, Al al-Bayt University
11. Dr Lamia El-Khouri, Yarmouk University
12. Prof. Dr. Sami Mahmood, Yarmouk University
13. Prof. Dr. Dia-Eddin Arafah, Jordan University
14. Prof. Dr. Akram Rousan, Jordan University of Science and Technology
15. Cyrus Salimi-Asl, DAAD Rep in Jordan
16. Dr. Ned Xoubi, Jordanian Atomic Energy Commission
17. Prof. Dr. Abdul Haleem Wreikat, Jordanian Atomic Energy Commission

Guest Editors:

Prof. Dr. Marwan S. Mousa marwansmousa@yahoo.com

Prof. Dr. Hani Khoury khouryhn@yu.edu.jo

Prof. Dr. Ziad Al-Saad zalsaad@Gmail.com

PAGES	PAPERS
38 – 49	Environmental Magnetism: Heavy Metal Concentrations in Soils as a Function of Magnetic Materials Content. <i>Tayel El-Hasan, Abdel-Jaleel Al-Nawiseh, Mahdi S. Lataifeh</i>
50 – 59	Heavy Metals Distribution in the Dead Sea Black Mud, Jordan <i>Kamal Momani; Tayel El-Hasan, Samer Auaydeh, Khaled Al-Nawayseh</i>
60 – 65	Exchange Coupling and Magnetic Properties of Fe/Ir(001) superlattices <i>B. Alqassem, B.A. Hamad, J.M. Khalifeh</i>
66 – 71	Associated Minerals and their Influence on the Optical Properties of Jordanian Kaolin <i>Akl M. Awwad, Rafat Ahmad, Hatem Alsyouri</i>
72 – 83	Mineralogy and Authigenesis of Zeolitic Tuff from Tall-Juhira and Tall Amir, South Jordan <i>Reyad A. Dwairi, Hani N. Khoury, Khalil M. Ibrahim</i>
84 – 95	Cementation of Silver Ions on Metallic Copper <i>Marian Jaskula</i>
96 – 107	Determination of crystallite thickness and crystal growth mechanisms of Jordanian clays by X-ray diffraction method. <i>I.M.Odeh, W.A.Saqqa, D.Eberl</i>
108 – 119	Adsorption of Thorium (IV) and Uranium (VI) by Tulul al-Shabba Zeolitic Tuff, Jordan <i>Mona Al-Shaybe and Fawwaz Khalili</i>

Environmental Magnetism: Heavy Metal Concentrations in Soils as a Function of Magnetic Materials Content.

Tayel El-Hasan *, Abdel-Jaleel Al-Nawiseh, Mahdi S. Lataifeh

Faculty of Science, Mu'tah University, 61710, P.O. Box (7), Mu'tah, Al-Karak - Jordan.

Abstract

The magnetic materials contained in the urban soil or roadside soils have become increasingly important as they could serve as good adsorbent media for the heavy metals such as Co, Cr, Cd, Pb, Zn and Ni. Usually, Fe-Oxides or hydroxides such as the magnetite, hematite and goethite are contained in the soil originated through natural or anthropogenic processes.

The results obtained in this investigation indicate the positive correlation between magnetic materials content and the heavy metals concentrations; and show that magnetite (Fe_3O_4) is the main magnetic mineral phase, which might be attributed to various anthropogenic sources mainly the traffic related activities. Recently, this finding has an important implication in monitoring the urban and roadside soil heavy metal pollution, which is developed into new concept called the environmental magnetism.

© 2009 Jordan Journal of Earth and Environmental Sciences. All rights reserved

Keywords: Magnetite, Urban soil, Heavy metals, Magnetic Proxies, Pollution, VSM.

1. Introduction

The first explicit description of environmental magnetism as a distinct field was reported by (Thompson & Oldfield, 1986). The environmental magnetism, a newly developing interdisciplinary trend, aimed to use the magnetic proxies as pollution indicator (Fassdinder et al. 1990; Morris et al. 1995; Versteeg et al. 1995; and Ptrovsky et al. 1999). The extent of this methodology was reviewed in details in (Oldfield et al. 1991; Versteeg et al. 1996; and Gautam et al. 2005).

Environmental magnetism has played an important role in understanding past climate change through studying of loess, lake and marine sediments magnetic properties (Waden, 2004). Furthermore, the environmental magnetism acts as a more rapid and non-destructive means of assessing pollution history of sediments (Brilhante et al. 1989, Foster et al., 1991, and Charlesworth & Lees, 2001). Moreover, Shilton et al., (2005) found positive relationship between magnetic contents and organic matter in dust samples.

Strzyszcz and Magiera, (1998) had investigated the correlation coefficient between magnetic susceptibility and heavy metal concentration in industrial areas. They showed that the magnetic susceptibility and the concentration of heavy metals in soil were in good correlation. Chalresworth and Lees (2001) reported a good correlation between heavy metal concentrations and magnetic proxies in Lake Core sediments. Good correlation was pointed out to exist between heavy metal

and the magnetic mineral characteristics (Beckwith et al., 1986; Rose and Bianchi-Mosquera, 1993; Hunt et al., 1995). Kim et al. (2007), noticed a positive significant correlation between enrichment index of the magnetic susceptibility ($\text{Ei } \chi$) and enrichment index of analyzed element ($\text{Ei } \text{metals}$), which confirmed the validity of use of magnetic proxies for heavy metal pollution.

Magnetic measurements were shown to be useful in investigating the atmospheric aerosols pollution, and source of pollution in many urban and industrial areas (Hoffman et al. 1999; Muxworthy et al. 2001; and Jordanov et al. 2003). Using the rapid and inexpensive environmental magnetism method, it is possible to obtain qualitative or semi-quantitative data on urban pollution, specially the magnetic susceptibility (Kim et al. 2007). Lu et al. (2005) showed that the magnetic properties and heavy metal content of automobile emission particulates resulted in significant positive correlations between the magnetic parameters and the contents of Pb, Cu and Fe. The magnetic measurements of various environmental materials, such as atmospheric particulates, roadside dust, soil, and vegetation, have successfully detected the source of pollution in many urban and industrial areas (Hoffman et al. 2003; and Jordanova et al. 2003).

Xia et al. (2001) suggested mixed contribution of magnetic materials from natural and anthropogenic sources; they confirmed the relationship between magnetic materials and pollution identification studies. Lu et al. (2005) showed that ferromagnetic materials were responsible for the magnetic properties of automobile emission particulates, and found that Cu, Pb, Cd and Fe are correlated with the magnetic particulates in automobile emissions.

The positive correlations between organic matter content of urban street dust and certain mineral magnetic

* Corresponding author. tayel@mutah.edu.jo;

properties were reported by (Shilton et al. 2005). In Jordan, the first attempt related to environmental magnetism implications was limited to motioning the roadside pollution using magnetic proxies (El-Hasan and Lataifeh, 2003; and El-Hasan, 2008). However, there are no previous studies in Jordan in using this implication to delineate the urban soil heavy metal pollution. The studied area was chosen as a known polluted area based on the results of (El-Hasan, 2002). The current work aimed to study the content and type of magnetic mineral phases in the urban soils of Sahab city, central Jordan, using two magnetic proxies, the initial magnetic susceptibility (χ_{in}) and the saturation magnetization (M_s). Moreover, this study aims to unravel the relationship between the heavy metals and magnetic parameters in soil samples and to determine the influences of the industrial activities in Sahab industrial city. Additionally, it aims to determine which magnetic proxies can be used as an effective environmental pollution probe, also to identify the magnetic mineral phases using the X-Ray Diffraction (XRD) technique. As well, to study the effect of grain size on the observed magnetic parameter, and to evaluate the environmental situation in accordance to the obtained results using the Index of Pollution (IP) and the categorization of samples based on their activities.

2. Study Area Settings

Sahab city is located in the central region of Jordan, 12 km to the east of the capital Amman (Fig. 1). It is of moderate topography with an altitude of around 700 m above sea level, and of moderate precipitation of around 250 mm/year. The soil of the study area is of Vertisol type, and the texture analysis shows that it has sandy clay; composed of sand 50%, clay 25% and silt 22% (El-Hasan, 2002)..

The study area is about 25 km² with 60,000 inhabitants. It compresses the Jordanian first and largest industrial estate King Abdullah the Second Industrial Estate (KAIE), which was established in 1980. It is located at the southeastern part of the study area (Fig. 1). It contains 365 firms with various types of industries such as engineering, chemical, pharmacological, food, plastic, rubber, and construction etc. Besides, an international highway and leading national roads crosses Sahab city.

The study area is dominated by Al-Hisa Phosphorite Unit (AHP) of Campanian-Mastrichitian age. It is 15 - 20 m thick, and consists of thin-bedded chert, white marl, chalky - marl, and phosphate (Fadda, 1991).

3. Sampling and Analytical Methods

A total of 56 samples were collected on a basis (500X500) grid across the whole city with a density of 9 samples per km², each soil sample was collected from upper soils (0-10 cm depth). The samples were collected during the period from January to April 2000. Each sample coordinate was delineated, using the GPS (Garmin GPS II Plus).

The samples extracted by taking 2g of soil sample (<2mm), then mixed with 25 ml of de-ionized water, vigorously shaken for 2 hours, and then centrifuged for an hour at 700 revolutions using Sorvall RC-5B Refrigerated

Super Speed Centrifuge (model GFL-3032). The solution was then transferred into 50 ml polyethylene bottles (Water extract). Residual was treated with 25ml of 0.01M HNO₃ and again shaken and centrifuged as in the previous step; the extract was decanted into 50 ml-polyethylene bottles (Acid extract). The soil pH and the electrical conductivity (EC) were analyzed by mixing 1:5 ratios of soil and de-ionized water.

Heavy metals were determined using Perkin Elmer AAS Analyst 300, with graphite furnace HGA 800, and autosampler AS 72. The analytical accuracy was monitored by using (Fluka Chemika) reference standard solution. The error for all analyzed elements was within 5% of the certified references.

Samples were sieved into sand size (63-150 μ m), and silt size (<63 μ m). The two different sizes samples were analyzed for their initial magnetic susceptibility χ_{in} and saturation magnetization M_s using Vibrating Sample Magnetometer (VSM). The VSM gives an indirect measure of the saturation magnetization (M_s) and the initial magnetic susceptibility χ_{in} . The parameters can be deduced from the initial magnetization curve with an applied magnetic field up to 10⁴ Oe. The VSM was also used to determine the magnetic phase from the shape of the hysteresis loops (Xia et al. 2008).

The measurements were made at room temperature (RT) in an applied magnetic field (H) up to 1 Tesla (Oe). The saturation magnetization M_s was determined by plotting M versus 1/H for each sample, and then extrapolating to 1/H equal zero. The intercept with the M - axis represents the M_s value, as shown Fig. (2a), and then the portion of M_s was recalculated to 1g samples. The initial magnetic susceptibility χ_{in} was calculated, using the following equations:

$$\chi_{in} = dM / dH \quad (1)$$

(Culity, 1972)

(χ_{in}) was deduced by calculating the slope of the line as H = zero and M = zero as shown in Fig. (2b). Then the portion of χ_{in} was recalculated to 1g sample.

The mineral constituents of the samples were determined using X-Ray Diffraction system (Philips-X'pert MpD) operating at 40 KV and 40 mA. Ten samples were pre-concentrated by separating the magnetic materials in each sample using ordinary magnet, then they were grinded till particle size became <63 μ m, and after that they were analyzed using the XRD. The fine powder samples were randomly mounted on special slides and then scanned between 2° and 65°, using Ni-filtered Co K- α radiation, divergent and scattering slits of 0.02° mm, a receiving slit of 0.15 mm, with stepping of 0.01° and scanning speed of 3°/min. For the M_s and χ_{in} heavy metals spatial distribution within the study area was graphically presented using computer program (Surfer, version 0.7).

4. Results and Discussion.

The total heavy metals (t-HM) were used as a measure for pollution, and represent the sum of the concentrations of (Fe, Mn, Cu, Co, Cr, Ni, Zn, Cd and Pb). The iron concentration, t-HM, magnetic susceptibility χ_{in} and saturation magnetization M_s in large and fine particles size

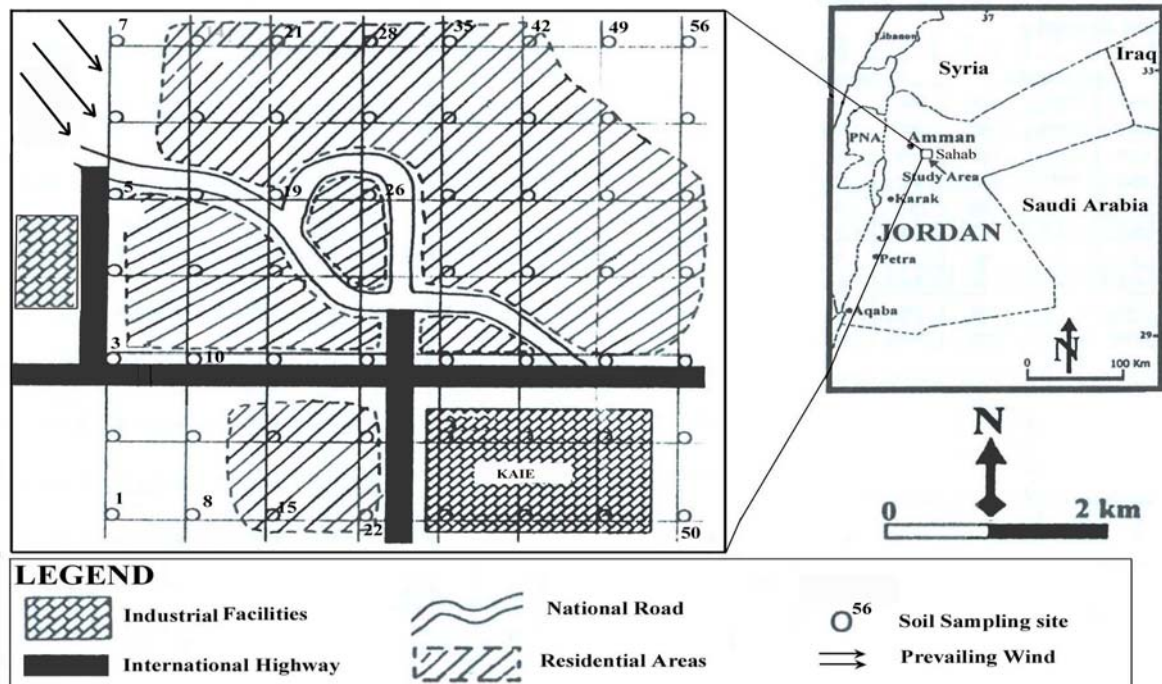


Fig. 1: Location map and sampling sites (after El-Hasan, 2008).

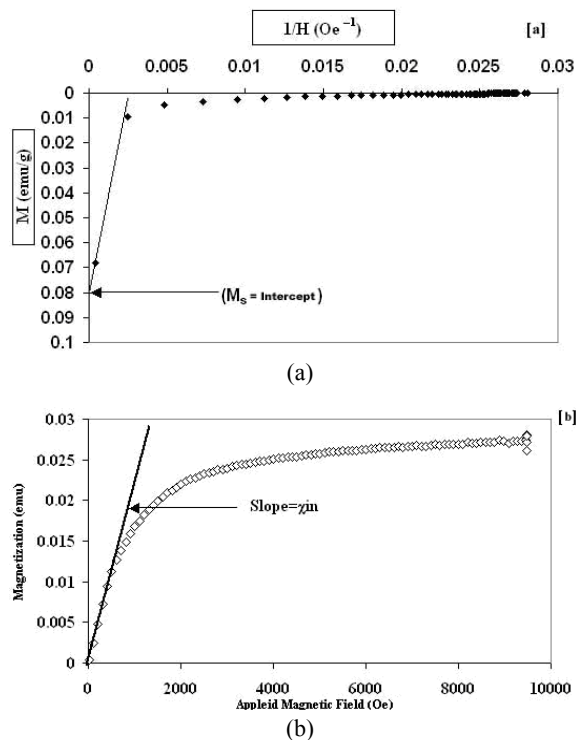


Fig. (2): a) M vs. $1/H$ plotting for a representative sample showing the determination of M_s values b) M vs. H plot for a representative sample showing how to calculate the initial magnetic susceptibility χ_{in} (slope of the bold line). (after El-Hasan and Lataifeh, 2003).

are presented in Table (1). Where the calculated results indicate the domination of the magnetic susceptibility over the saturation magnetization, which might be due to the fact that susceptibility represents the total contribution of ferromagnetic minerals (Dearing, 1999), while the saturation magnetization is only a measure of the magnitude of atomic magnetic moment.

4.1. Particle Size Effect

Many previous studies reported the dependence of the values of magnetic material concentrations on particle size (e.g. Heller et al., 1998; and Shi & Cioppa, 2006). Xia et al., (2001) has used the finest grain size ($< 63 \mu\text{m}$) in tracing street dust magnetic properties. Thomas (1987) pointed out that particles of size $< 2\text{mm}$ represent typical urban streams and soils, while (Forstner, 1983) indicated that those $< 63 \mu\text{m}$ represent the lake basin sediments. The current study has divided the studied sample sizes into two categories $< 63 \mu\text{m}$ and $> 63 \mu\text{m}$. Similar grain size categories were used by (Charlesworth & Lees, 2001).

By comparing the values of (χ_{in}) and (M_s) in Table (1), we noticed an increase in magnetic proxies values of the large size particles more than that for the fine size particles Fig. (3). This might be attributed to the fact that large size particles of greater than $63 \mu\text{m}$ in diameter have low degree of pedogenesis process, which is the main factor that causes the degradation and disintegration of the particles. The low degree of pedogenesis is usually caused by the low precipitation and lower chemical weathering rate. The average annual precipitation in the studied area does not exceed 250 mm/year with high evaporation rates (Fadda, 1991; and Department of Meteorology 2004).

Table (1): Values of studied parameters (χ_{in}) and (M_s), Fe and t-HM contents in samples for the two investigated particle sizes.

Sample No.	Fine size (< 63 μm)		Large size (> 63 μm)		t-HM (ppm)	Fe (ppm)
	χ_{in} (<i>emulg.Oe</i>) 10^{-5}	M_s (<i>emulg</i>)	χ_{in} (<i>emulg.Oe</i>) 10^{-5}	M_s (<i>emulg</i>)		
1	1.21	0.002	1.27	0.0025	8.8	6.3
2	0.90	0.002	1.46	0.0026	20.4	17.5
3	1.43	0.002	1.92	0.0027	32.8	28.6
4	1.83	0.002	1.65	0.0026	26.7	22.6
5	1.44	0.003	1.87	0.0028	76.5	71.5
6	1.25	0.002	1.28	0.0028	9.4	3.3
7	1.65	0.002	1.68	0.0023	15.8	13.8
8	1.56	0.004	1.31	0.0022	13.8	12
9	1.29	0.002	1.47	0.0028	9.8	7.3
10	1.73	0.002	2.37	0.0047	101	95
11	1.02	0.002	1.19	0.0021	8.0	3.4
12	1.42	0.003	1.49	0.0036	25.3	20.5
13	1.18	0.003	1.59	0.0025	9.9	7.6
14	1.38	0.002	1.87	0.0030	28.1	24.8
15	1.27	0.002	1.72	0.0026	22.1	18.8
16	1.40	0.002	1.24	0.0022	11.2	7.3
17	1.60	0.002	2.00	0.0030	53.2	46.4
18	1.36	0.003	1.44	0.0023	10.1	6.8
19	1.61	0.002	2.02	0.0030	48.2	42.6
20	1.52	0.002	1.72	0.0024	31.4	24.5
21	1.53	0.003	1.88	0.0030	37.0	32.4
22	1.35	0.002	1.34	0.0025	15.5	11.4
23	2.11	0.003	2.16	0.0041	89.2	82.9
24	1.07	0.002	1.57	0.0027	8.8	4.4
25	1.09	0.002	1.18	0.0023	8.7	4.4
26	1.27	0.004	1.59	0.0048	41.8	37.6
27	1.38	0.002	1.40	0.0019	18.4	13.5
28	1.31	0.002	1.38	0.0023	19.3	14.5
29	0.99	0.002	1.17	0.0018	24.6	21.1
30	1.56	0.003	1.60	0.0031	37.8	30.4
31	1.13	0.002	1.59	0.0026	15.3	8.6
32	1.35	0.003	1.41	0.0026	25.3	19.1
33	1.43	0.002	1.48	0.0024	20.8	14.6
34	1.32	0.003	1.35	0.0031	15.6	9.5
35	1.45	0.003	1.46	0.0029	39.0	34
36	0.88	0.002	1.23	0.0020	24.6	20.6
37	0.94	0.001	1.01	0.0015	6.5	4.5
38	1.10	0.002	1.29	0.0022	18.2	11.1
39	1.13	0.002	1.50	0.0027	21.8	17.6
40	0.91	0.001	1.14	0.0016	13.4	10.5
41	0.83	0.002	1.10	0.0025	20.9	16

Table 1 continues next page.....

42	1.04	0.002	1.45	0.0025	18.1	12.4
43	0.96	0.002	1.33	0.0017	18.5	13.9
44	1.44	0.002	1.47	0.0020	16.9	12.9
45	1.40	0.002	1.43	0.0025	24.6	19.8
46	1.44	0.002	1.45	0.0027	26.2	17.9
47	1.02	0.002	1.29	0.0023	16.1	11.4
48	1.14	0.002	1.38	0.0026	18.7	13.9
49	0.94	0.002	1.62	0.0031	16.8	11.9
50	0.88	0.002	1.67	0.0029	14.4	10.3
51	1.18	0.002	1.13	0.0019	14.5	11.8
52	1.67	0.002	1.75	0.0026	43	38.1
53	1.62	0.002	1.60	0.0026	24.2	18.4
54	0.90	0.002	1.29	0.0024	13.4	8.5
55	0.96	0.002	1.66	0.0026	23.5	19.6
56	0.90	0.002	1.33	0.0025	22.9	17.8
Average	1.28	0.0022	1.50	0.0026		
Max	2.11	0.0041	2.37	0.0048		
Min	0.83	0.0014	1.01	0.0015		
ST. Dev.	0.28	0.0005	0.28	0.00062		
Threshold	1.21	0.002	2.05	0.00384		

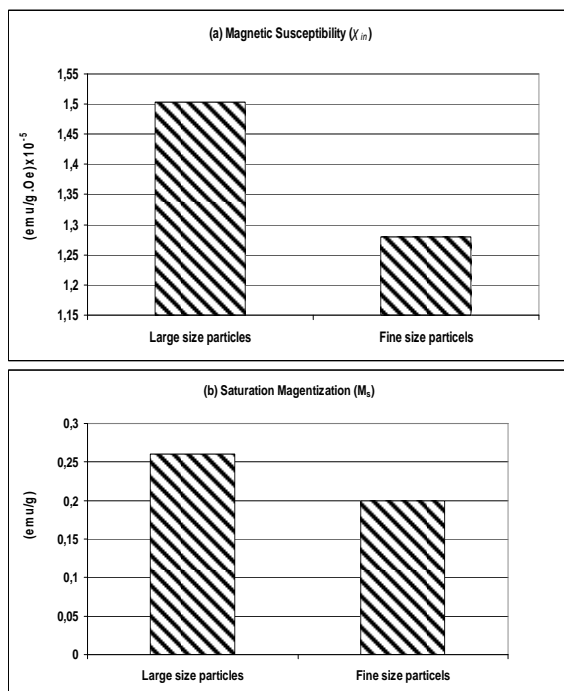


Fig. (3): Histogram showing the difference between the fine and large size particles in their contents of the (a) Magnetic susceptibility, and (b) Saturation magnetization.

Therefore, the climatic conditions would lower the pedogenesis as a result of lowering the chemical weathering rate. Similar results were reached by Kim et al., (2007) and El-Hasan, (2008). The effect of the post-depositional processes (diagenetic) or pedogenesis on the magnetic signal was recognized by (Hofmann et al. 1999).

The values of χ_{in} for large grain size particles range ($1.01 - 2.37 \times 10^{-5}$ emu/g.Oe) with an average of (1.5×10^{-5} emu/g.Oe). The value of M_s ranges from (0.0015 - 0.0048 emu/g) with an average of (0.0026 emu/g). The spatial distribution of χ_{in} and M_s are illustrated graphically in Figures (4 a & b).

According to data illustrated in Table (1) the values of initial magnetic susceptibility χ_{in} and the saturation magnetization M_s are higher in the following samples (3, 5, 10 and, 19), particularly the sample (19) is located at the center of the city and influenced by the highest density of traffic jam. Samples (3 & 5) are located at the international highway and the main entrance of Sahab city respectively, where both have a high traffic density. The sample (36) is located in the middle of King Abdullah II Industrial Estate (KAIE) that is affected by the industrial activity alone. However, it bears low values of both χ_{in} and M_s in large particle size (0.002 emu/g and 1.23×10^{-5} emu/g.Oe), respectively. This would indicate the influence of traffic as the prime source of magnetic pollution. Although, Kim et al. (2007) has found that industrial areas bear the higher magnetic concentrations, with intermediate concentrations in traffic area, the lowest concentrations were found in park areas.

4.2. Relationship between magnetic proxies and heavy metal distribution

The correlation coefficient was used in order to clarify the relationship between the magnetic proxies and heavy metal contents. The high correlation coefficient between the heavy metals concentration with the initial magnetic susceptibility (χ_{in}) and saturation magnetization (M_s) was obvious (Table 2). This table shows that the correlation coefficient between the t-HM and the initial magnetic susceptibility (χ_{in}) values are (0.77 - 0.59) for large and

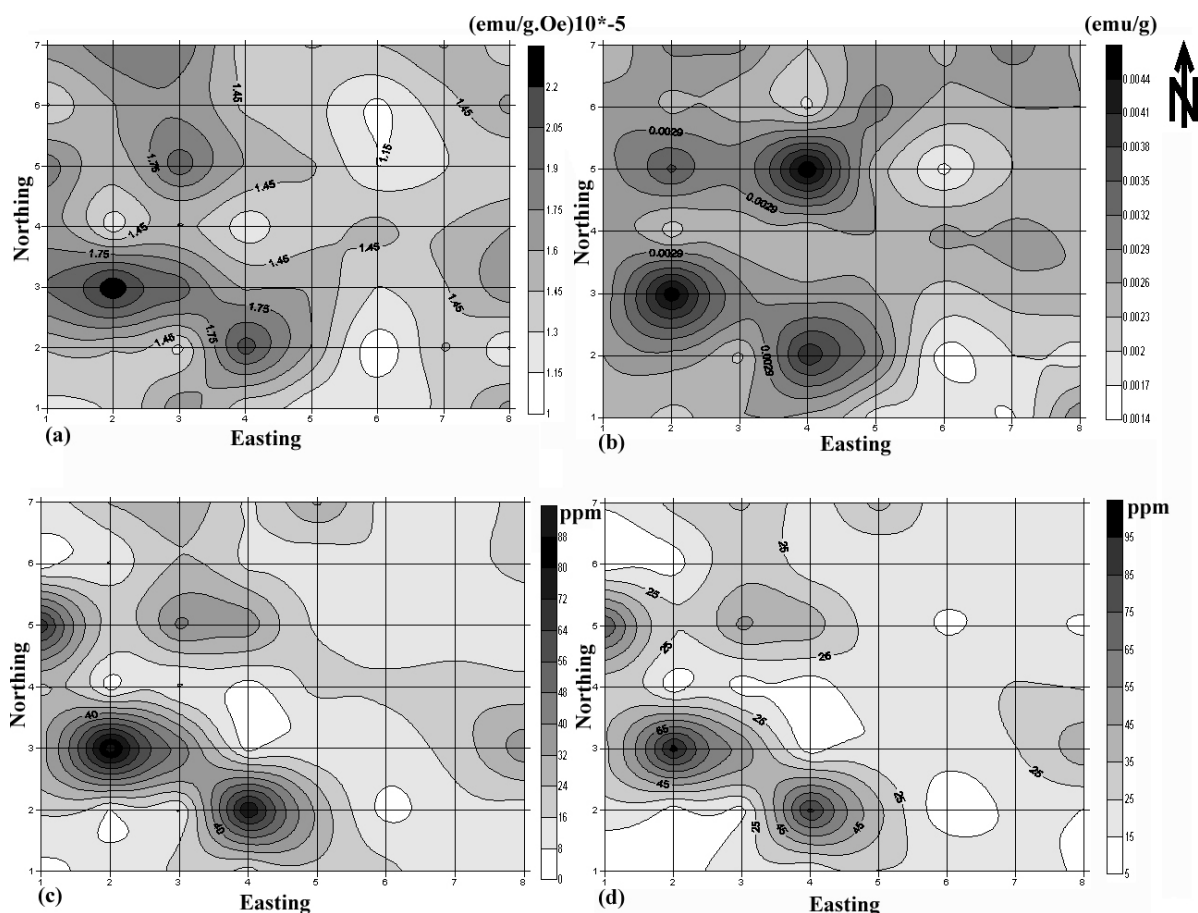


Fig. (4): Contour maps showing the distribution of studied parameters (a) Magnetic Susceptibility, (b) Saturation magnetization, (c) Fe, (d) Total heavy metal (t-HM).

Table 2. Correlation coefficient matrix for χ_{in} , M_s , t-HM and Fe in both fine and large particle size.

		Fine			
Large		χ_{in}	M_s	t-HM	Fe
	χ_{in}		0.50	0.59	0.59
	M_s	0.68		0.23	0.24
	t-HM	0.77	0.66		0.99
	Fe	0.77	0.66	0.99	

fine size particles, respectively. Whereas the correlation coefficient between the t-HM and the saturation magnetization (M_s) have the values (0.66 - 0.23) for large and fine size particles, respectively. Moreover, the correlation coefficient showed large difference between the two magnetic proxies; where the correlation between M_s and heavy metals is lower than the correlation between χ_{in} and heavy metals. This might be attributed to the fact that χ_{in} is the measure of the value of a respective quantity at the origin of the initial magnetization curve.

The distribution of all studied parameters (Fe, total heavy metals (t-HM), χ_{in} and M_s) are shown as contour maps using the Surfer 7.0 as illustrated in Fig. (4). There is an obvious correlation between the χ_{in} and M_s together with total heavy metals (t-HM) and iron (Fe). This is in agreement with the results obtained from correlation coefficient in Table (2). There are many previous studies that reached similar conclusions (e.g. Bityukova et al., 1999); they found the Ni, Cr, Zn, Cu, Pb and Mo are the

heavy metals that influenced the low field susceptibility (χ_i). In addition, the laboratory studies reveal that Fe-oxides particles in soil are highly adsorbing of heavy metals (Rose and Bianchi-Mosquera, 1993).

4.3. Magnetic mineral phases characterization

The magnetic materials contained in the samples of high magnetic susceptibility were pre-concentrated with ordinary magnet. A similar way of treatment was done by (Kim et al., 2007). The pre-concentrated samples were investigated using the X-ray diffractometer; the results showed that the magnetite is the main magnetic mineral phase (Fig. 5). The X-ray chart in figure (5) is for the sample (No. 23), which is located at a mixed area; where residential and traffic activities are usually intervening. This conclusion indicates the effect of anthropogenic origin of the magnetic pollutant materials, like the manufactured iron structures such as the vehicle structures

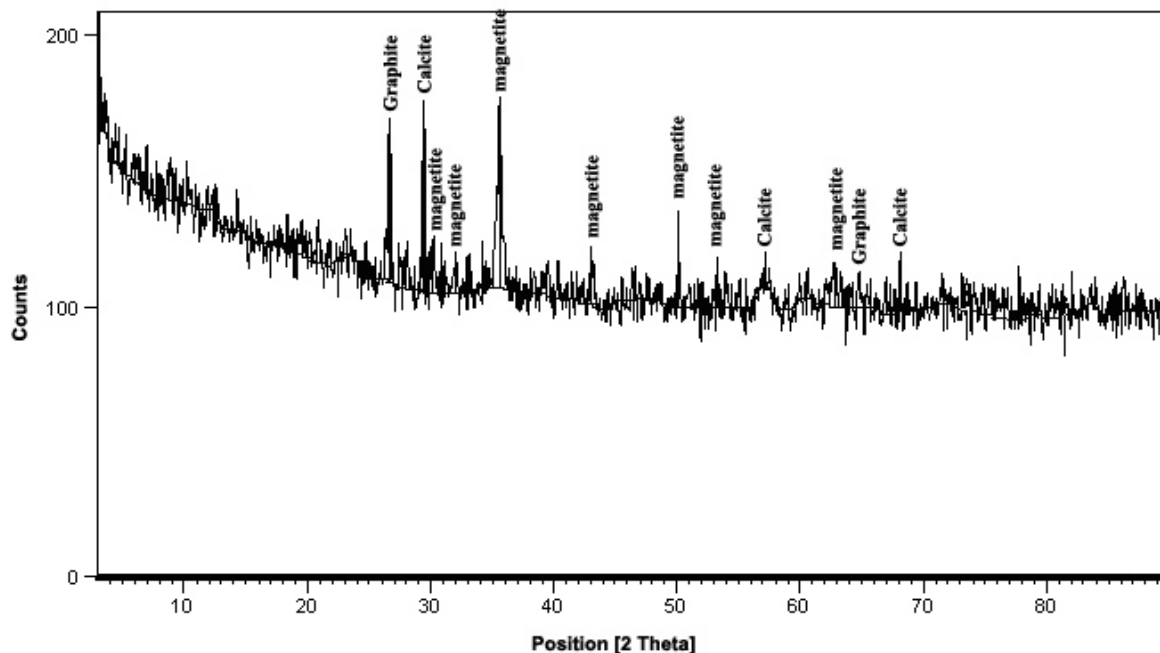


Fig. (5): X-Ray diffraction chart for selected soil sample, showing that magnetite is the main magnetic mineral phase.

which are mainly composed of magnetite-like materials (Kapicka et al. 2003). Shi & Cioppa, (2006) attributed small grain magnetic source to the construction debris or eroded river sediments whereas the larger magnetic particles are associated with industrial and traffic areas. Moreover, this result was reached by (Thomson and Oldfield, 1986). Hofmann et al., (1999) found the magnetite-like phase is the responsible for enhancement of magnetic signal in roadside soil whereas the natural magnetic materials are often composed of hematite and goethite (Xia et al. 2008). Gautam et al., (2004) reported that manufactured bricks and kilns used stable hematite and magnetite; similar results were also reported in (Hofmann et al., 1999; and Guatam et al. 2005). Furthermore, the hysteresis loop for the same sample (No. 23) shows a typical ferrimagnetic material with low coercive force (i.e. steep and narrow loops) as shown in Fig. (6), which confirms the presence of magnetite as the main magnetic mineral, such an observation was reported also by (Xia et al. 2008).

Shilton et al., (2005) found higher magnetite more than hematite in dust magnetic minerals. Moreover, Gautam et al. (2004) have found that magnetite is the dominant magnetic phase for typical road dust samples. Moreover, the magnetite presence in soil was attributed to be as a result of the pedogenesis (Banerjee, 2006).

4.4. Environmental aspects

The environmental implication of the obtained results shows that magnetic proxies can be used as environmental monitoring tools, for both natural and anthropogenic sources of pollution. The discrimination between lithological and anthropogenic influence on topsoil, using the magnetic susceptibility was successfully done by (Magiera et al., 2005). Therefore, the data were further treated using the index of pollution (IP).

The early-developed method of calculating the index of pollution (IP) of (Chester et al., 1985) was used. This

method was successfully used in evaluating the urban pollution in Karak city, central Jordan (El-Hasan and Jiries, 2000).

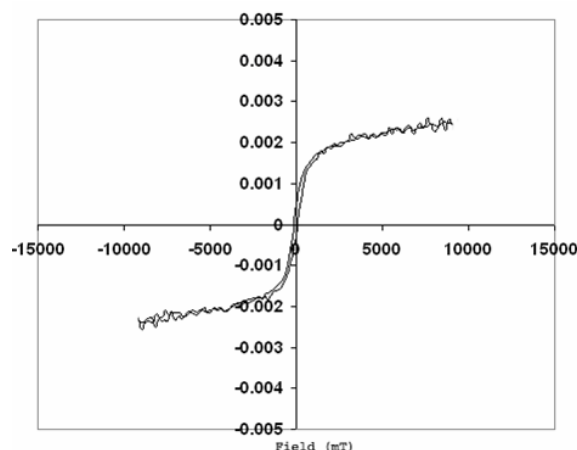


Fig. (6): Magnetic hysteresis loop of the topsoils from the study area of Sahab city.

This technique is based on assigning the ABS (Artificial Background Samples) in the sampling sites. The site numbers (9, 14, 24, 15 and 37) were chosen as the ABS due to their lowest concentration of heavy metals, and site numbers (37, 40, 41, 43 and 51) were chosen as the ABS due to their lowest concentration of magnetic proxies. Then the threshold for each element based on the ABS was calculated. The Index of pollution (IP) was then calculated by dividing the concentration of each element by the new threshold of the ABS of that element as follows:

$$\text{Threshold} = (X_{(ABS)} + 2 \sigma_{(ABS)}) \tag{2}$$

Chester et al., (1985).

$$\text{IP} = \text{Conc. E/Threshold} \tag{3}$$

Chester et al., (1985).

Where, $X_{(ABS)}$ is the average of elements in the ABS samples, and $\sigma_{(ABS)}$ is the standard deviation of each element of the ABS samples as shown in Table (3).

According to the data presented in Table (3), we notice the existence of a positive relationship between the IP for heavy elements and both the IP for the initial magnetic susceptibility χ_{in} , and the saturation magnetization M_s . Moreover, there was a clear positive significance correlation coefficient between the IP of both χ_{in} and M_s with the IP for total heavy metals (IP t-HM) and the IP for iron (IP Fe). The correlation significance was also higher in the large size particles (0.66, 0.77) between M_s and χ_{in} , respectively, rather than for fine size particles (0.24 and 0.59) between M_s and χ_{in} respectively as shown in Table 4.

The samples were categorized into four groups based on the dominating activities at each site. These groups are traffic (17 samples), industrial (11 samples), residential (20 samples) and the rest were considered as background (8 samples), which are the empty spaces. The averages of the χ_{in} , M_s , t-HM and Fe in both particle sizes are illustrated in Table 5.

Traffic samples bear the highest magnetic materials for both sizes, where the χ_{in} and M_s are $(1.66 \cdot 10^{-5} \text{ (emu/g.Oe)})$, 0.0029 emu/g and $(1.41 \cdot 10^{-5} \text{ (emu/g.Oe)})$, 0.0022 emu/g for large and fine particle, respectively. However, residential sites came in the second place followed by industrial, and finally the background sample (Fig. 7).

The traffic pollution was pointed out as the main source for magnetic pollution (Hoffmann et al., 1999; Lu, 2003 and Lu et al. 2005; and Guatam et al. 2005). Moreover, (Shilton et al. 2005) had reported the traffic related emissions enhancing strong magnetic signature.

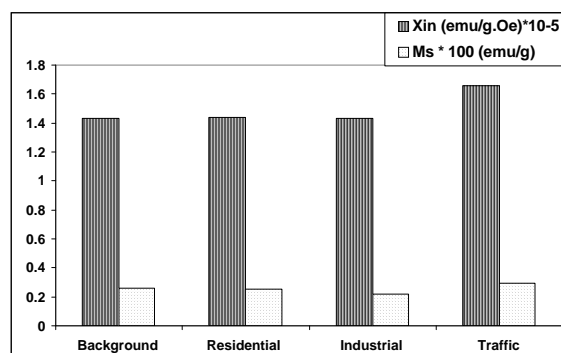
Using the magnetic susceptibility χ_{in} the enrichment series was as follows: Traffic > Residential > Industrial > Background, in both fine and large particle sizes. However, for the saturation magnetization M_s in large size particles it was: Traffic > Background > Residential > Industrial, whereas in fine particles there was no significant variation between the four categories (Table 5).

This would confirm that χ_{in} as well the large size particles exhibit more clearly magnetic signature than M_s and fine particles. And it indicates that the traffic areas have usually higher magnetic susceptibility. Although the background samples have the lowest magnetic concentrations, their concentrations have little difference from other categories (Table 5). This might be attributed to the fact that these samples are mainly composed of red

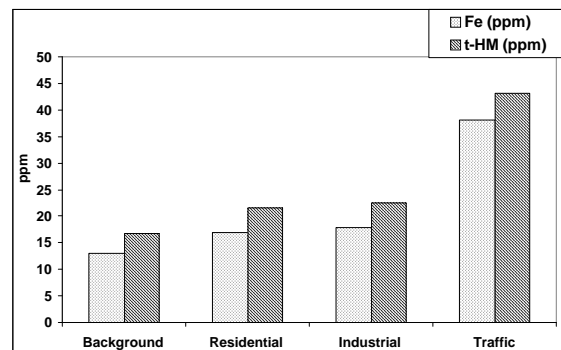
soils which normally have high Fe content. The analytical measurement of χ_{in} and M_s for these samples, using the VSM, usually measures not only the adsorbed magnetic materials (anthropogenic) but also the magnetic materials of natural origin inside the soil itself. This caused high magnetic signature in the background samples.

5. Conclusions

The magnetic proxies show a good correlation with heavy metals, and thus can be used as indicator for pollution; this correlation was evident from the IP results too. The magnetic susceptibility was better than saturation magnetization as pollution proxy indicator. The large grain size bears higher magnetic materials than smaller size, which can be attributed to the lack or low rate of pedogenesis. Traffic areas show higher magnetic pollution than other industrial and residential areas.



(a)



(b)

Fig. (7. a,b): Histogram showing the average values for all categories in a) Magnetic proxies, and b) Fe and t-HM.

Table 3. Index of pollution values for (χ_{in}) and (M_s), t-HM and Fe in the large size and fine size particles.

Sample	Fine particles		Large particles		IP t-HM	IP Fe
	IP- χ_{in}	IP- M_s	IP- χ_{in}	IP- M_s		
1	0.93	1.00	0.94	1.00	0.79	0.64
2	0.69	0.67	1.08	1.04	1.82	1.79
3	1.10	0.83	1.42	1.08	2.93	2.93
4	1.40	0.96	1.22	1.04	2.38	2.31
5	1.10	1.04	1.38	1.12	6.83	7.32
6	0.95	0.75	0.95	1.12	0.84	0.34
7	1.26	0.88	1.24	0.92	1.41	1.41
8	1.19	1.50	0.97	0.88	1.24	1.23
9	0.99	0.92	1.08	1.12	0.87	0.75
10	1.33	0.83	1.75	1.87	9.02	9.72
11	0.78	0.75	0.88	0.84	0.71	0.35
12	1.09	1.17	1.10	1.43	2.25	2.10
13	0.91	1.25	1.18	1.00	0.88	0.78
14	1.06	0.88	1.39	1.20	2.51	2.54
15	0.98	0.88	1.27	1.04	1.97	1.92
16	1.07	0.96	0.92	0.88	1.00	0.75
17	1.22	0.83	1.48	1.20	4.75	4.75
18	1.04	1.13	1.06	0.92	0.90	0.70
19	1.23	0.92	1.49	1.20	4.30	4.36
20	1.16	0.79	1.27	0.96	2.80	2.51
21	1.17	1.08	1.39	1.20	3.31	3.32
22	1.03	0.88	0.99	1.00	1.39	1.17
23	1.61	1.08	1.60	1.63	7.97	8.49
24	0.81	0.83	1.16	1.08	0.78	0.45
25	0.84	0.71	0.87	0.92	0.78	0.45
26	0.97	1.67	1.18	1.91	3.73	3.85
27	1.05	0.79	1.04	0.76	1.64	1.38
28	1.00	0.83	1.01	0.92	1.72	1.48
29	0.76	0.63	0.86	0.72	2.20	2.16
30	1.19	1.17	1.18	1.24	3.37	3.11
31	0.87	0.75	1.17	1.04	1.36	0.88
32	1.04	1.08	1.04	1.04	2.26	1.96
33	1.09	0.96	1.09	0.96	1.85	1.49
34	1.01	1.09	1.00	1.24	1.39	0.97
35	1.11	1.05	1.08	1.16	3.49	3.48
36	0.68	0.67	0.91	0.80	2.20	1.83
37	0.72	0.60	0.75	0.60	0.58	0.46
38	0.84	0.67	0.96	0.86	1.63	1.14
39	0.86	0.88	1.11	1.08	1.95	1.80
40	0.70	0.59	0.85	0.64	1.20	1.07
41	0.64	0.73	0.81	1.00	1.87	1.64
42	0.80	0.88	1.07	1.00	1.62	1.27
43	0.74	0.69	0.98	0.66	1.65	1.42
44	1.10	0.65	1.09	0.80	1.51	1.32
45	1.07	0.96	1.06	1.00	2.20	2.03
46	1.10	0.83	1.07	1.08	2.34	2.11
47	0.78	0.79	0.95	0.92	1.43	1.17
48	0.87	0.75	1.02	1.04	1.67	1.42
49	0.72	0.71	1.20	1.24	1.50	1.22
50	0.67	0.67	1.23	1.16	1.29	1.05
51	0.90	0.83	0.84	0.74	1.29	1.21
52	1.29	0.92	1.30	1.02	3.84	3.90
53	1.24	0.92	1.18	1.02	2.16	1.88
54	0.69	0.75	0.96	0.96	1.20	0.87
55	0.74	0.77	1.23	1.04	2.10	2.01
56	0.69	0.71	0.98	1.00	2.05	1.82

Acknowledgment

The authors are deeply thankful for Al-albayt University (Earth Science Institute) for their help in X-Ray Diffraction.

References

- [1] Banerjee, S.K., (2006): Environmental magnetism of nanophase iron minerals: Testing the biomineralization pathway. *Physics of the Earth and Planetary Interiors*. 154: 210-221.
- [2] Beckwith, P.R., Ellis, J.B., Revitt, D.M., Oldfield, F., (1986): Heavy metal and magnetic relationship for urban source sediment. *Physics of the Earth and Planetary Interiors*. 42: 67-75.
- [3] Bityukova, L., Scholgar, R., and Birke, M. 1999. Magnetic susceptibility as indicator of environmental pollution of soils in Tallinn. *Journal of Physics and Chemistry of Earth (A)*. 24(9): 829-835.
- [4] Brilhante, O., Daly, L., Trabuc, P., 1989. Application of magnetism to detect pollution caused by heavy metals in the environment. *C. R. Academic Science. Paris* 309 (II), 2005-2012.
- [5] Charlesworth S. M., Lees J. A. 2001. The application of some mineral magnetic measurements and heavy metal analysis for characterizing fine sediments in an urban catchment, Coventry, UK. *Journal of Applied Geophysics*. 48: 113-125.
- [6] Chester, R., Kudoja, W.M., Thomas, A., and Towner, J., (1985). Pollution reconnaissance in stream sediments using non-residual trace metals. *Environmental Pollution (Series B)*. 10. 213-238.
- [7] Dearing, J.A., Hannam, J.A., Anderson, A.S., Wellington, E.M.H. 2001. Magnetic, geochemical and DNA properties of highly magnetic soils in England. *Geophysical Journal International*. 144: 183 - 196.
- [8] Department of Meteorology, Jordan 2004. Annual Report. Unpublished report, Amman
- [9] El-Hasan, T. (2002): Urban Geochemistry: Heavy Metals Distribution on the Soils of Relatively Heavy Industrial City of Sahab, Central Jordan. *Mu'tah Lil-Buhuth wad-Dirasat*, Vol. 17 (3): 49-67.
- [10] El-Hasan, T. (2008): The Detection of Roadside Pollution of Rapidly Growing City in Arid Region Using the Magnetic Susceptibility and Saturation Magnetization as Proxies. *Environmental Geology*. 54(1):23-29.
- [11] El-Hasan, T.; and Lataifeh, M. (2003): Environmental magnetism: The implication of initial magnetic susceptibility and saturation magnetization for detecting roadside pollution in arid regions. *Dirasat, Pure Sciences*, 30(2): 191-2002.
- [12] Fadda, E., (1991): The geology of sahib area, map sheet No.3253 IV, NRA. Unpublished report, bulletin No. (17) Amman, Jordan.
- [13] Fassdinder, J.W.E., Stanjeck, H., and Vali, H. (1990): Occurrence of magnetic bacteria in soil. *Nature*, 343: 161-163.
- [14] Forstner, U., (1983) : Assessment of heavy metal pollution in rivers and estuaries. In: Thornton, I. (ED): *Applied Environmental Geochemistry*. Academic Press, London, pp. 395-423.
- [15] Foster, I, D, L., Charlesworth, S.M., Dearing, J.A., Keen, D.H., Dalgleish, H.Y., (1991): Lake sediment: a surrogate measure of sediment associated heavy metal transport in fluvial systems? *Sediment and Stream Water Quality in a Changing Environment: Trends and Explanation*, vol. 203, IAHS press, Wallingford, pp. 321-328.
- [16] Gautam, P.; Blaha, U.; and Appel, E. 2005. Magnetic susceptibility of dust-loaded leaves as a proxy of traffic-related heavy metal pollution in Kathmandu city, Nepal. *Atmospheric Environment*. 39:2201 -2211.
- [17] Gautam, P.; Blaha, U.; Appel, E.; and Neupane, G.; 2004. Environmental magnetic approach towards the quantification of pollution in Kathmandu urban area, Nepal. *Physics and Chemistry of the Earth*. 29(973 - 984)
- [18] Heller, F., Strzyszcz, Z., Magiera, T. 1998. Magnetic record of industrial pollution in forest soils of Upper Silesia, Poland. *Journal of Geophysical Research*. 103(B8): 767 - 774.
- [19] Hoffmann, V., Knab, M., and Appel, E. 1999. Magnetic susceptibility mapping of roadside pollution. *Journal of Geochemical Exploration*, 66: 31-326.
- [20] Hunt, C.P., Moskowitz, B.M., Banerjee, S.K., 1995. Magnetic properties of rocks and minerals. In: Ahrens, T.J. (Ed.), *Rock Physics and Phase Relations: a Handbook of Physical Constants*. American Geophysical Union (AGU) Publication, pp. 189 - 204.
- [21] Jordanova, N.V., Jordanova, D.V., Veneva, L., Yorova, K., Petrovsky, E. (2003): Magnetic response of soils and vegetation to heavy metal pollution—A case study. *Environmental Science and Technology*. 37: 4417 - 4424.
- [22] Kapicka, A., Jordanova, N., Petrovsky, E., and Podrazsky, V. (2003): Magnetic study of weakly contaminated forest soils. *Water, Air, and Soil Pollution* 148: 31 - 44.
- [23] Kim, W.; Doh, S.J.; Park, Y.H.; and Yun, S.T. 2007. Two-year magnetic monitoring in conjunction with geochemical and electron microscopic data of roadside dust in Seoul, Korea. *Atmospheric Environment*. 41:7627-7641.
- [24] Lu, S.G., (2003): *Chinese Soil Magnetism and Environment*. Higher Press, Beijing, China (in Chinese).
- [25] Lu, S.G., Qiang, H.B., Jing, C.I.A., and Xu, C. (2005) : Magnetic properties and heavy metal content of automobile emission particulates. *JZUS*. 8:731-735.
- [26] Magiera, T., Strzyszcz, Z., Kapicka, A., and Petrovsky, E., (2006): Discrimination of lithogenic and anthropogenic influences on topsoil magnetic susceptibility in Central Geoderma. 130: 299 - 311.
- [27] Morris, W.A., Versteeg, J.K., Bryant, D.W., Legzdins, A.E., McCarry, B.E., and Marvin, C.H. 1995. Preliminary comparisons between mutagenicity and magnetic susceptibility of respirable airborne particulate. *Atmospheric Environment*. 29: 3441-3450.
- [28] Muxworthy, A.R., Matzka, J., Petersen, N., (2001): Comparison of magnetic parameters of urban atmospheric particulate matter pollution and metrological data. *Atmospheric Environment*. 35 : 4379 - 4389.
- [29] Oldfield, F. 1991. Environmental magnetism – a personal prospective. *Quaternary Science Review*. 10: 73-85.
- [30] Oldfield, F., Richardson, N., (1990): Lake sediment magnetism and atmospheric deposition. *Philosophical Transactions of the royal society of London B* 327:325-330.
- [31] Petrovsky, E. Kapicka, A. Jordanova, N. Knab, M. and Hoffmann, V. 1999. Low-field magnetic susceptibility: a proxy method of estimating increased pollution of different environmental systems. Submitted to *Environmental Geology*.

- [32] Rose, A., and Bianchi-Mosquera, G.C., (1993) : Adsorption of Cu, Pb, Zn, Co, Ni, and Ag on goethite and hematite: a control on metal mobilization from red beds into stratiform copper deposits. *Economic Geology*. 188: 1226 - 1236.
- [33] Shi, R., Cioppa, M.T., 2006. Magnetic survey of topsoils in Windsor-Essex County, Canada. *Journal of Applied Geophysics*. 60: 201-212.
- [34] Shilton, V.F.; Booth, C.A.; Smith, J.P.; Giess, P.; Mitchell, D.J.; and Williams, C.D. 2005. Magnetic properties of Urban street dust and their relationship with organic matter content in the west midlands, UK. *Atmospheric Environment*. 39:3651-3659.
- [35] Strzyszczyk, Z. and Magiera, T. (1998): Heavy metal contamination and magnetic susceptibility in soils of Southern Poland, *Phys. Chem. Earth*. 23(9-10): 1127 - 1131.
- [36] Thomas, M.C., 1987. Channel sedimentation within the urbanized River Thame, UK. *Regul. Rivers. Research Management*. 1 : 229-246.
- [37] Thomson, R., Oldfield, F., 1986. *Environment Magnetism*. George Allen and Unwin, London. PP 354.
- [38] Versteeg, J.K., Morris, W.A., and Rukavina, N.A. 1995. The utility of magnetic properties as a proxy for mapping contamination in Hamilton Harbor sediment. *Journal of Great Lake Research*. 21: 71-83.
- [39] Versteeg, J.K., Morris, W.A., and Rukavina, N.A. 1996. Distribution of contaminated sediment in Hamilton Harbor as mapped by magnetic susceptibility. *Geoscience Canada*. 22 (4): 145-151.
- [40] Waden, J. (2004): Book review: Heller et al. (2003): *Environmental magnetism: principles and application of environmental magnetism*. *Quaternary Science Review*. 23: 1876-1870.
- [41] Xia, S., Dearing J.A., Boyle, J.F., Bloemendal, J., Morse, A. P., 2001: Association between magnetic properties and its implications. *Journal of Applied Geophysics*. 48: 83-92.
- [42] Xia, D.S., Chen, F.H., Bloemendal, J., Liu, X.M., Yu, Y., and Yang, L.P. (2008): Magnetic properties of urban dustfall in Lanzhou, China, and its environmental implications. *Atmospheric Environment* 42 (2008) 2198 – 2207.

Heavy Metals Distribution in the Dead Sea Black Mud, Jordan

Kamal Momani ^a; Tayel El-Hasan ^{a,*}, Samer Auaydeh ^a, Khaled Al-Nawayseh ^b

^aDepartment of Chemistry, Mu'tah University, 61710, Al-Karak – Jordan.

^bArab Potash Company; P.O. Box (1470), Amman - Jordan.

Abstract

The concentrations of trace metals (Fe, Mn, Ni, Zn, Co, Cr, Cu and Pb) were investigated in the Dead Sea black mud and river sediments in the northern basin of the Dead Sea region, Jordan. The pH of the mud was slightly above 8 while it was around 6 for the seawater. All analyzed heavy metal content in the black mud, except Pb, was less than their contents in other types of mud. This might be due to the effect of the mildly acidic pH of seawater, which would enhance the metal solubility or incorporation within salt mineral structure, rather than precipitation. The sequential extraction results showed that Ni and Co transferred into the carbonate fraction, Mn is found mostly as manganese-iron oxide, and the residual phase contained Cr, Cu, Fe and Pb. This study illustrated that the black mud had low heavy metal contents, thus indicating low toxicity. Additionally, it shows insignificance effect of the mixing of freshwater with seawater on the heavy metal contents in the black mud.

© 2009 Jordan Journal of Earth and Environmental Sciences. All rights reserved

Keywords: Dead Sea, Black mud, Sequential extraction, Heavy metals, Jordan.

1. Introduction

The Dead Sea is one of the most famous sites for climatotherapy. It is the lowest point on earth at 422 m below Sea level; its level is declining with rate equal to 1m/year, and evaporation rate is equal to 0.5 cm/day (APC, 2007). The Dead Sea is among the saltiest water bodies on the earth, its salinity reaches 340 g/kg compared with oceans 35 gkg⁻¹ (Al-Nawayseh, 2003).

The Dead Sea is only 35 km west of Amman and 30 km east of Jerusalem; it is located in the middle of Jordan rift valley region, extending from north to south along Wadi Araba and Jordan River (Oumeish, 1996). The Dead Sea is as old as the history of Jordan and Palestine. It was mentioned in the world Old Testament and the Holy Koran, the Dead Sea was given many names for example, Sedom, dragon Araba, Asphalt Sea and Lutt Sea (Oumeish, 1996). It is 28 million years old; and is divided into two lakes: the northern lake comprises 76% of the whole Sea with a maximum depth of 360 m, and the southern one comprises 24% of whole Sea and it is 10 m deep, the two lakes are separated by the Lisan Island, the total length of the Sea is 67 km, and the width ranges from 12 to 17 km, the total surface area is 1000 km² (Abdel-Fattah, 1997).

The Dead Sea is the lowest lake in the world, and it is considered the saltiest one among all the hyper saline lakes of the world. The chemical composition of the Dead Sea brines are Potassium Chloride which consists of 1.2 % (weight/weight) or (w/w) of the brine salt, Magnesium

Chloride 14.5%, Sodium Chloride 7.5%, Calcium Chloride 3.8% and Magnesium Bromide 0.5% (Es-Shahat et al., 2003). These chemicals provide the raw materials for fertilizers, salts and cosmetic products. Abdel-Fattah and Nicholas (2009) studied the toxic element contents in the natural black mud of the Dead Sea that is used in cosmetics production. They found no toxic enrichment of elements either in the raw mud or its derivative products.

The climate in the Dead Sea area is characterized by it is hot dry summer season, with mean temperature about 33 °C. In winter the temperature is pleasant, with average temperature 16.8 °C. The maximum temperature is 40.6 °C in July, the hottest month, while the minimum temperature is 10.8 °C in January, the coldest month. The average relative humidity ranges from 40.6% to 44.3% in summer and from 59% to 63.3% in winter season. Rainfall is very low with an annual rainfall of 70 mm (Al-Nawayseh, 2003).

The atmosphere over the Dead Sea is rich in oxygen 10% more than any other seas, which might be due to its lower altitude. Water evaporation is relatively low because the dissolved salts lower the vapor pressure over the sea surface (Oumeish, 1996). The geology of the investigated area is controlled by the Rift valley, which is a continuation of the East African Rift valley and the Red Sea and began during the Eocene-Oligocene age (Powell, 1988).

The Dead Sea represents a rich source of black mud, which is used in climatotherapy for many skin diseases (Oumeish, 1996). The Dead Sea black mud was used as facial masks and skin curative since ancient times (Abdel-Fattah and Schultz-Makuch, 2004). Therefore, it is essential to evaluate its chemical feature, especially heavy metal content.

* Corresponding author. tayel@mutah.edu.jo

A previous study, dealing with the Dead Sea mud geochemistry and mineralogical features in four places along the eastern shore, has found that the level of trace elements in the Dead Sea mud was less than those in any other sea mud and its composition was 40% of the total mud is carbonate, 20% is clay, 5% feldspar, 25% quartz, 6% pyrite and 0.7 % organic matter (Abdel-Fattah, 1997).

Abdel-Samie et al., (2004) studied the groundwater and the surface water of the Dead Sea area especially in Wadi Issal, Mazra'a area, Es-Safi area and Wadi Ibn Hammad. They found that the surface water has low salinity 700 mg/L, but the groundwater has a higher salinity 569 mg/L - 2266 mg/l. Also high level of nitrate was noticed in Es-Safi and Mazra'a. Furthermore, and they found that the surface and groundwater resources of the Dead Sea were not highly contaminated with heavy metals except for Fe and Mn. Al-Nadaf, (1992) found that the levels of trace elements (Zn, Cd, Cu, Co, Cr, Ba, Sr, Pb, and Ni) in soil of Kitim-Nueimeh, north Jordan valley; were higher than the average soil values, and in some cases exceed the maximum tolerable limits, which is attributable to using large quantities of nutrients and heavy traffics.

A study on the physiography, structure, stratigraphy, paleo-limnology, water, and sediments of the Dead Sea has illustrated many interrelationships between geology, chemistry, and limnology (Neev and Emery, 1967). Moreover, another study indicated that the sulfate-reducing bacteria is present in the reducing bottom sediments of the Dead Sea and that they were the most probable source of the dissolved sulfide in the bottom water (Nissebaum, 1969).

This work aims to determine the concentration of heavy metals in the Black mud and their spatial distribution along the eastern shore of the Dead Sea. The physiochemical parameters of the black mud such as pH, EC, and organic matter (OC) were used to study the heavy metal distribution profiles. Furthermore, the sequential extraction technique was used to investigate the distribution of heavy metals and the chemical forms in which those elements might be associated in the black mud. Finally, the mixing of fresh and salty waters and its effect on the black mud composition was studied too.

1.1. Study area settings

The Dead Sea is located in the center part of the Jordan rift valley and consists of two basins, the northern basin (a longer and deepen one) and the southern basin (a smaller and shallow) (Abed, 1985). The southern basin had completely dried out and exposed through pumping of the brine to the Potash factories. The northern basin contains the hotels and tourism sites. Therefore, the investigated area concentrates on the eastern shore of the Dead Sea northern basin, where the black mud and the main streams supply the Dead Sea by freshwater, Fig. (1). Particularly, this study covered the area between Swiemah in the north to the Lisan Island in the south, passing through three sources of fresh water: Swiemah, Zarqa - Ma'en and Wadi Al-Mujeb, Fig. (1).

2. Materials and Methodology

2.1. Sampling collection and preparation

A total of 30 samples of black mud were collected in the summer of 2005 from different sites on the eastern shore of the Dead Sea starting from Swiemah to the Lisan Island passing through three sites of mixing with fresh water. These sites are Swiemah, Zarqa - Ma'en and Wadi Al-Mujeb.

The mud samples had been collected from the area covered with the Dead Sea water, ranging from 1-3 meters off-shore. Another 4 samples were collected from outside the sea; they are covered only by freshwater Fig. (1). The samples were collected from 5 cm deep at the mud/water interface. The sample sites were separated by about one kilometer from each other. The samples were characterized in detailed descriptive procedure including: location of mud sample, depth, color, smell, etc. The electrical conductivity (EC) was measured by conductivity meter (WTW, LF-320, Weilheim, Germany) and was calibrated by using 0.01 M KCl at 25°C. The seawater pH was measured on sites by using glass electrode pH meter (WTW, pH 523, Weilheim, Germany) that was calibrated based on pH 5 and pH 9 at 25°C, all these data are presented in Table (1).

The collected samples of black mud were stored in polyethylene bags and carried to the laboratory, where they air-dried for two days and stored in Polyethylene bags in cold and dark place. The mud pH values were determined by treating the mud with de-ionized water (soil-to-water ratio = 1:2.5) that was equilibrated over night (Abul-Kashem and Singh 1999).

2.2. Analytical methods

One gram of each black mud sample was accurately weighted, then dried in an oven at 105 °C for 12 hours to reach constant weight in order to determine the moisture content. The weight loss was calculated based on the difference between the final and the initial weights. The same samples were burned in furnace at a 550 °C for 4 hours to determine the organic matter content in the form of Loss On Ignition (LOI), which then was calculated gravimetrically based in the weight difference (Preer et al., 1980).

The collected samples of black mud were stored in polyethylene bags and carried to the laboratory, where they were air-dried for two days and were stored in Polyethylene bags in cold and dark place. The mud pH values were determined by treating the mud with de-ionized water (soil-to-water ratio = 1:2.5) that was equilibrated over night (Abul-Kashem and Singh 1999).

2.2.1. Heavy metals extraction

One gram of the mud sample was digested with 15 ml of high purity concentrated HNO₃ by using a 50 ml Polyethylene test tube. The mixture was heated to 95°C for 2 hours by using a water bath, ultrasonicated for 30 minutes at 80°C, then was filtered by Whatman pre-washed filter paper (45 µm) with 1% HNO₃. Then sample was diluted into a 25 ml Polyethylene volumetric flask with 1% HNO₃. Heavy metals (Mn, Pb, Cu, Co, Zn, Cr, Ni and Fe) were analyzed by using a Flame Atomic Absorption Spectrophotometer (FAAS) model Spectra

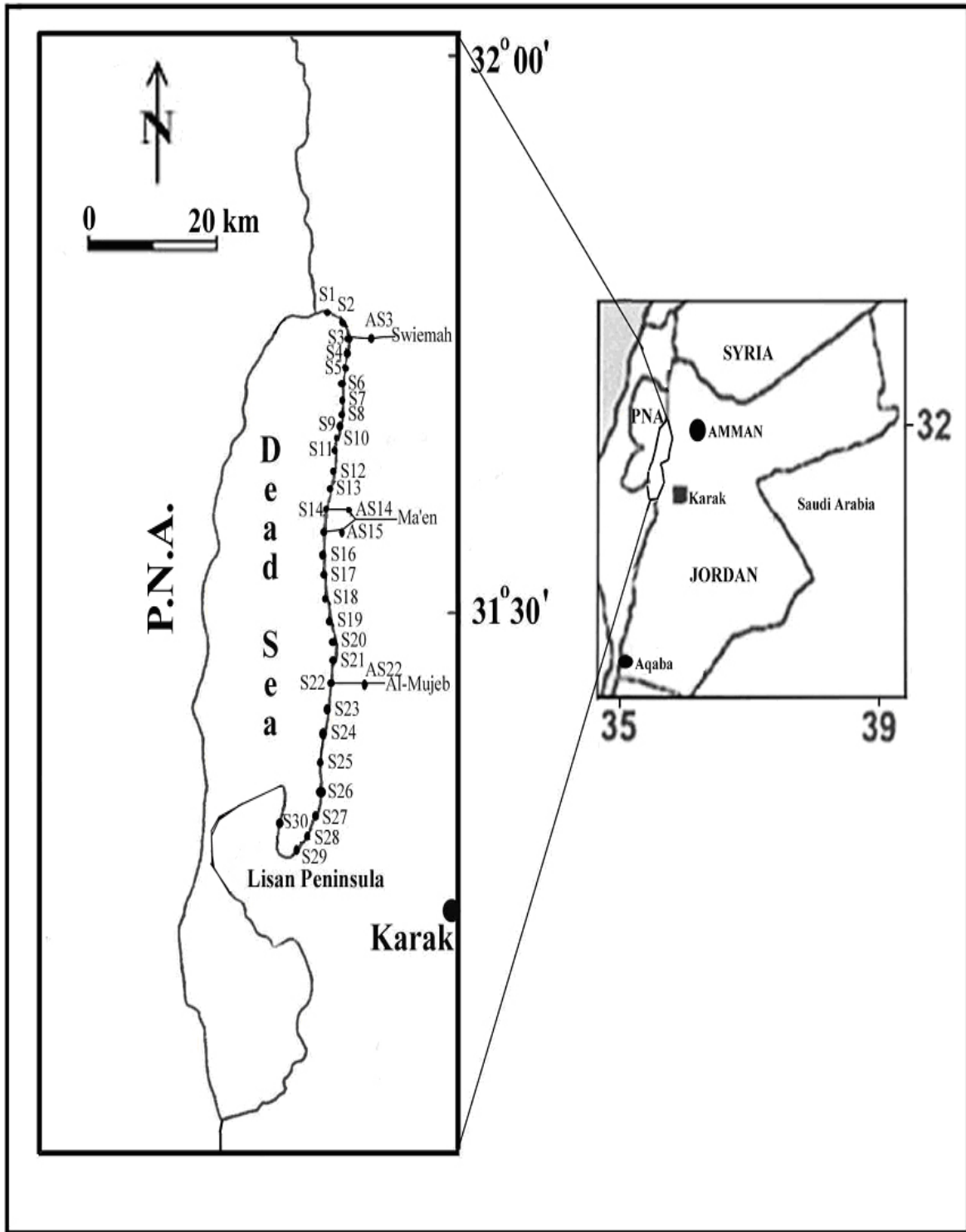


Figure (1): Location map of the study area showing the two basins of the Dead Sea and the samplings sites.

Table 1. Black mud description, location, depth, pH and EC parameters.

Sample	Location	Mud Description color, odor	pH water	EC water (mS/cm)	pH Mud
S1	Salt	Black – bad odor	6.01	180.3	8.05
S2	Salt	Black – bad odor	5.97	181.4	7.80
S3	Mixing	Black – bad odor	6.04	185.7	7.95
AS3	Fresh	White – bad odor	6.97	26.5	7.80
S4	Salt	Black – bad odor	5.92	180.8	8.08
S5	Salt	Black – bad odor	6.03	186.9	8.25
S6	Salt	Black – bad odor	6.05	163.4	8.24
S7	Salt	Black – bad odor	6.05	180.0	8.13
S8	Salt	Black – bad odor	6.04	180.1	7.85
S9	Salt	Black – bad odor	6.05	181.9	8.04
S10	Salt	Red – bad odor	5.91	180.7	7.98
S11	Salt	Black – bad odor	6.02	180.5	7.83
S12	Salt	Black – bad odor	6.28	188.5	7.73
S13	Salt	Black – bad odor	5.95	188.0	7.93
S14	Mixing	White – bad odor	5.94	180.6	8.51
AS14	Fresh	White – bad odor	6.94	10.19	8.31
S15	Mixing	Black – bad odor	5.96	180.7	8.24
AS15	Fresh	White – bad odor	6.84	38.9	8.24
S16	Mixing	Black – bad odor	5.97	180.7	8.02
S17	Salt	Black – bad odor	5.95	181.6	8.03
S18	Salt	Black – bad odor	5.94	181.3	7.99
S19	Salt	Black – bad odor	5.94	180.6	7.83
S20	Salt	Black – bad odor	5.91	181.9	7.95
S21	Mixing	Black – bad odor	5.92	182.1	8.29
S22	Mixing	Black – bad odor	5.92	181.6	8.03
AS22	Fresh	Black – bad odor	7.25	30.9	8.09
S23	Salt	Black – bad odor	6.03	180.6	8.08
S24	Salt	Black – bad odor	6.02	180.3	8.04
S25	Salt	Black – bad odor	6.01	180.6	8.04
S26	Salt	Black – bad odor	6.01	182.9	8.21
S27	Salt	Black – bad odor	5.98	181.0	8.22
S28	Salt	Black – bad odor	6.01	180.8	8.10
S29	Salt	Black – bad odor	6.03	181.9	8.1
S30	Salt	Black – bad odor	6.03	180.7	8.23

Atomic Absorption Varian 800 (Varian, Australia). Quality control was done for Cd, Fe, Zn, Mn, Cu, Ni, Pb and Cr by using (Merck ICP4) standard solutions. The errors were within 95% confidence level.

2.2.2. Sequential extraction procedure

The sequential extraction procedure of (Tessier et al., 1979) was used because it was widely employed in studying the chemical fractionation of soils, dusts and marine sediments (Tessier et al., 1979; Navas and Lindhofer, 2003; Sulkowski and Hirner, 2006 and Momani, 2006).

The quality control procedure including reagent blanks, duplicate samples, and analysis of standard reference material was used to assess precision and accuracy of the obtained data. Blanks were prepared in a similar manner and were analyzed before each measurement. All extractions and analyses were made with duplicate samples for quality control assessment, and the average results were reported. The analytical accuracy for the total heavy metal content was confirmed by analyzing the standard reference material (SRM, soil 7) from the National Institute of Standards and Technology (NIST), USA. The level was better than $\pm 6\%$. The detection limits for heavy metals by using the flame AAS technique (FAAS) of (Varian, 800) are as follows in ($\mu\text{g/l}$): Co

(0.05), Cr (0.06), Cu (0.04), Fe (0.1), Mn (0.02), Ni (0.01), Pb (0.1), and %RSD was less than 1.3.

3. Results and Discussion

3.1. Black mud physicochemical properties

The saltwater mud samples are generally black in color; with few exceptions of reddish black color Table (3). The freshwater mud samples (AS3, AS14, AS15 and AS22) are white in color. The depth ranges from 3-10 cm from mud surface. All freshwater and saltwater mud samples has bad odor, due to higher organic matter content.

The pH value of seawater ranged from 5.91 to 6.28 with an average of 5.99. While the freshwater has higher pH values ranged from 6.84 to 7.25 with an average of 7.05. The pH values of both saltwater ranges: 7.74 to 8.51 with an average of 8.05, and the freshwater mud sample ranges 8.11 to 8.31 with an average of 8.11. Therefore, they possess almost similar average pH; which was above 8; which indicates the alkaline nature of this type of water. The interesting feature was the conversion between seawater pH value (5.99) and saltwater mud pH value (8.05) from mild acidic to alkaline. Therefore, the mild acidic media of the seawater would cause the heavy metals to remain in solution rather than to precipitate into the black mud.

Table 2. Sequential extraction procedure.

Fraction	Procedure
Exchangeable	1 g of sample is extracted with 8 ml of pH = 7, unbuffered 1.0 M MgCl ₂ in Polyethylene centrifuge tubes for 1 hour at 25°C with continuous agitation
Carbonate	Residue from exchangeable fraction extracted with 8 ml of pH 5, 1.0 M NaOAc for 5 hours at 25°C with continuous agitation.
Fe-Mn oxides	Residue from Carbonate fraction, extracted with 20 ml of 0.04 M NH ₂ OH.HCl in 25% acetic acid (v/v) for 5 hours at 96 °C with occasional agitation.
Organic	The residue from Fe-Mn oxides fraction extracted with 3 ml of 0.02 M HNO ₃ and 5 ml of 30% H ₂ O ₂ adjusted to pH 2 with concentrated HNO ₃ . The mixture was heated to 85 °C for 2 hours with occasional agitation. A second 3 ml aliquot 30% of H ₂ O ₂ (pH 2 with concentrated HNO ₃) was then added and the sample was heated again to 85°C for 3 hours with occasional agitation. After cooling, 5 ml of 3.2 M NH ₄ OAc in 20% (v/v) HNO ₃ was added and the sample diluted to 20 ml and agitation continuously for 30 minutes.
Residual	The residue from the organic fraction was digested with 15 ml conc. HNO ₃ , heated to 95°C for 3 hours sonicated for 1 hour at 60 °C, filtered and diluted with 1 % (v/v) HNO ₃ in a 25 ml Polyethylene volumetric flask to the mark and then stored at 4°C until the time of analysis.

The electrical conductivity (EC) of seawater ranges (163.4-188.5 mS/cm) with an average value of 181.27 mS/cm. whereas freshwater samples characterized by low EC values vary from 10.19 to 38.90 mS/cm with an average of 26.62 mS/cm. High EC value of Dead Sea mud compared to freshwater mud can be due to its enrichment with salts and other alkaline minerals such as calcite, aragonite, and gypsum which are often precipitated from saltwater (Abdel-Fattah, 1997).

3.2. Heavy metal abundances

The concentrations of the heavy metals and the Loss On Ignition (LOI) were illustrated in Table (3). Generally, the Dead Sea black mud does not show anomalous or even high heavy metal levels. This might be attributed to the lack of metallic-rich occurrences in the catchment areas of the Dead Sea (Abed, 1985). Furthermore, in the Dead Sea area there are no main sources of pollution compared with other urban areas.

The heavy metals content in the black mud of the Dead Sea was compared with freshwater and saline water sediments such as hemipelagic sediments (Deep Sea sediment), near shore sediments, and freshwater sediments (Lake and River mud), Table (4) and Figures (2a, b, c and d). These figures indicate clearly that most of the heavy metals (Fe, Mn, Cr, Cu, Co and Ni) are depleted in the Dead Sea black mud when compared with hemipelagic mud, lake mud, river mud and the near shore sediments, representing both freshwater and saline water sediments. The only exceptions were Pb and Zn to lesser extent, which were enriched in the Dead Sea black. The findings of this study are in agreement with that reached by (Oumeish, 1996). Moreover, the heavy metals contents of the studied black mud agree with (NRA, 1991). The average of LOI which was obtained by NRA laboratories (37.16 wt%) was higher than what reported in this study (32.69 wt%). This might be attributed to the differences in analytical methods used in LOI measurements, where in this study the LOI was measured at 550°C, following the procedure of (Jaradat et al., 2005). Whereas, the NRA data are measured at 1000°C, which means more structural halogens were evaporated and thus increases the LOI values.

The Dead Sea water is highly enriched with various heavy elements. However, the relative depletion of heavy metals in the Dead Sea black mud, compared with other sediments worldwide, might be attributed as most of these heavy elements are incorporated into salt complexes rather than being precipitated or co-precipitated with neither sediments nor organic matter, Figures (2a, b, c and d). Furthermore, the average saltwater pH value was 5.99, indicating a mild acidic media, which would enhance the heavy metals solubility rather than precipitation. This can explain the enrichment of the heavy metals in the seawater

while it is depleted in the black mud. Similar findings were reported by several researchers (Oumeish, 1996; Nissebaum, 1969 and 1974).

3.3. Speciation of heavy metals in the black mud

The sequential extraction results in grouping the heavy metals, based on their preferred phases as following: carbonate phase [Ni and Co], Fe-Mn Oxides [Mn], residual phase [Cr, Cu, Fe and Pb]. There were no preferences of any metal to the exchangeable and organic phases. The correlation coefficients of heavy metals and LOI are in agreement with the sequential extraction results, Table (6). The correlation coefficient results showed that none of the heavy metals have positive correlation with Loss On Ignition (LOI) and Mn. This might be interpreted that none of them preferred the organic phase. Particularly, Mn had no significant correlation with any other metals confirming the fact that Mn is associated with iron-manganese oxides phase only. The manganese was found on the Dead Sea shores as black incrustations in form of Mn-Oxides such as psilomelane, cryptomelane and pyrolusite (Garber et al., 1981). This would explain the reason why Mn was confined particularly to this phase.

Moreover, Cr, Cu and Fe had significant correlations with each other, Ni and Co that had moderate correlation values while a positive correlation among Cu, Cr and Zn was observed. Nevertheless, the combination between sequential analysis and correlation coefficient was highly in agreement with each other, where these groups of heavy metals are concentrated in the residual fraction. These results were found in agreement to high extent to those findings of heavy metals in the Dead Sea sediments (Nissenbaum, 1974).

Table 3. Table showing the average heavy metal concentrations (mg/kg) and LOI (wt%) in the saltwater mud samples.

Sample	Fe	Cu	Ni	Zn	Cr	Mn	Co	Pb	LOI
S1	1230.8	9.2	31.4	16.3	25.6	195.8	10.0	59.5	27.6
S2	1348.0	10.8	33.3	19.9	31.4	324.9	11.0	62.0	34.2
S3	1610.3	12.9	43.8	29.3	39.7	380.9	12.0	68.0	36.7
S4	1579.3	13.3	36.2	25.5	34.3	365.8	10.0	56.3	36.3
S5	1318.5	11.0	35.7	26.4	33.5	288.6	9.0	58.3	28.4
S6	1232.8	12.4	41.4	43.1	36.1	348.7	11.0	72.0	32.9
S7	1386.0	12.0	48.3	45.6	42.8	140.2	7.0	55.3	31.1
S8	855.8	12.5	66.4	52.7	35.0	206.4	10.0	61.0	33.4
S9	926.8	10.7	60.5	38.9	36.5	216.9	7.0	58.5	34.0
S10	1725.3	5.1	45.9	9.5	41.0	393.6	6.0	42.5	30.5
S11	1086.0	11.1	64.3	29.1	38.5	227.6	11.0	49.5	35.8
S12	1270.0	13.1	63.9	26.9	42.4	320.3	12.0	64.7	32.2
S13	1100.0	13.0	62.9	37.2	42.3	234.8	11.0	70.8	33.2
S14	1240.5	12.7	64.2	31.8	39.6	293.8	15.0	52.8	31.0
S15	1999.0	13.1	59.1	30.7	35.4	189.9	14.0	65.8	22.2
S16	1344.5	10.9	56.9	29.9	37.5	255.7	13.0	61.3	36.0
S17	1331.0	12.4	61.4	46.5	44.7	167.2	13.0	57.5	33.5
S18	746.5	8.6	51.7	17.5	32.7	109.5	11.0	58.5	31.3
S19	365.3	5.5	41.8	9.0	23.9	176.1	9.0	29.5	31.0
S20	1584.8	15.2	68.7	46.2	50.2	150.2	13.0	47.0	33.7
S21	1873.3	15.2	71.7	66.7	59.5	114.2	13.0	60.0	31.8
S22	1736.3	14.7	66.8	38.2	56.4	143	12.0	53.8	32.8
S23	1589.3	16.2	69.0	96.8	48.7	131.0	14.0	58.3	34.7
S24	1624.3	15.7	68.1	69.7	50.4	136.7	12.0	49.3	35.2
S25	1610.8	16.7	72.1	67.3	51.2	145.2	13.0	46.3	32.5
S26	924.0	12.4	61.9	32.2	43.2	99.2	9.0	51.0	34.8
S27	1530.8	12.2	62.7	42.1	53.8	162.4	9.0	53.8	32.3
S28	1503.3	16.0	68.7	46.0	47.6	118.3	10.0	73.8	33.2
S29	1167.8	13.1	62.4	38.7	45.2	121.2	9.0	62.5	33.1
S30	2137.5	18.9	73.2	70.3	65.6	285.3	13.0	60.8	32.9
Mean	1365.9	12.6	57.2	39.3	42.2	214.8	11.0	57.3	32.6
Max.	2137.5	18.9	73.4	96.8	65.6	393.6	15.0	73.8	36.7
Min.	365.3	5.1	31.4	9.0	23.9	99.2	6.0	29.5	22.2
σ	324.5	3.0	19.6	9.7	12.8	78.8	3.79	9.3	2.9

Table 4. Comparison of heavy metal contents in several types of mud and sediments from freshwater and saline water, all are in ppm except Fe in wt%

Elements	Dead Sea This Study*	Hemipelagic Mud ¹	Lake Mud ²	River Mud ¹	Near Shore Sediments ³
**Fe	0.195	4.75	3.64	3.4	-
Mn	254	760	378	620	850
Cu	13	30	29	32	48
Co	12	20	57	14	13
Cr	43	97	68	85	100
Ni	58	53	40	32	55
Zn	39	24	73	23	95
Pb	58	130	27	78	20

*The data is for saltwater mud samples only.

**Fe as Fe₂O₃ (% by mass); ¹ Govindaraju, (1989); ² Dasa, et al., (2006); ³ Wedepohl, (1960)

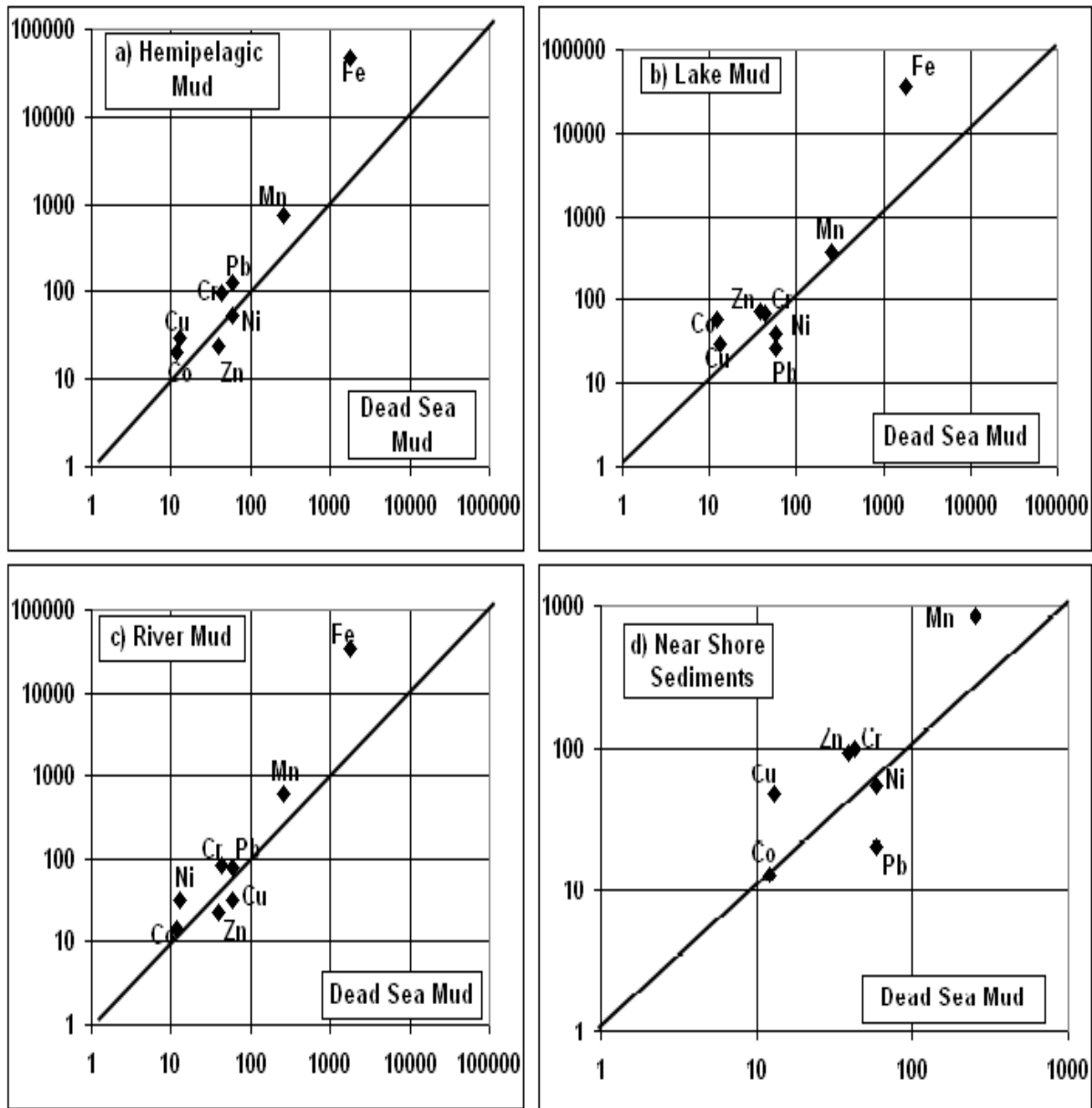


Fig. (2): 1:1 ratio scatter plot shows the comparison of heavy metals between the Dead Sea Mud and (a) Hemipelagic mud and (b) Lake mud (c) River mud and (d) Near Shore sediments.

Table 5. Distribution of heavy metals based on sequential extraction in various chemical fractions of black mud.

Sites	Fraction	Cr	Mn	Cu	Ni	Co	Fe	Pb
S1	Exchangeable	4.0	5.8	0.8	5.3	2.0	0.3	1.3
	Carbonate	6.0	33.5	3.5	12.0	4.0	5.7	7.8
	Fe-Mn Oxides	5.5	109.8	1.3	5.3	1.9	156.2	7.0
	Organic	2.0	33.5	3.5	5.5	1.5	478.9	8.8
	Residual	7.0	13.8	4.0	5.0	1.8	607.1	18.3
S6	Exchangeable	4.0	7.3	0.8	4.3	1.5	1.2	0.8
	Carbonate	7.5	42.5	3.8	12.8	4.1	1.4	5.5
	Fe-Mn Oxides	9.0	216.3	1.8	7.8	2.8	65.0	7.5
	Organic	3.0	36.5	2.8	6.8	1.3	322.6	7.0
	Residual	11.0	33.5	4.5	6.3	1.8	631.2	20.0
S15	Exchangeable	4.5	6.3	0.8	5.3	1.5	0.3	2.5
	Carbonate	8.5	33.3	3.8	14.8	4.3	4.6	5.8
	Fe-Mn Oxides	9.0	108.3	1.0	5.3	2.2	133	7.3
	Organic	4.0	22.0	2.0	3.3	0.8	228.9	9.3
	Residual	10.5	12.8	4.0	6.0	1.7	581.1	25.8
S22	Exchangeable	5.0	15.8	0.8	6.3	1.6	1.3	4.3
	Carbonate	8.5	52.0	3.8	18.3	4.2	18.9	6.8
	Fe-Mn Oxides	10.0	45.3	2.0	6.8	1.9	568.6	9.0
	Organic	9.0	14.0	1.8	5.8	0.5	426	8.0
	Residual	19.0	26.5	7.3	10.8	2.1	758	22.3
S28	Exchangeable	5.0	14.8	0.8	7.3	1.6	0.4	4.0
	Carbonate	7.5	15.5	3.8	17.8	4.1	2.3	9.8
	Fe-Mn Oxides	10.5	49.5	1.3	8.0	2.2	127.1	7.8
	Organic	5.5	35.5	3.8	7.0	1.2	535.6	11.8
	Residual	12.0	13.0	3.8	6.5	1.4	744.5	25.3

Table .6. Correlation coefficient matrix; significance threshold at 99% confidence level is (0.4357) (n=34)

	Fe	Cu	Cr	Zn	Ni	Pb	Co	Mn	LOI
Fe	1.00								
Cu	0.52	1							
Cr	0.56	0.76	1						
Zn	0.42	0.74	0.69	1					
Ni	0.27	0.66	0.75	0.67	1				
Pb	0.17	0.37	0.07	0.1	0.002	1			
Co	0.23	0.64	0.42	0.37	0.42	0.23	1		
Mn	0.00	0.17	0.04	-0.16	-0.18	0.23	0.35	1	
LOI	0.17	-0.04	-0.10	0.09	0.07	-0.13	-0.37	-0.49	1

3.4. Effect of mixing with freshwater

The samples were divided into two groups, based on Table (1): (a) Normal samples which are totally covered by Dead Sea saltwater alone (thirty samples), (b) Mixed samples, those affected by the mixing of freshwater and Dead Sea saltwater, and they were seven samples namely (S1, S2, S3, S14, S15, S21 and S22), those samples are

located in front of the big tributaries at Swimah, Zarqa-Ma'en and Al-Mujeb. The comparison of the heavy metal concentrations with LOI values for the mud samples in the mixed water and Dead Sea saltwater showed no significant difference across them, thus no effect of the mixing processes was dominant, Fig. (3).

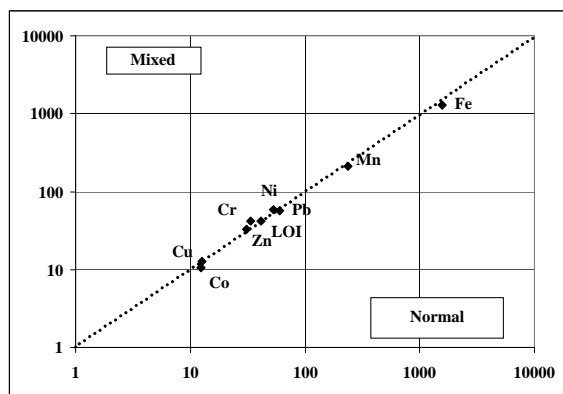


Fig. (3): 1:1 ratio scatter plot to compare the average heavy metals and LOI between the mixed water and normal seawater samples.

4. Conclusion

The heavy metal levels in the Dead Sea black mud samples were depleted comparatively to other saline and freshwater sediments worldwide. This might be attributed to the fact that there are no geological exposures of metallic rich deposits in the catchments area of the Dead Sea. The mud samples are not exposed to anthropogenic pollution sources such as aerial deposition. Although Dead Seawater is rich in heavy metals, the black mud is depleted in the most of trace elements. Thus, it was found that heavy metals prefer to be incorporated in the soluble salt complexes rather than precipitating due to the mild acidic environment of the Dead Sea water.

The findings of the sequential extraction and the analysis of correlation of various chemical parameters showed that none of heavy metals preferred the organic phase of the black mud. Finally, there was no effect of mixing the freshwater entering the Dead Sea from surrounding streams with saltwater on the components of the Black mud.

References

- [1] Abdel-Fattah, A. N. (1997). Mineralogical, geochemical, healing Characterization and origin of the Dead Sea Clay Deposits, M. Sc. Thesis, University of Jordan. P 140.
- [2] Abdel-Fattah, A., and Schultz-Makuch, D. (2004): Dead Sea black mud: Medical geochemistry of a traditional therapeutic agent. American Geophysical Union (AGU), Abstract book.
- [3] Abdel-Fattah, A. and Pingitore, N. Jr. (2009): Low levels of toxic elements in Dead Sea black mud and mud-derived cosmetic products. *Environmental Geochemistry and Health*, 31(4): 487-492. Abdel-Samie, S. G. ES-Shahat, M .F. and Al-Nawayseh, K. M. (2004). Mineralization Sources of Surface and Subsurface Water at the Southeastern Edges of Dead Sea Basin in Jordan. *Isotope and Radioactive Research*. 36: 167-186.
- [4] Abed, A. (1985). Geology of the Dead Sea, Dar Al Argam, Amman, Jordan. PP 232.
- [5] Abul-Kashem, M. and Singh, B. (1999). Heavy metal Contamination of Soil and Vegetation in the Vicinity of industrial in Bangladesh. *Water Air Soil Pollution*. 115: 347-361.
- [6] Al-Naddaf, M. (1992). Geochemical and Mineralogical Characteristic and Classification of Soil in Kitim-Nueima Area. M. SC. Thesis. Yarmouk University Department of Geology, Jordan.
- [7] Al-Nawayseh, K. (2003). Evaluation of Surface and Groundwater Sources in Southern Ghore-Jordan, Ph.D. Thesis, Ain Shams University.
- [8] Arab Potash Company.(2007).Site measurements(end of April)
- [9] Dasa, B.K., AL-Mikhlaifib, A.S., and Kaura, P. (2006) Geochemistry of Mansar Lake sediments, Jammu, India: Implication for source-area weathering, provenance, and tectonic setting. *Journal of Asian Earth Sciences*. 26: 649–668.
- [10] Es-Shahat, M.F, Al-Nawayseh, K. M, Jiries, A. G, Al-Nasir, F.M. (2003). Pesticides and Heavy Metal Distribution in Southern Dead Sea Basin. *Bull, Environ. Contamination. Toxicology*. 71: 1230-1238.
- [11] Garber, R.A., Nishra, A., Nissebaum, A., and Friedman, G.M. (1981): Modern deposition of Manganese along the Dead Sea shore. *Sedimentary Geology*. 30: 267-274.
- [12] Govindaraju, K. (1989): Complilation of working values and sample description on 272 geostandards. *Geostandards Newsletter. Special Issue*. 13:1-113.
- [13] Jaradat, Q., Masadeh, A., Zaitoun, M.A. and Maitah, B.M. (2005). Heavy Metal Contamination of Soil, Plant and Air of Scrap yard of Discarded Vehicles at Zarqa City, Jordan. *Soil and Sediment Contamination*, 14: 449-462.
- [14] Momani, K. (2006). Partitioning Of lead in Urban Street Dust Based on the Particle Size Distribution and Chemical Environments. *Soil and Sediment Contamination*. 15: 131-146.
- [15] Navas, A., and Lindhorfer, H., (2003): Geochemical speciation of heavy metals in semiarid soils of the central Ebro Valley (Spain). *Environmental International*. 29:661-680.
- [16] Neev, A and Emery, K. O. (1967): The Dead Sea Depositional Processes and Environments of Evaporates. *Geological Survey of Israel Bulletin*. 41:1-6.
- [17] Nissebaum, A., (1969): Studies in the geochemistry of the Jordan River-Dead Sea system, Unpublished Ph.D. Thesis (In English), UCLA.
- [18] Nissenbaum, A. (1974). Trace Elements in Dead Sea Sediments. *Israel Journal of Earth Science*. 23: 111-116.
- [19] NRA Laboratories Report (1991): Amman, Jordan. 50-54.
- [20] Oumeish, Y. (1996). Climatotherapy at the Dead Sea in Jordan. *Clinics in Derinntaology*. 14: 659- 664.
- [21] Powell, J.H. (1988): The geology of Karak area, Map sheet No. 3152 II. Nat. Res. Auth. Unpublished Report. NRA, Amman. 172 pp.
- [22] Preer, J. R. Sekhon, H. S and Stephens, B. R. (1980): Factors Affecting Heavy Metals Contents of Garden Vegetables. *Environmental Pollution*. 1: 95-104.
- [23] Tessier, A. Campbell, C and Bisson, M. (1979): Sequential Extraction Procedure For The speciation of Particular Trace Metal. *Analytical. Chemistry*. 51: 844-885.
- [24] Sulkowski, M., and Hirner, A., (2006): Element fractionation by sequential extraction in a soil with high carbonate content. *Applied Geochemistry*. 21:15-28.
- [25] Wedepohl, K.H. (1960): Composition and development of the exterior of the earth. *Astrophysical Journal*. 131(3): 638-663.

Exchange Coupling and Magnetic Properties of Fe/Ir(001) superlattices

B. Alqassem, B.A. Hamad^{*}, J.M. Khalifeh

Department of Physics, University of Jordan, Amman 11942, Jordan

Abstract

We present ab initio calculations of the exchange coupling for Fe/Ir system using a self-consistent full-potential linearized augmented plane-wave (FLAPW) method. The local spin density approximation (LSDA) as well as the generalized gradient approximation (GGA) are used to treat the exchange correlation potential. In this work, supercells consisting of two layers of Fe separated by Ir layers ranging from 1 to 7 are constructed. For each spacer layer thickness, two calculations were performed, one for ferro- and another for anti-ferromagnetic ordering of Fe atoms. We obtained an oscillatory behavior for the interlayer exchange coupling with a period of 7.83 Å for both LSDA as well as GGA.

© 2009 Jordan Journal of Earth and Environmental Sciences. All rights reserved

Keywords: Magnetism, Superlattice, Fe, Ir, Exchange Coupling, ab initio calculations.

1. Introduction

All through the last two decades, the influence of interlayer exchange coupling (IEC) between magnetic layers separated by a non-magnetic spacer has involved substantial efforts. Ever since, it was firstly studied by Grünberg [1] for Fe/Cr superlattices in 1986, and following the discovery of Parkin [2] on coupling oscillates between the FM and the AF configurations as a function of spacer layer thickness, and the interest is on the rise. Shortly afterwards, Parkin has shown that oscillatory exchange coupling occurs with almost all transition and noble metals as spacer materials [3]. Not until the last decade when the reward of this detection is translated to a definite application. The giant magneto-resistance became a renowned industrial application for the coupling. The giant magneto-resistances are utilized as responsive detectors for magnetic field in magnetic data storage; it is now commonly used in magnetic read head of all magnetic recording devices. It is all due to the remarkable properties of these materials, exhibited in the great change of their resistance once placed in a small field, large enough to reverse their magnetic alignments. This discovery gave an important momentum for intensive investigations in this area of research [4-11].

An assortment of methodologies covering a wide spectrum of theoretical approaches has been explored to clarify this inspiring phenomenon, approaches like the first principles or tight-binding total energy calculations [12-15], the Ruderman-Kittel- Kasuya-Yosida (RKKY) theory [16-19], a free-electron model [20-22] and the Anderson s-d Mixing models [23, 24]. Recently, a new disclosure stating that every one of the above models can be integrated into a more broad approach. Seeing the interlayer

-exchange coupling as an interpretation of quantum size effect and described in terms of

(spin-dependent) reflection coefficients of electrons at the interfaces between the nonmagnetic spacer and the ferromagnetic layers [25-27].

In this work, we study the interlayer exchange coupling in Fe/Ir(001) superlattices using a self-consistent full-potential linearized augmented plane-wave (FLAPW) method. Although, this system is expected to be a good candidate for interlayer exchange coupling, yet the theoretical studies to investigate its behavior are scarce. Previous experimental studies have obtained high quality of Fe/Ir(001) superlattice with flat interfaces and absence of interdiffusion [28-30], the fact that makes them promising structures for GMR devices.

The rest of the paper is arranged as follows: In section, II we present the computational details of calculations; in section III, we put forward the results and discussion; and finally, in section IV we provide recommendations and conclusions.

^{*} Corresponding author. b.hamad@ju.edu.jo

2. Computational Details

All calculations are performed using the self-consistent full-potential linearized augmented plane-wave (FLAPW) method within the density functional theory [31]. The calculations are carried out using the LSDA [32] as well as GGA [33] approximations. The cutoff energy of the plane waves in the interstitial region between the muffin tins is taken as 16 Ry for the wavefunction and 169 Ry for the potential. The k-point sampling is performed using Monkhorst–Pack grid in the irreducible part of the Brillouin zone. The wavefunction expansion inside the muffin tins are taken up to $l_{max} = 10$ and the potential expansion up to $l_{max} = 4$. These parameters were chosen to set the self-consistent calculations where the convergence is taken with respect to the total charge of the system with a tolerance of 0.0001 electron charges. The muffin-tin radii are taken to be 1.12 Å and 1.24 Å for Fe and Ir, respectively. The calculations are performed using Fermi-level smearing of 0.005 Rydberg.

The calculated lattice constant of bulk ground states of bcc Fe and fcc Ir are found to be 2.84 Å and 3.87 Å. We used the supercell technique to build FeIr_n ($n=1-7$) superlattices, Fig.1 presents one of these supercells, namely FeIr₄ superlattice. To optimize the structures, the lattice constants for each cell were relaxed in three steps. We start with a cubic supercell and varying the volume of the supercell keeping the c/a ratio constant. The energy dependence on the volume is tested and the equilibrium volume is obtained using the Murnaghan's equation of state fit [34]. Then varying the c/a ratio at the equilibrium volume obtained from the first step. The energy dependence on the c/a ratio is tested to obtain the equilibrium value. Finally, the volume of the supercell re-varied again at the equilibrium c/a ratio obtained from the second step. The new equilibrium volume is found by the Murnaghan's equation of state fit [34].

The lattice constants for each superlattice structure are given in Table 1. It is to be noted here that the lattice parameters are compared with those obtained by Vegard's law [35], where the lattice constants are calculated using the following equations:

$$a = \frac{a_{Fe} + na_{Ir}/\sqrt{2}}{n+1} \quad (1)$$

$$c = \sqrt{2}a \left(\frac{n+1}{2} \right) \quad (2)$$

here the $\sqrt{2}$ factor is used to convert from fcc-structure to bct-structure, while the $(n+1)/2$ factor represents the number of unit cells formed. A close look at Table 1 reveals that the lattice constants of the supercells obtained by the optimization technique are close to those of Vegard's law.

The total energy is calculated for ferro- and antiferromagnetic configurations of Fe for each FeIr_n superlattice. The same structure has been used for both configurations for the sake of consistency to obtain reliable energy differences, i.e. the unit cell is doubled even in the ferromagnetic configuration for comparison purposes. The exchange coupling, j , is calculated using the equation:

$$j(d) = E_{tot}^{\uparrow\downarrow}(d) - E_{tot}^{\uparrow\uparrow}(d) \quad (3)$$

where d is the thickness of the spacer layer and $E_{tot}^{\uparrow\downarrow}(d)$ and $E_{tot}^{\uparrow\uparrow}(d)$ are the total energies of the system in AF and FM arrangements. The exchange

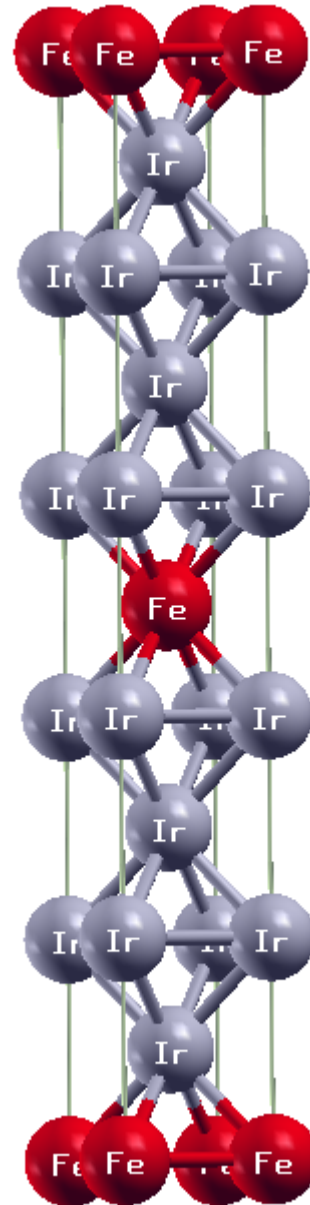


Fig.1 : The schematic diagram for FeIr₄ supercell.

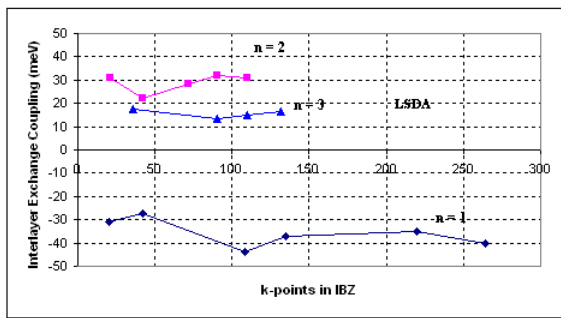
coupling convergence with respect to the number of k-points in the irreducible Brillouin zone (IBZ) has been checked for each FeIr_n structure. The convergence test of j as a function of the number of k points is shown in Fig. 2 for both the LSDA and GGA exchange potentials. It is found that j converges faster than the total energy as a function of the number of k-points.

3. Results and Discussion

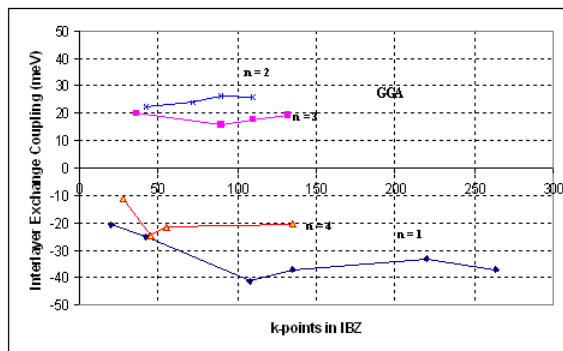
3.1. Exchange Coupling

The study of the interlayer exchange coupling requires the calculation of the total energy of Ferro- and antiferromagnetic ordering of Fe designed for each Ir spacer layer thickness. The IEC is calculated for both LSDA and GGA exchange correlation potentials as shown in Fig. 3. As the Ir spacer thickness is increased, the IEC Table1: The lattice constants for the relaxed seven superlattices.

Superlattice	Lattice Constants by Optimization Technique		Lattice Constants by Vegard's Law	
	a (Å)	c (Å)	a (Å)	c (Å)
FeIr	2.67	3.64	2.79	3.94
FeIr ₂	2.71	5.60	2.77	5.88
FeIr ₃	2.71	7.62	2.76	7.81
FeIr ₄	2.72	9.56	2.76	9.75
FeIr ₅	2.73	11.45	2.75	11.68
FeIr ₆	2.73	13.42	2.75	13.62
FeIr ₇	2.73	15.40	2.75	15.55



(a)



(b)

Fig. 2 : Interlayer exchange coupling, j (meV) for FeIr_n multilayers as a function of the number of k - points in the IBZ for different number of Ir layers for (a) LSDA and (b) GGA.

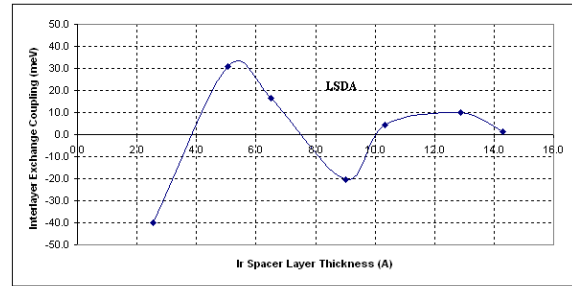
oscillate between FM and AF by a period of oscillation about 7.83 Å for both the LSDA and GGA potentials, which is comparable with that obtained by Stoeffler [36]. It is to be noted here that only one period of oscillation could be obtained in our calculations since we are restricted with small Ir thickness up to 14 Å.

From Fig.3, it can be noticed that the LSDA calculations give higher values of the interlayer exchange coupling than those obtained using the GGA exchange-

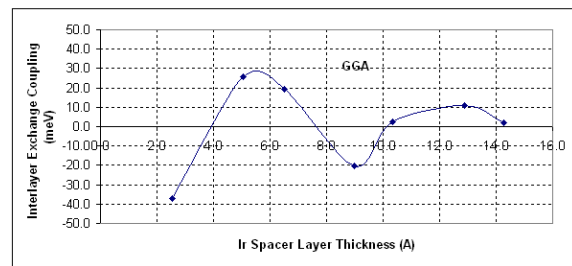
correlation potential, with the same period of oscillation for both approximations.

3.2. Magnetic structure

Magnetic moments (in Bohr magnetons, μ_B) for the case of FM ordering, using the GGA and LSDA calculations for different layers, are presented in Table 2 and Table 3, respectively. As expected, the Fe layer carries the overwhelming part of the total magnetic moment. The table also points out the following: (i) the



(a)



(b)

Fig. 3: Interlayer exchange coupling, (meV) for FeIr_n multilayers as a function of Ir spacer layer thickness (Å) for (a) LSDA and (b) GGA potentials.

Table 2: Magnetic moments (in Bohr magnetons) for each layer in the Fe/Ir unit cell using the GGA approximation. Results are shown for one Fe layer on top of up to 7 Ir layers.

Fe	Ir layer number						
	1	2	3	4	5	6	7
2.14536	0.03033						
2.52453	-0.07337	-0.07338					
2.68122	0.08753	-0.10992	0.08690				
2.69386	0.09129	-0.04400	-0.04406	0.09129			
2.68806	0.04772	-0.06590	0.00860	-0.06586	0.04770		
2.70738	0.05870	-0.07538	0.00964	0.00966	-0.07516	0.05875	
2.72556	0.07470	-0.05586	0.00494	0.02015	0.00497	-0.05588	0.07471

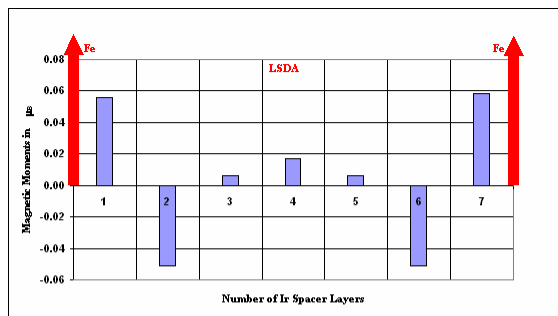
first Ir substrate layer continuously ferromagnetically coupled to the Fe layer. (ii) The second Ir layer continually antiferromagnetically coupled to the Fe layer.

In Fig. 4, the induced magnetic moments per atom on the Ir spacer layers are plotted, using both the GGA as well

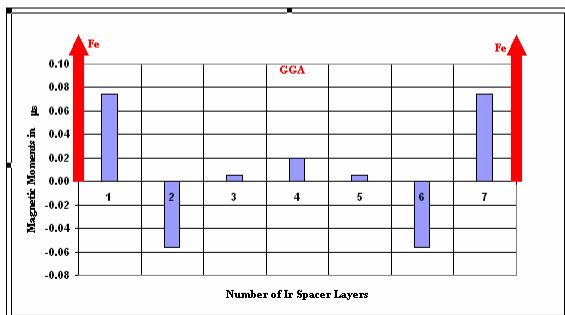
as the LSDA potentials, for the FeIr₇ multilayers system. The induced magnetic moments of Ir atoms are oscillating; however, the magnetic moments in the central layers are weaker than those at the interface. The induced magnetic moment at the interface is 0.075 μ_B whilst 0.020 μ_B at the central layer for the GGA calculations. The induced magnetic moments are reduced in the LSDA calculations. The induced magnetic moment at the interface is 0.056 μ_B whilst 0.017 μ_B at the middle layer.

Table 3: Magnetic moments (in Bohr magnetons) for each layer in the Fe/Ir unit cell using the LSDA approximation. Results are shown for one Fe layer on top of up to 7 Ir layers.

Ir layer number	
Fe	1 2 3 4 5 6 7
1.93343	0.02476
2.32311	-0.06518 -0.06518
2.51308	0.07706 -0.09588 0.07706
2.51253	0.06905 -0.03793 -0.03794 0.06906
2.51602	0.03807 -0.05674 0.00828 -0.05674 0.03807
2.54075	0.04495 -0.06511 0.01152 0.01152 -0.06511 0.04495
2.55823	0.05584 -0.05095 0.00593 0.01701 0.00593 -0.05104 0.05584



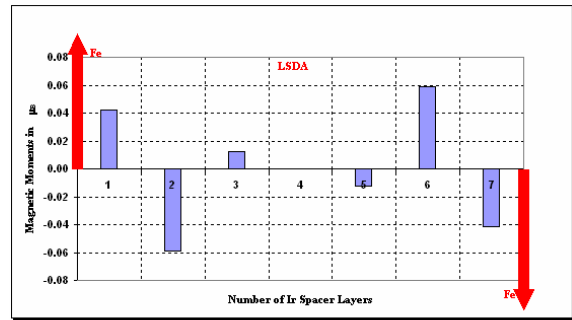
(a)



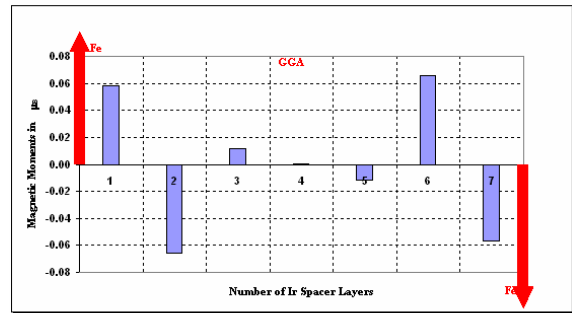
(b)

Fig. 4: Induced magnetic moments on Ir spacer layer in ferromagnetic FeIr₇ multilayer using (a) LSDA and (b) GGA calculations. The Fe atoms are placed in positions 0 and 8.

The oscillatory behavior also appears for the magnetic moments on Ir atoms, with zero magnetic moment at the central Ir atom, Fig.5.



(a)



(b)

Fig. 5: Induced magnetic moments on Ir spacer layer in anti-ferromagnetic FeIr₇ multilayer using (a) LSDA and (b) GGA calculations. The Fe atoms are placed in positions 0 and 8.

4. Conclusion

The IEC for Fe/Ir is calculated by using the self-consistent FLAPW method with the LSDA and GGA exchange correlation potentials. We can summarize the main points of this study as follows:

1. The IEC has an oscillatory behavior as a function of Ir spacer layer thickness with a period of 7.83 Å for both the LSDA as well as the GGA potentials. The period of oscillation is found to be the same for both the LSDA as well as GGA potentials.
2. The induced magnetic moments on Ir atoms show an oscillatory behavior. The first Ir substrate layer is always ferromagnetically coupled to the magnetic layer, whereas, the interior Ir layers are coupled antiferromagnetically.
3. The GGA gives higher magnetic moments for Fe and Ir as compared to the LSDA.

References

- [1] P. Grünberg, R. Schreiber, Y. Pang, M. B. Brodsky, and H. Sowers, Phys. Rev. Lett., 57, 2442 (1986).
- [2] S. S. P. Parkin, N. More, and K. P. Roche. Phys. Rev. Lett. 64, 2304(1990).
- [3] S. S. P. Parkin Phys. Rev. Lett. 67, 3598 (1991).
- [4] Dinia, M. Stoeffel, K. Rahmouni, and D. Stoeffler, Europhys.Lett. 42, 331 (1998).
- [5] H. Yanagihara, Eija Kita, and M. B. Salamon, Phys. Rev. B 60,12957 (1999).

- [6] Y. Lou, M. Moske, and K. Samwer, *Europhys. Lett.* 42, 565 (1998).
- [7] S. Colis, A. Dinia, C. Ulhaq-Bouillet, P. Panissod, C. Meny, G. Schmerber, and J. Arabski, *Phys. Stat. Sol. (a)* 199, 161 (2003).
- [8] S. Mirbt, O. Eriksson, B. Johansson, and H. L. Skriver, *Phys. Rev. B* 52, 15070 (1995).
- [9] S. Mirbt, A. M. N. Niklasson, B. Johansson, and H. L. Skriver, *Phys. Rev. B* 54, 6382 (1996).
- [10] J. Unguris, R. J. Celotta, and D. T. Pierce, *Phys. Rev. Lett.* 79, 2734 (1997).
- [11] N. N. Shukla and R. Prasad, *Phys. Rev. B* 70, 14420 (2004).
- [12] F. Herman, J. Sticht, and M. V. Schilfgaard, *J. Appl. Phys.* 69, 4783 (1991).
- [13] P. Lang, L. Nordström, R. Zeller, and P. H. Dederichs, *Phys. Rev. Lett.* 71, 1927 (1993).
- [14] J. Kudrnovský, V. Drchal, L. Turek, and P. Weinberger, *Phys. Rev. B* 50, 16105 (1994).
- [15] D. Stoeffler and F. Gautier, *Phys. Rev. B* 44, 10389 (1991).
- [16] Y. Yafet, *Phys. Rev. B* 36, 3948 (1987).
- [17] [17] C. Chappert and J. P. Renard, *Europhys. Lett.* 15, 553 (1991).
- [18] W. Baltensperger and J. S. Helman, *Appl. Phys. Lett.* 57, 2954 (1990).
- [19] R. Coehoorn, *Phys. Rev. B* 44, 9331 (1991).
- [20] J. Barnas, *J. Magn. Magn. Mater.* 111, L215 (1992).
- [21] R. P. Erickson, K. B. Hathaway, and J. R. Cullen, *Phys. Rev. B* 47, 2626 (1993).
- [22] J. C. Slonczewski, *J. Magn. Magn. Mater.* 126, 374 (1993).
- [23] Y. Wang, P. M. Levy and J. L. Fry, *Phys. Rev. Lett.* 65, 2732(1990).
- [24] P. Bruno, *J. Magn. Magn. Mater.* 116, L13 (1992).
- [25] M. D. Stiles, *Phys. Rev. B* 48 7238 (1993).
- [26] P. Bruno, *J. Magn. Magn. Mater.* 121, 248 (1993).
- [27] P. Bruno, *Phys. Rev. B.* 52, 418 (1995).
- [28] S. Andrieu, M. Piecuch, L. Hennem, J. Hubsch and E. Snoeck, *Europhys. Lett.* 26, 189 (1994).
- [29] S. Andrieu, E. Snøeck, P. Arcade and M. Piecuch, *J. Appl. Phys.* 77, 1308(1995).
- [30] S. Andrieu, Hubsch, E. Snoeck, H. Fischer and M. Piecuch, *J. Magn. Magn. Mater.* 148, 6 (1995).
- [31] P. Blaha, K. Schwarz, and J. Luitz, *Wien2k Package* (www.wien2k.at), A Full Potential Linearized Augmented Plane Wave Package for Calculating Crystal Properties (Kalheinz Schwarz, Techn. Universitat Wien, Austria).
- [32] U. Von Barth, and L. Hedin. *J. Phys. C* 5, 1629 (1972).
- [33] J. P. Perdew, S. Burke, and M. Ernzerhof. *Phys. Rev. Lett.* 77, 3865 (1996).
- [34] F. D. Murnaghan, *Proc. Natl. Acad. Sci. (U.S.A.)* 30 244 (1944).
- [35] L. Vegard, *Z. Phys.* 5, 17 (1921).
- [36] D. Stoeffler, *Eur. Phys. J. B* 37, 311 (2004).

Associated Minerals and their Influence on the Optical Properties of Jordanian Kaolin

Akl M. Awwad*, Rafat Ahmad, Hatem Alsyouri

Industrial Chemistry Centre, Royal Scientific Society, Amman, Jordan

Abstract

Kaolin samples from Al-Disi kaolin deposits in southeastern region of Jordan are associated with mineral impurities, which impart color to this kaolin and adversely affect its application in paper and paint industries. The associated mineral impurities with kaolin were separated by deflocculating of kaolin particles in polymeric sodium polyphosphate solution. The crude kaolin, deflocculated kaolin (suspended kaolin), and the associated mineral impurities with kaolin (residue) were determined by X-ray fluorescence, X-ray diffraction, FTIR spectroscopy, and spectroscopic studies. The composition of the residue separated from Al-Disi kaolin composed mainly from quartz, feldspar, and hematite. The separation of these associated mineral impurities from al-Disi kaolin by deflocculating process improves the brightness of kaolin to be suitable for processing to produce kaolin that meets specifications for paper making, filler, cosmetics and other uses that demand high whiteness and low impurity content.

© 2009 Jordan Journal of Earth and Environmental Sciences. All rights reserved

Keywords: Kaolin; Sodium polyphosphate; Jordan; Associated minerals; Deflocculated agent; FTIR, XRD, Optical properties.

1. Introduction

Kaolin is a geologic term referring to a rock that is predominately composed of > 50% [1] of the mineral kaolinite $[Al_2Si_2O_5(OH)_4]$. Kaolin is a layered silicate mineral, with one tetrahedral sheet linked through oxygen atoms to one octahedral sheet of alumina octahedral. The mineral kaolin is usually associated with various impurities: quartz, anatase, rutile, pyrite, siderite, feldspar, etc., depending on the origin and depositional environment [2]. These impurities affect the characteristic properties of kaolin and its utility for applications. The industrial applications of kaolin in ceramics tiles and glass, paper coating, rubber, adhesives, sealants, as filler [3] lead to an extensive research to be carried out on the nature of the existing impurities associated with kaolin [5-7]. In Jordan, although kaolin deposits occur, their industrial usage has been restricted to the manufacturing of ceramics. No research has been conducted to understand the genesis and suitable industrial applications of kaolin occurrences in the country.

Suspensions of kaolin particles in aqueous solutions are tremendously important in ceramics, pharmaceuticals, paints, and cosmetics industries. The performance of kaolin suspensions depends on the stability of these suspensions. The stability of the kaolin suspensions is governed by two factors van der Waals forces and repulsive electrostatic forces. kaolin suspensions are prepared by suspending the kaolin particles in aqueous

solutions of different deflocculated agents such as sodium sulfite, sodium nitrate, sodium phosphate, monomeric and oligomeric phosphates [5,9-11].

The purpose of the present paper is to separate and identify the associated mineral impurities with kaolin by deflocculating of kaolin particles in sodium polyphosphate solutions and to be useful for industrial applications.

2. Materials and Methods

Kaolin clay samples have been collected from the quarry of Al-Disi district of Aqaba state located 45 km east of Al-Quweira town. The location of this site is shown in Fig.1. The mine area is around 54 Mt as given in the survey of Natural Resources authority, Jordan.

Clay samples in this study were crushed ground, using a vibrating Disc mill (model RS 200, Retsch-Germany). The clay was then sieved through a 325-mesh sieve (44 μ m particle size) and washed with dionized water three times to dissolve soluble salts.

Concentration of associated minerals was performed by the following method: 100 grams of the fine powder of Al-Disi clay, 1-2 grams of sodium polyphosphate, and 200-400 ml of water were mixed in a glass tank and slurried by stirring with an electric stirrer for 30 minutes to form suspension of clay. The clay deflocculated particles were removed by decantation and repeated washing with water to get the associated mineral impurities concentrate as residue. The residue was dried in an oven at 105 °C.

* Corresponding author. aklm@rss.gov.jo

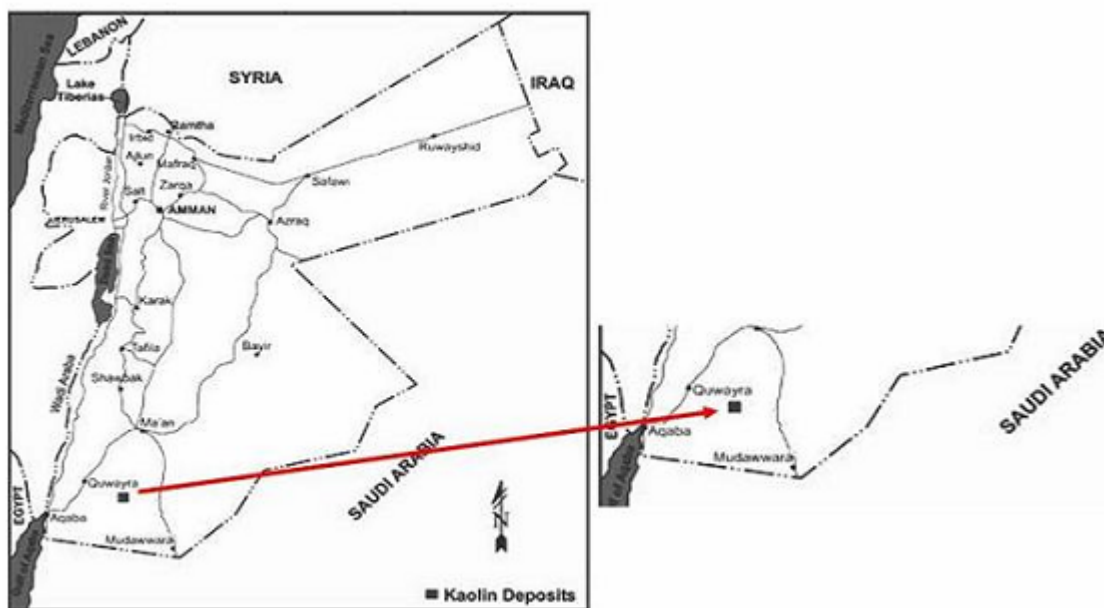


Figure1. Location map of the kaolin mines in Jordan. ■, Al-Disi deposits of kaolin

The chemical composition of the samples was determined by X-ray fluorescence (XRF-800 Shimadzu).

The XRD patterns were taken using X-ray diffractometer (Shimadzu XRD-6000) equipped with Cu $K\alpha$ radiation source using Ni as filter and at a setting of 30 kV/30 mA. All XRD data were collected under the same experimental conditions, in the angular range $3^\circ \leq 2\theta \leq 50^\circ$.

FTIR spectra were obtained by IRprestige-21 Shimaduz FT-IR- spectrophotometer, using KBr pellet method.

Optical brightness and color values were measured by Color Touch Macbeth color-eye 7000 spectrophotometer. Brightness represents the percent of reflectance of light at a wavelength of 457 nm. The "Lab" system based on the color opposites gives representation of the colors. The term "L" is a measure of lightness/darkness and varies from 100 for perfect white to 0 for absolute black. The red/green color is indicated by "a". The more positive value a indicates reddishness and negative value indicates greenishness. Similarly, the yellow/blue shades are represented by "b", positive value for yellow and negative for bluishness.

3. Results and Discussion

Table 1 shows the chemical composition of the crude clay, the suspended clay and the concentrated associated minerals (residue) determined by X-ray fluorescence (XRF).

Table 1. Chemical composition of crude kaolin, suspended kaolin, and associated minerals in weight percent (nd = not determined).

	Crude kaolin	Suspended kaolin	Associated minerals
SiO ₂	59.18	63.48	90.51
Al ₂ O ₃	26.22	22.89	5.16
Fe ₂ O ₃	1.52	1.36	3.05
TiO ₂	1.42	1.33	nd
CaO	0.11	0.18	0.11
MgO	0.09	0.17	nd
Na ₂ O	0.11	0.09	0.08
K ₂ O	1.12	1.42	1.44
P ₂ O ₅	0.11	0.18	nd
LOI	10.21	8.88	

It is observed that the concentrations of SiO₂ are greater than the theoretical value, which can be explained by the presence of various amounts of quartz in all samples as indicated by X-ray diffraction. After Si, the most abundant impurity elements are Fe, Ti, and K. Crude clay and suspended clay contain around 1.5% iron oxide and titanium oxide. It can be seen that the associated mineral impurities with clay predominantly composed of > 90% SiO₂, > 5% Al₂O₃, and > 3% Fe₂O₃.

The amounts of associated mineral impurities with clay in all samples studied are 4% to 6% of the total crude clay. Also it can be seen in Table 1 that the ignition loss is less significant as compared to the theoretical value, which confirms the low carbonate in the clay samples. The K₂O percentage is more important. This gives an indication of the existence of illite and K-feldspar in this clay.

X-ray diffraction study (XRD) of the crude kaolin samples Fig. 2a showed that the kaolinite is the dominant mineral phase with quartz impurities. The suspended kaolin samples deflocculated by sodium polyphosphate Fig.2b show the emergence of a small peak at 2θ = 8.9 relative to illite, which does not appear in the crude clay samples. The associated mineral impurities are separated as residue by deflocculating process of crude kaolin as can be seen in Fig. 2C shows that quartz is the dominant mineral impurities with additional reflection of feldspar and hematite.

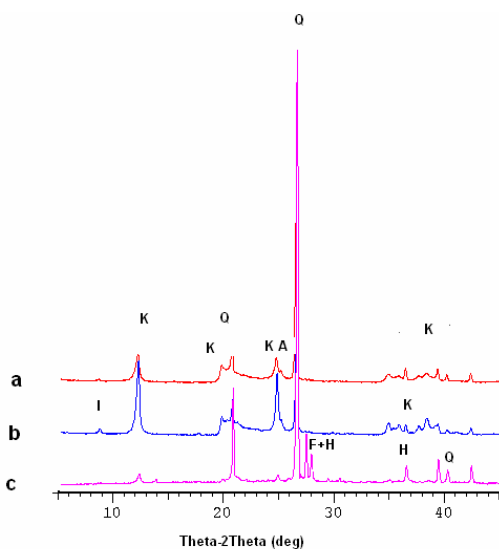


Figure 2. X-ray diffraction patterns of < 50-μm size (a) crude kaolin; (b) suspended kaolin; (c) associated mineral (residue). K: Kaolinite, Q: Quartz, A: Anatase, I: Illite, F: Feldspar, H: Hematite.

FTIR spectra of the crude kaolin, suspended kaolin, and the residue (associated mineral impurities) are illustrated in Fig. 3. The FTIR profiles of both crude kaolin and the suspended kaolin are roughly similar, as seen in Figures 3a and 3b. The FTIR spectrum shows the strongest absorbance bands at 3698, 3655, 3624, 1040, 799, cm⁻¹, characteristic of kaolinite, Table 2.

A shoulder at ≈ 1099 cm⁻¹ indicates the presence of quartz. A weak band at around 1449 cm⁻¹ indicates the presence of carbonate bearing minerals. FTIR spectra of the residue Fig. 3c shows a strong band of H₂O at 3445 cm⁻¹ dominates the OH-stretching region. The absorption bands in the 450 -1103 cm⁻¹ owing to Si-O, Si-O-Si, Al-O-Si deformation and Si-O stretching are characteristic of quartz and feldspar.

Table 2. FTIR band assignments of crude kaolin, suspended kaolin, and associated minerals.

Assignments	Crude/suspended kaolin Band (cm ⁻¹)	Associated Minerals Band (cm ⁻¹)
OH - vibration	3697, 3655, 3624	
OH stretching of water	3444	3444
OH deformation of water	1639	1647
CO ₃ vibration	1449	1432
Si-O-Si	1098	1100
- Si-O-	1039	
AlAlOH	918	
Si-O-Si	795	800
Si-O stretching of quartz	758	
Al-O-Si	696	640
Si-O	649	
Si-O-Si deformation	538	
Si-O-Si deformation	471	475
Si-O deformation	430	

The microscopic studies showed that the associated minerals (residue) separated from Al-Disi kaolin clay by deflocculated kaolin in sodium polyphosphate consist mainly of Quartz, feldspar, and hematite, Fig.4.

The associated mineral impurities (residue) are treated with concentrated hydrochloric acid; a pale yellow solution is formed. The pale yellow solution was separated from the unreacted residue by filtration and analyzed by Inductively-coupled Plasma optical Emission Spectroscopy (ICP-OES). The results showed that the solution consists mainly of iron oxides. This result indicates the presence of small amounts of hematite in the residue. The microscopic photograph, Fig. 5 shows the remaining residue contains quartz and feldspar.

The data for the two optical properties whiteness and color values are reported in Table 3.

The whiteness of the suspended kaolin is compared to the crude kaolin sample of 49%. The term L is a measure of lightness/darkness and varies from 100 for perfect white to 0 for absolute black. The red/green balance is indicated by "a" (the more positive the value "a", the greater the redness and the more negative the more greenness). The yellow/blue shades are presented by "b". The positive value gives yellowness and the negative corresponds to blueness). The whiteness and color values such as Lab values in Table 3 show the whiteness of suspended kaolin (deflocculated by polymeric sodium polyphosphate); and are superior to that crude kaolin. Both kaolin samples have positive values for "a" and "b" indicating that they are red and yellow. The suspended kaolin sample have lower values of "a" and "b" than that of crude kaolin. This indicates that the redness and yellowness of suspended kaolin is decreased due to the decrease of metal oxides impurities such as iron oxides. It seems that these oxides decrease the whiteness of kaolin.

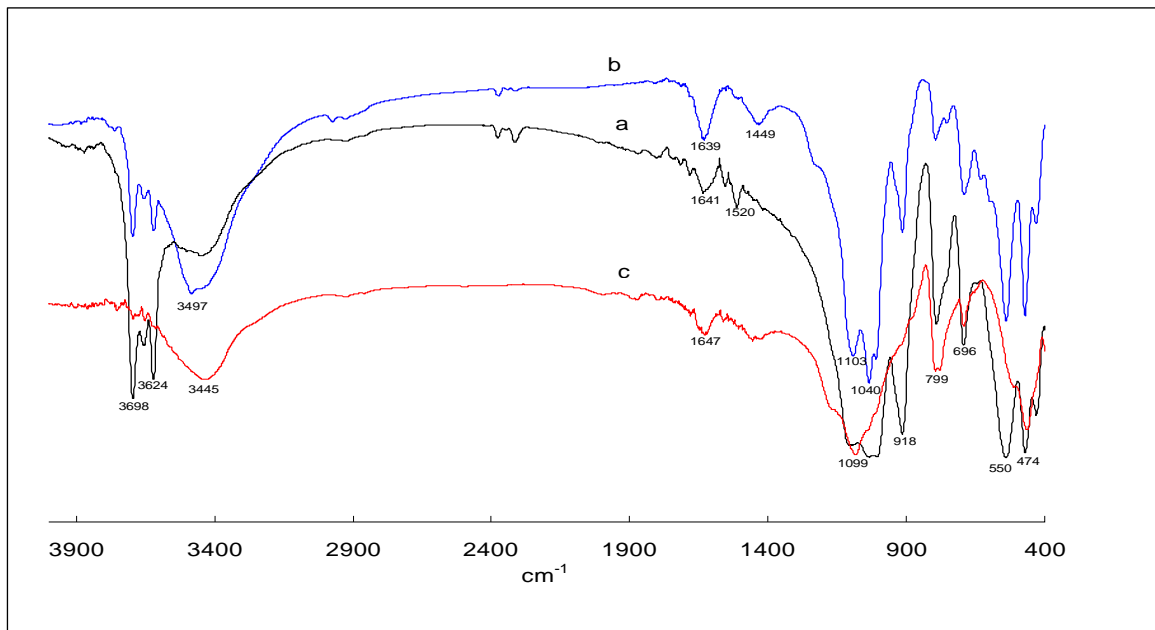


Figure 3. FTIR spectra: (a) crude kaolin; (b) suspended kaolin; (c) associated minerals (residue).

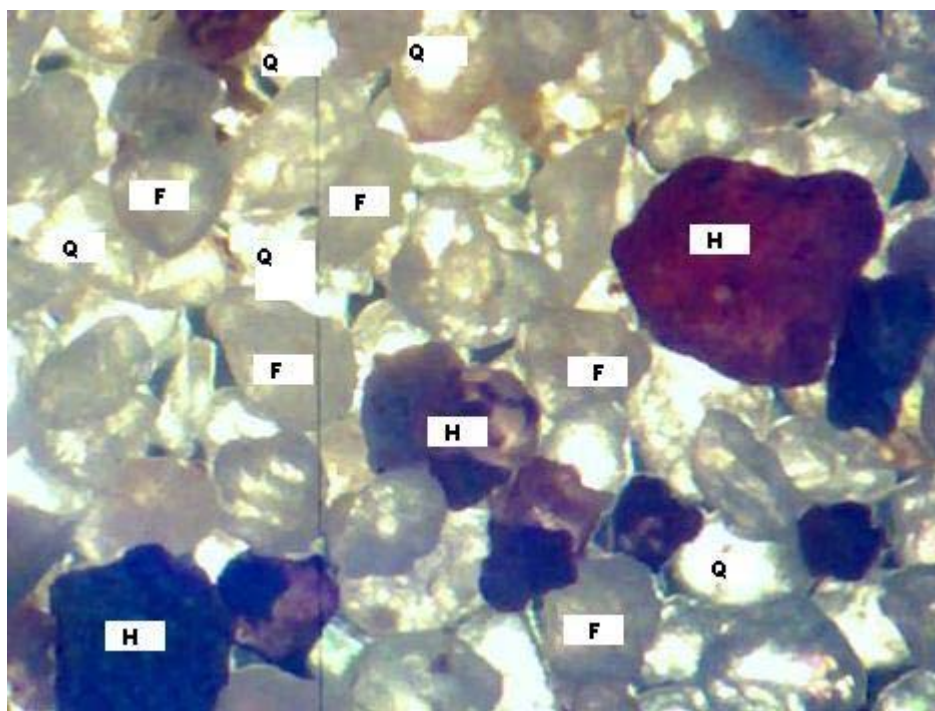


Figure 4. Microscope pictures of associated mineral impurities taken by Wraymer BM-3400 T microscope with magnification x 200. H: hematite; F: feldspar; Q: quartz.

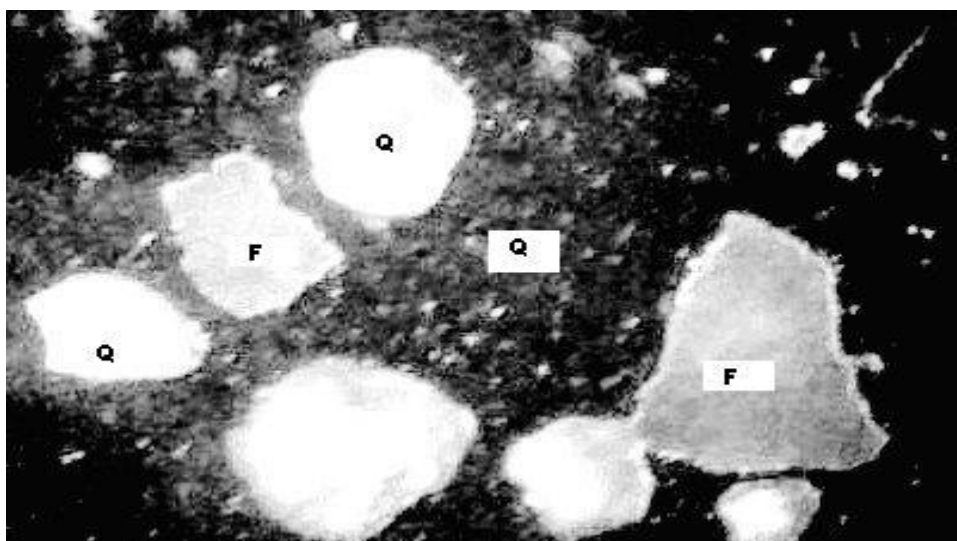


Figure 5. Microscope pictures of associated mineral impurities taken by Wraymer BM-3400 T microscope with magnification x 200. After treatment with hydrochloric acid. F: feldspar; Q: quartz.

Table 3. Optical properties: whiteness and Lab values of crude kaolin and suspended kaolin.

		Crude kaolin	Suspended kaolin
whiteness		49.17	65.27
color values	L	79.64	88.29
	a	2.29	0.69
	b	7.62	7.39

a: Reddishness value, b: Yellowness value, L: Lightness/darkness

4. Conclusion

The chemical analysis, XRF, and XRD show that Al-Disi kaolin clay is mainly constituted of silica and alumina in major quantities and iron, titanium, calcium, magnesium and other elements in minor quantities. The loss of ignition value indicates that clay has lower carbonaceous matter. The X-Ray diffraction study shows the presence of quartz, feldspar, hematite, and illite as major phases. The presence of the above minerals was further confirmed by microscopic studies. The deflocculating of kaolin clay with polymeric sodium polyphosphate (SPP-kaolinite clay) raised its whiteness from 49.17 to 65.27. The FTIR spectra analysis reveals that the polymeric sodium polyphosphate was basically held onto kaolinite clay.

Acknowledgments

The authors are thankful to the Royal Scientific Society for financial grant and for permission to communicate this work, and to Natural Resources Authority Jordan for providing kaolin samples.

References

- [1] T. Dombrowsky, The origins of kaolinite-implication for utilization. In: Carty, W. (Ed.), Science of Whiteware. The American Ceramic Society, Westerville, OH, 2000, pp. 3-12.
- [2] R.W. Grimshaw, Physics and Chemistry of Clay, 4th ed. Ernest Benn, London, ISBN: 1971, 0510-47701-7.
- [3] H.H. Murray, Ullmann's Encyclopedia of Industrial Chemistry, 5th Edition. VCH Publishers, 1986, pp. 109-136.
- [4] W. B. Jepson, Structural iron in kaolinites and in associated ancillary minerals. In: Stucki, J. W.; Goodman, B. A.; Schwertmann, U. (Eds.), Iron in Soils and Clay Minerals. NATO Advanced Science Institutes Series. D. Riedel Publishing Company, Dordrecht, Holland, 1988, pp. 467-536.
- [5] N. Yildiz, M. Erol, B. Baran, Y. Sarikaya, A. Calimil, Modification of rheology and permeability of Turkish ceramic clays using sodium silicate. Applied Clay Science Vol. 13, 1988, 65-77.
- [6] S. Chandrasekhar, S. Ramaswamy, Influence of mineral impurities on the properties of kaolin and its thermally treated products. Applied Clay Science Vol. 21, 2002, 133-142.
- [7] S. Chandraschar, S. Ramaswamy, Investigation on a gray kaolin from south east India. Applied Clay Science Vol. 37, 2007, 32-46.

- [8] T. Manfredini, G.C. Pellacani, P. Pozzi, A.B. Corradi, Monomeric and oligomeric phosphate as deflocculants of concentrated aqueous clay suspensions. *Applied Clay Science* Vol. 5, 1990, 193-201.
- [9] D. Penner, G. Lagaly, Influence of anions on the rheological properties of clay mineral dispersion. *Applied Clay Science* Vol. 19, 2001, 131-142.
- [10] F. Andreola, E. Castellini, J.M.F. Ferreira, S. Olhero, M. Romagnoli, Effect sodium hexametaphosphate and ageing on the rheological behaviour of kaolin dispersions. *Applied Clay Science* Vol. 31, 2006, 56-64.
- [11] D. Derrington, M. Hart, T.M. White worth, Low head sodium phosphate and nitrate hyperfiltration through thin kaolinite and smectite layers- Application of engineered systems. *Applied Clay Science* Vol. 33, 2006, 52-58.

Mineralogy and Authigenesis of Zeolitic Tuff from Tall-Juhira and Tall Amir, South Jordan

Reyad A. Dwairi^{a,*}, Hani N. Khoury^b, Khalil M. Ibrahim^c

¹Tafila Technical University, Department of Natural Resources and Chemical Engineering, Tafila, Jordan

²The University of Jordan, Department of Applied Geology, Amman, Jordan

³Hashemite University, Department of Environmental Geology, Zarqa, Jordan

Abstract

Tall Amir and Tall Juhira are two important volcanoes located in southern Jordan. Huge quantities of zeolitic tuff deposits are existed within basaltic rocks. These two localities haven't been investigated nor evaluated for their mineralogical and zeolitic content. Zeolitic tuff from south Jordan is composed mainly of three components: Volcanic glass, primary rock forming minerals and secondary rock forming minerals.

Zeolitic tuff from Tall Juhira (ZTJ) are characterized by highly weathered red to brown color, and friable tuff. The main zeolitic tuff minerals in ZTJ are phillipsite and chabazite.

Zeolitic tuff from Tall Amir (ZTA) is characterized by gray color and well-cemented tuff. The main zeolitic tuff minerals are phillipsite, chabazite and analcime.

© 2009 Jordan Journal of Earth and Environmental Sciences. All rights reserved

Keywords: Zeolitic tuff; Tall-Juhira; Tall Amir; Phillipsite; Chabazite; Analcime.

1. Introduction

Zeolitic tuff associated with basaltic rocks in Jordan are exposed in different localities include northeast, central and south of Jordan, Figure (1) shows two important locations of basaltic volcano. The first one is Tall Juhira with latitude of (30° 38' 47") and longitude of (35° 49' 37") with a height of about (1355 m). It is one of the most important deposits of zeolitic tuff in the south of Jordan. The second one is Tall Amir with a latitude of (30° 33' 05") and longitude of (35° 47' 58") with a height of about (1049 m).

The study area is characterized by rainy period which is short in the studied volcanoes areas (December to March) with average annual precipitation of about 100 mm, the rest of the year is warm and dry. Occasional Snow falls mainly in the highlands, and may reach 70 cm in thickness. The maximum recorded temperature is 39 C° in July.

2. Regional Geology

Basalt in the studied areas is of Neogene age. It comprises porphyritic, fine grained rocks. The previous petrological, geochemical and geostatistical studies that dealt with the basalt from the study area demonstrates that they are sodic alkalic basalts that belong to the alkali olivine basalt series, and are considered as nepheline basanite (Ibrahim, 1987).

According to Ibrahim (1987) the essential minerals in the basaltic samples are pyroxene, plagioclase and olivine with variable amounts of opaques and nepheline. Apatite is the most abundant accessory mineral.

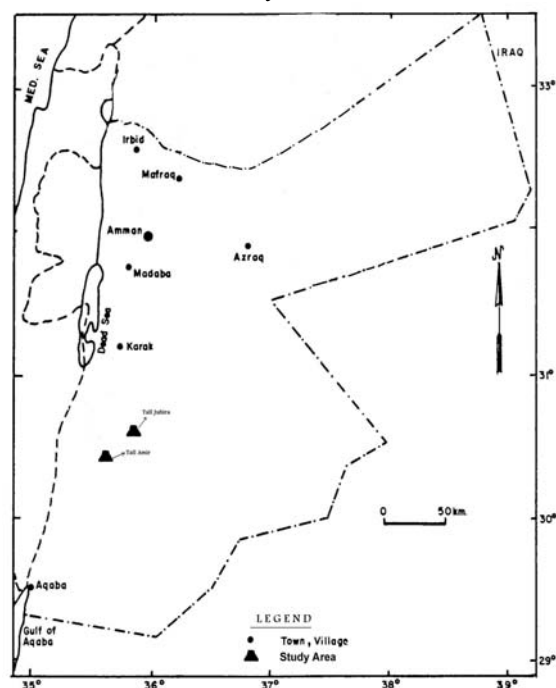


Fig. (1). Location map of the studied basaltic volcano.

* Corresponding author. rdwairi@ttu.edu.jo

Uneiza volcano is type localities for the basalt along the Dead Sea Rift in southern Jordan (1143m high). It comprises one of the symmetrical volcanic centers with basaltic flows separated by zones of pyroclastic deposits. The rocks of the volcano are 110 m thick of lapilli, ash, welded tuff, and basaltic flow. The lithics are angular to rounded and consist of carbonates, phosphates, shale, and chert. The studied cross section include two types of ejecta: the first one is at the bottom and belong to the Aritayn type which consists of reddish brown well bedded,

well sorted, well cemented, fining upward pyroclastic with small bombs, and Zeolites in this ejecta occur as cementing material. And the second type is the Hassan type, which consists of violet to black, poorly sorted, poorly cemented, angular to sub angular pyroclastics. The total thickness of the Aritayn type is 18 m in Jordan, while the Hassan type thickness is only 3 meters thick. Figure (2) is a columnar section of Jabal Uneiza volcano after (Ghrir, 1998).

Location	Thickness	Horizon	Lithology	Description	
Uneiza Volcano	20	Upper Zone Sideromelane Zone		Agglomerated, bad sorted bed cemented, dominated by basaltic to scoriaceous bombs and show variation in color form violet to black, with carbonate.	
				Normal grading ashes, well sorted, well cemented, laminated	
		Middle zone Palagonite		Normal grading lapilli, well sorted, well cemented with carbonate and silicious lithic, dominated by small rounded bombs at the lower part.	
				Ashes, well sorted well cemented with carbonate	
				Normal grading lapilli, well sorted, well cemented, brownish color, carbonate and shale lithic.	
	10	Lower Zone Zeolite Zone		Ashes, well sorted, well cemented, laminated, brownish color.	
				Normal grading lapilli, well sorted, well cemented, with few small bombs.	
				Medium to coarse lapilli, bad sorted, well cemented, brownish red color, dominated by bombs.	
		0			Fine to coarse lapilli, bad sorted, well cemented with carbonate lithic, dominated by small bombs, reddish brown color highly zeolite content.

Fig. (2) Columnar section of Jabal Uneiza volcano after (Ghrir, 1998).

3. Materials and Methods

Ten fresh representative channel samples were collected from the two volcanic centers and zeolitic tuff outcrop, five samples of each location.

Thin section petrography was carried out by using impregnation method. Ten thin sections of zeolitic tuff from the two locations were prepared and examined under the polarizing microscope.

The samples were investigated using scanning electron microscope (SEM) (Quanta 600 F, FEI) combined with Energy-dispersive X-ray analysis (EDX) mapping (Genesis 4000, EDAX) available in BGR, Hanover, Germany. EDX (spot analysis) was carried out during the progress of SEM studies. With SEM/EDX analyses technique, samples were investigated for their physical properties including size, shape, and surface morphology. EDX provides information on the chemistry of the individual particles.

X-ray Diffraction Analysis (XRD) for random preparation samples was done using Phillips X-ray Diffractometer. Random preparations for X-ray diffraction analyses were also made for zeolitic fractions of the size range between (1) mm and (0.3) mm.

4. Results

4.1. Transmitted polarizing microscope results

Thin sections investigation shows that the tuffaceous basaltic samples are composed of four major components:

1. Vesicles
2. Volcanic glass and Palagonite
3. Major rock forming primary minerals (olivine, nepheline, pyroxene, plagioclase)
4. Secondary weathering product minerals (zeolites, iron oxides, clay minerals, and calcite)

The volcanic tuff can be divided into two components (pyrogenic and authigenic minerals) according to the mineral formation phases. The term pyrogenic refers to the host mineral phase (major rock forming minerals), while the term authigenic refers to the alteration product (secondary product minerals).

The break down of rock-forming primary minerals during weathering transfers them into secondary minerals as alteration products. Willson (2004) has described the weathering of pyrogenic minerals and their alteration product. He found that olivine, plagioclase, and pyroxene break down during weathering to clay minerals, Fe oxides, and Ca, Na, K aluminosilicate rich minerals.

The studied thin sections show that most of the samples are highly-altered tuffaceous volcanic basalt. The weathering of volcanic rocks from all localities is indicated by number of presented phases. Thin sections investigation shows that the secondary weathered products are zeolites (phillipsite, chabazite, and analcime) and non zeolites such as smectite, calcite, and gypsum. The detailed results of thin section studies for both primary and secondary minerals are as follow:

4.1.1. Vesicles (V)

The results of studied samples indicate a typical vesicular texture of different degrees. These vesicles are mainly empty or filled with a secondary filling material. These vesicles are circular, subcircular and irregular in shape (Figure 3).

4.1.2. Volcanic Glass (Vg) and Palagonite (Pl)

Low-temperature alteration of basaltic glass produces palagonite. The word palagonite was used to describe the altered basaltic glass of the hyloclastics from palagonia in the Hyblean Mounts, Sicily (Honnorez, 1981). Palagonite is present in most of the studied thin sections with variable colors that range from dark brown, yellow brown to deep red, depending on the degree of alteration (palagonitization). Palagonite occurs as microphenocrysts in the groundmass of all thin sections. Lath shape euhedral tabular crystals with zeolitic coating are common (Figure 3). Under the binocular microscope, palagonite is characterized by its vitreous, wax like or resinous luster with a conchoidal fracture.

The studied thin sections show two types of volcanic glass. These are fresh volcanic glass and weathered volcanic glass (palagonite). Palagonite is not stable and tends to crystallize to zeolites and chlorite as alteration products. The alteration of palagonite (palagonitization) gives the general chemical composition of SiO_2 , Al_2O_3 , Fe_2O_3 , FeO , MgO , and H_2O (Kerr, 1977). The studied altered tuff shows all samples from Tall Juhira are characterized by the presence of palagonitic glass with different degrees of alteration while four samples from Tall Amir shows palagonitization .

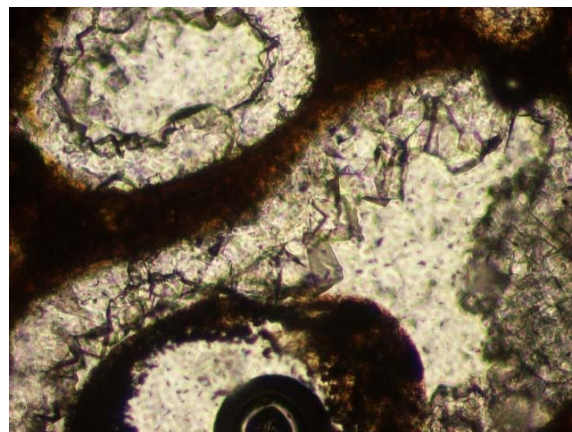


Fig. (3) vesicles from south Jordan zeolitic tuff (Tall Amir)

4.1.3. Major Rock Forming Primary Minerals

a- Olivine (Ol)

Olivine and its alteration product iddingsite (Id) are the most abundant microphenocrysts in most of the slides. Olivine is usually colorless and is highly fractured in the plain polarized light. The fresh crystals show olive green to pink interference colors. The crystals range in length from 0.3 to 2 mm. Olivine is altered to iddingsite (Id). Figure 4 shows a microphotograph from Tall Amir that is highly-altered olivine crystal to iddingsite. The iddingsitization is seen to surround the margins and the innermost parts of the crystal. Some crystals show corroded outlines and embayment.

Olivine usually is destroyed or replaced during the early stage of weathering. Olivine is altered by deuteric or hydrothermal process to a mixture of hydrous phyllosilicates and Fe-oxide minerals. In the latter case, the most common product is iddingsite, which may be optically homogeneous and crystallographically oriented with respect to the parent olivine (Wilson, 2004).

The transformation from olivine to iddingsite was studied in detail by Eggleton (1984), using transmission electron microscopy of ion-beam thinned specimens. A two-stage process was proposed. In the first stage, the olivine breaks down into thin lamellae consisting of a metastable hexagonal phase and elongated parallel to the olivine c axis. This transformation opens up solution channels which become infilled with lath-like crystals of saponite. In the second stage, water migrates more freely through the solution channels and permitting further growth of the smectite and goethite nuclei formed during early alteration and largely, but not entirely. In this instance, alteration was undoubtedly due to deuteric / hydrothermal activity, although weathering was considered to result in similar mineral assemblages. This point was amplified in a later study on the weathering of olivine in basalt to iddingsite by Smith et al, (1987). Three different basalts were examined. In each, the process of iddingsitization appears to have commenced before weathering, but progresses to completion as a result of later weathering. Iddingsite formation again involves etching along lamellar zones parallel to (001) and formation of smectite and oriented goethite within these zones. An important finding, however, is that some elements such as Al and Na, have been introduced from outside the weathering olivine crystal, showing that the process is not truly isochemical. In fact, in the later stages of decomposition, dioctahedral smectite and halloysite are associated with the weathered olivine. The initial stages of the alteration of olivine were explored in further detail by Banfield *et al*, (1990). It was founded that in altered basaltic andesites, the olivine consisted of fine intergrowths of forsterite-rich olivine and laihunite, an oxidized fayalitic phase where structural ferric iron is balanced by structural vacancies resulting in a distorted olivine structure. Where the intergrowths are widely spaced, the laihunite act as a barrier to weathering, resulting in the preferential dissolution and etching out of the forsterite to yield textures very similar to those reported by Eggleton (1984) and Smith *et al*, (1987). The etched out channels are first filled with semi-oriented aggregates of saponitic clay and subsequently with aggregates of oriented hematite crystals.

b- Plagioclase (Pla)

The second important rock forming mineral in the studied samples and the most abundant after olivine is plagioclase. In thin sections, plagioclase is found as phenocrysts or small laths in the groundmass. The crystals shape is euhedral to subhedral. The phenocrysts and lathes show albite twinning. In all thin section, plagioclase shows a highly strong alteration with partly or completely damaged crystals. Figure 5 shows lath shaped slightly altered plagioclase crystals which are dominated in most of the studied thin sections.

c- Pyroxene (Py)

High-Ca pyroxene diopside and augite are the most abundant clinopyroxenes in the studied thin sections. In thin sections clinopyroxene are colorless, pale green to bright green, and subhedral crystals. Figure 5 shows augite with plagioclase crystals as groundmass in most of the studied localities.

Orthopyroxenes are not abundant and are observed in restricted samples. Pyroxene have been found to weather to hydrous layer silicates in a similar way to that described for olivine (Willson, 2004).

d- Nepheline

The most abundant feldspathoidal mineral in all thin sections is nepheline. In thin sections, it appears colorless to turbid, euhedral to anhedral crystals. Nepheline crystals in most of slides are altered and not clear in the groundmass of basaltic tuff. The alteration product of nepheline is zeolites (Kerr, 1977).

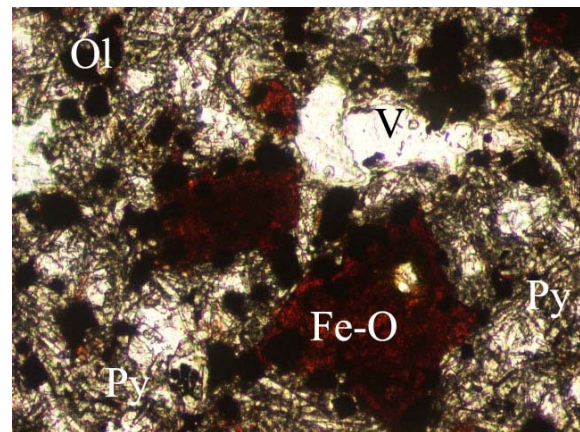


Fig. (4) Fe-oxides and iddingsite and augite with plagioclase crystals as groundmass from Tall Amir SJ.



Fig. (5) shows lath shaped slightly altered plagioclase crystals which are dominated in most of the studied thin sections.

4.1.4. Secondary Mineral Products (SM)

4.1.4.1 Zeolites

a-Phillipsite (Ph)

All samples from Tall Juhira south Jordan show phillipsitic crystals growth. It occur mainly as colorless, radial, fan shape crystal that is forming a thin rim of phillipsite crystals. Phillipsite is the most abundant zeolitic

mineral in all of the studied samples. It grows may be directly as the earliest phase in the walls of palagonite vesicles.

Figure 6 from Tall Juhira shows that phillipsite occurs as a rim of crystals growing directly on palagonite. Figure 7 from Tall Amir shows phillipsite growth as the first phase growth as a rim that shows a radial (fan like) shape growth of phillipsitic crystals with an assemblages of chabazite crystals while other plates show spherulitic growth of phillipsite crystals.

c- Chabazite (Ch)

Chabazite was reported for the first time in Jordan by Dwairi (1987) in Aritayn. Ibrahim (1993) described chabazite crystals from Jabal Aritayn as strongly zoned, elongated rhombohedra crystals with a complex penetration twinning. In all of the investigated sites, chabazite appears as colorless rhombohedra crystals with twinning and zoning.

Figure 7 shows that chabazite crystals grow as a second phase preceded phillipsite as indicated in samples from Tall Amir. Figure 8 shows a sugar like growth of chabazite crystals from Tall Juhira. All samples from this location show chabazite crystals.

4.1.4.2 Non Zeolitic Minerals

a - Clay minerals (Smectite (Sm))

Smectite form the earliest alteration product of the authigenic minerals. It appears as colorless, cloudy rim fringing palagonite granules and/or encrusting the vesicle walls with minute fringes (Figure 9) in most of the samples. This rim is circular in shape; and locks to form a flaky habit. It is absent in three samples from Tall Juhira, depending on the type and the degree of weathering. The most abundant smectite mineral in all samples is montmorillonite.

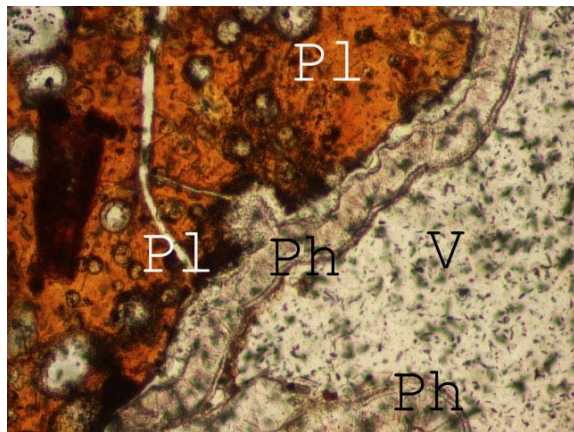


Fig. (6). Sample from Tall Juhira show that phillipsite occurs as a rim of crystals growing directly on palagonite followed by the growth of chabazite phase.

4.2 Scanning Electron Microscope and Energy-Dispersive X-ray Results.

Scanning electron microscopes (SEM) was carried out combined with energy-dispersive X-ray analysis (EDX) for all samples from Tall Juhira and Tall Amir. SEM/EDX analyses show that there are different zeolitic minerals included within the zeolitic tuff such as phillipsite, chabazite and analcime.

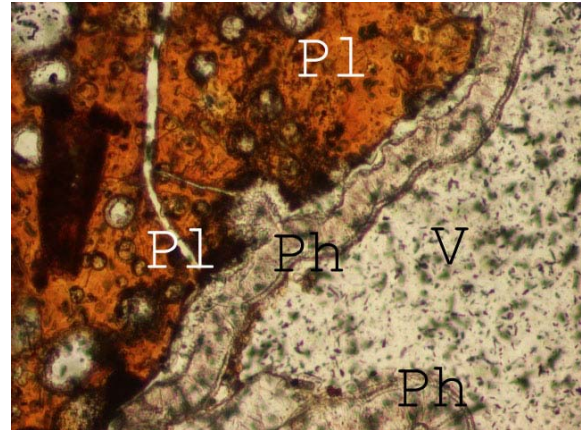


Fig. (6). Sample from Tall Juhira show that phillipsite occurs as a rim of crystals growing directly on palagonite followed by the growth of chabazite phase.

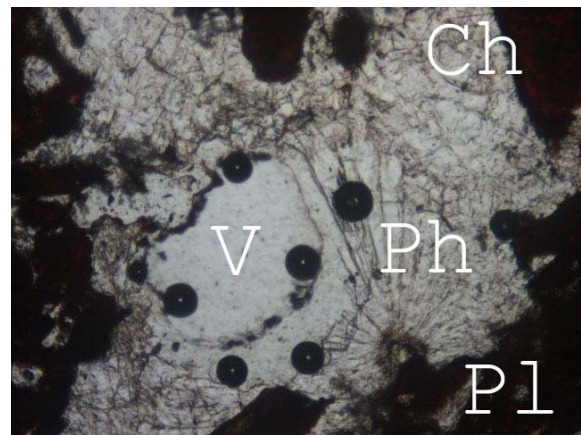


Fig. (7). Photograph shows a rim of phillipsite growth as a radial (fan like) shape growth of phillipsitic crystals from Tall Amir .

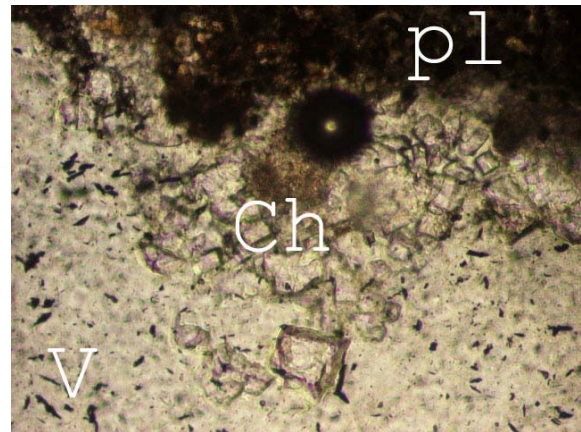


Fig. (8). Photograph show a sugar like growth of chabazite crystals as indicated in samples from Tall Juhira

a- Phillipsite

Phillipsite is the most abundant zeolitic mineral that appears under the SEM. It occurs as spherulitic radiating prismatic crystals. The spherulites are about 100µm to 150µm in diameter while the prismatic crystals commonly have zoning, and range in length from 100 µm to 200 µm and in width from 10µm to 5µm with a dome cap at the end of the prism

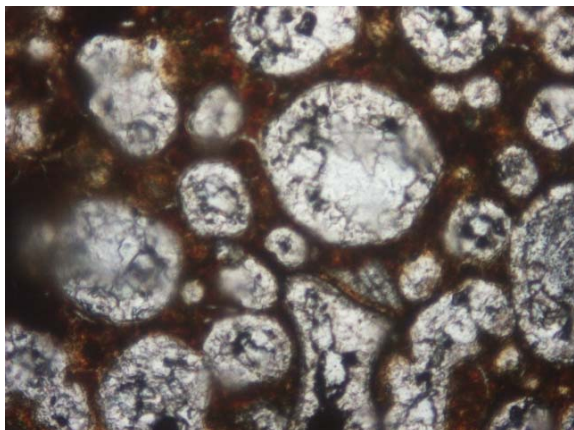


Fig. (9). Photograph shows a rim of clay minerals (smectite).

Figure 10 shows a group of growing prismatic phillipsitic crystals radiating from a growth center with a diameter range between 50 μm and 100 μm from Tall Juhira. Figure 11 shows two generations of phillipsite crystals from Tall Amir.

EDX results for phillipsite crystals are illustrated in Figures (12 and 13). Figure 12 from Tall Juhira shows that the chemical composition of phillipsitic crystals ($\text{K, Na, Ca}(\text{Si, Al})_8\text{O}_{16}$) has variable amounts of Na, K, and Ca. Figure 13 shows EDX results for phillipsite crystals from Tall Amir shows a high content of Na, K, and Ca. Phillipsite from Tall Juhira show high content of Ca and K and small amounts of Na as indicated in figure 12.

b- Chabazite

Dwairi (1987) described chabazite from Aritayn as wall rim crystals. Ibrahim (1993) has described also chabazite from Jabal Tarbush as rhombohedral crystals with dimensions range between 10-80 μm .

Chabazite is the second abundant zeolitic mineral after phillipsite in all studied localities. Chabazite crystals appear as a group of rhombohedral crystals with simple and complex penetration twinning. Crystals from the study areas range in dimensions from several microns to 15 μm . Chabazite from Tall Juhira, as in Figure 14, shows a complex penetration twinning with dimensions range between 15-20 μm . Both chabazite and phillipsite occur together as illustrated in Figure 14. Moreover, aggregates of chabazite crystals from Tall Amir grow directly on palagonite walls, as in figure 15.

EDX analysis for chabazite crystals for the two sites indicates a high content of Ca as illustrated in Figures (16 and 17). Chabazite from the two sites has a possible chemical composition similar to the theoretical chabazite of $\text{CaAl}_2\text{Si}_4\text{O}_{12}\cdot 6\text{H}_2\text{O}$.

d- Analcime

Analcime is the third zeolitic mineral found in the study area. It is restricted to Tall Amir locality. Analcime under the SEM appears as isolated euhedral crystals (rhombododecahedron form). Figure 18 shows isolated

euhedral crystals of analcime from Tall Amir. EDX data for analcime from Tall Amir showed high content of Na as indicated in figure 19. The theoretical chemical composition of analcime is $\text{NaAlSi}_2\text{O}_8\cdot\text{H}_2\text{O}$.

E- Smectite

It is one of the most important non zeolitic secondary minerals which are associated with phillipsite and chabazite. It is the main alteration product of the basaltic volcanic glass; and is developed in the early stage of alteration. Smectite under the SEM appears as circular to semi circular aggregates forming colloform structure. The circles have a radius of less than 30 μm . Figure 20 shows smectite circular growth with a cornflakes appearance.

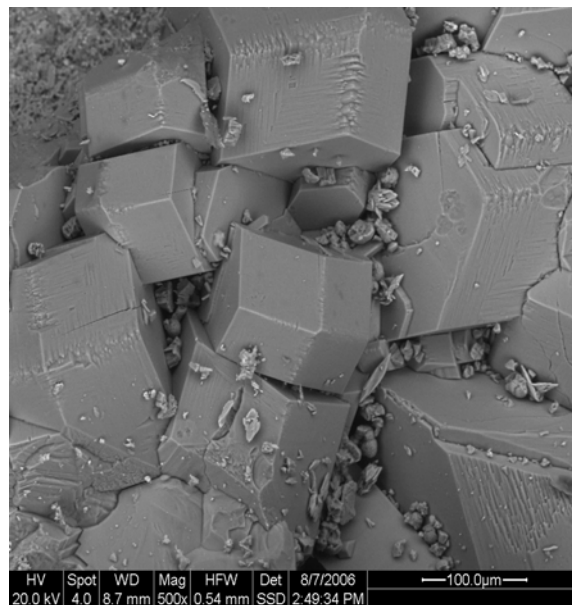


Fig. (10) SEM photo shows a prismatic phillipsite crystals from Tall Juhira.

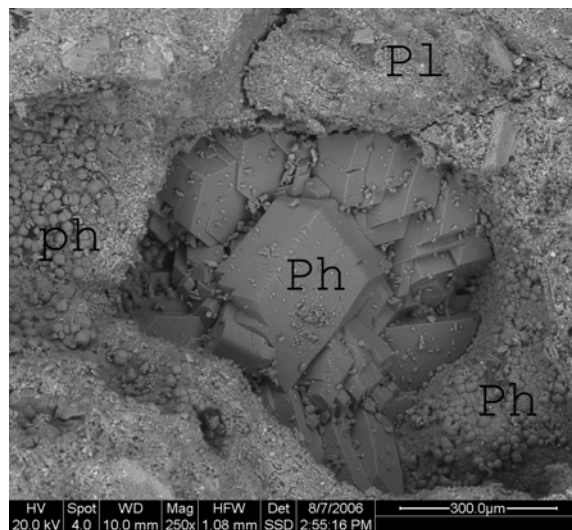


Fig. (11) SEM photo shows two generations of phillipsite crystals from Tall Amir

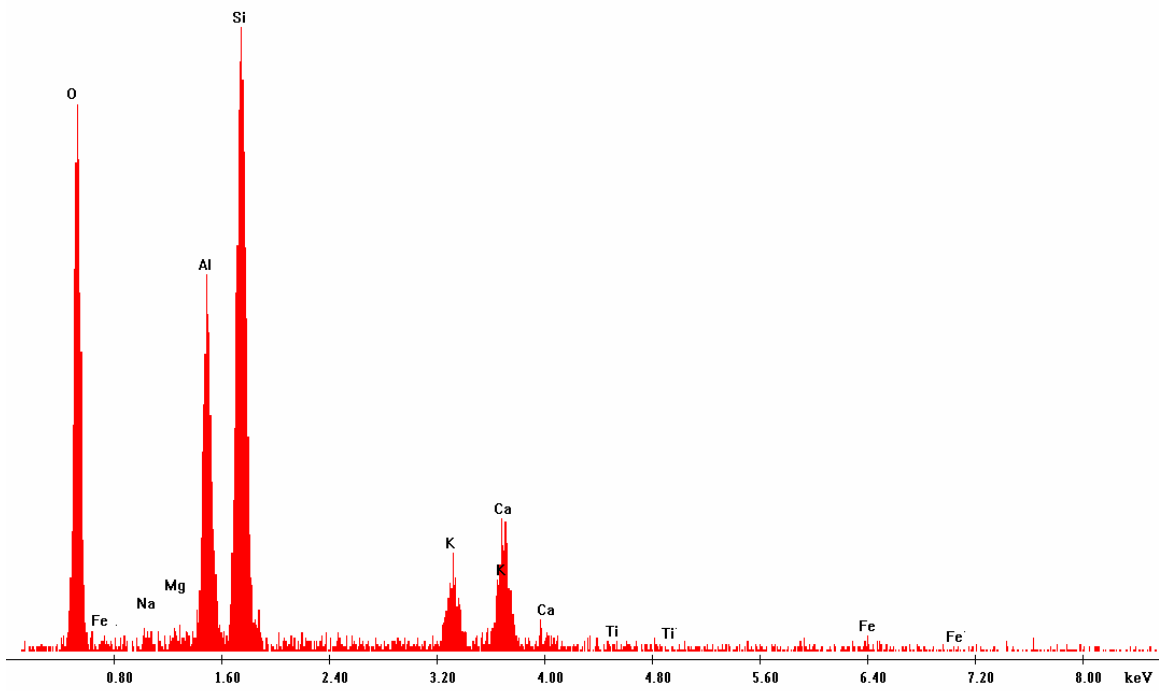


Fig. (12) Energy-dispersive X-ray results of zeolitic tuff (phillipsite) samples from Tall Juhira

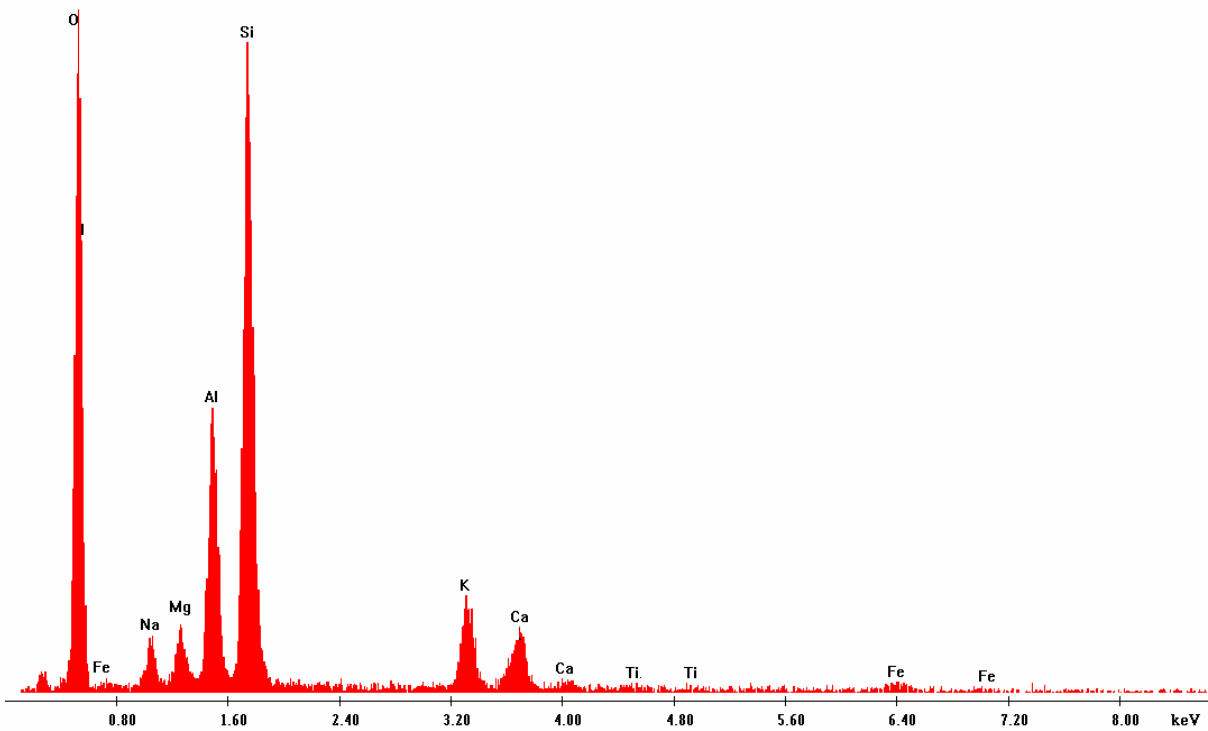


Fig. (13) Energy-dispersive X-ray results of zeolitic tuff (phillipsite) samples Tall Amir.

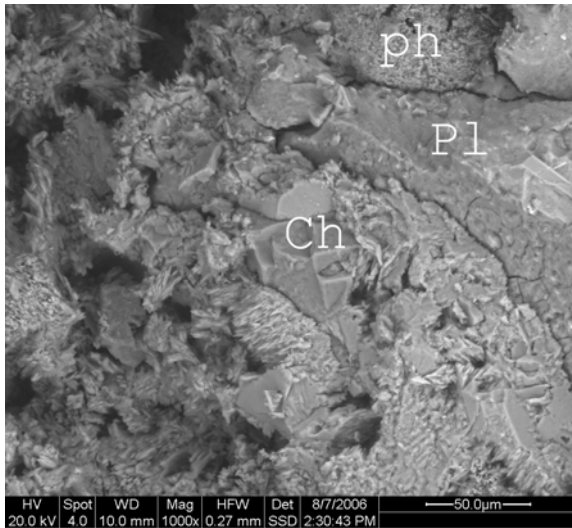


Fig. (14) SEM photo showing Simple twinning of chabazite crystals and phillipsite growth from Tall Juhira

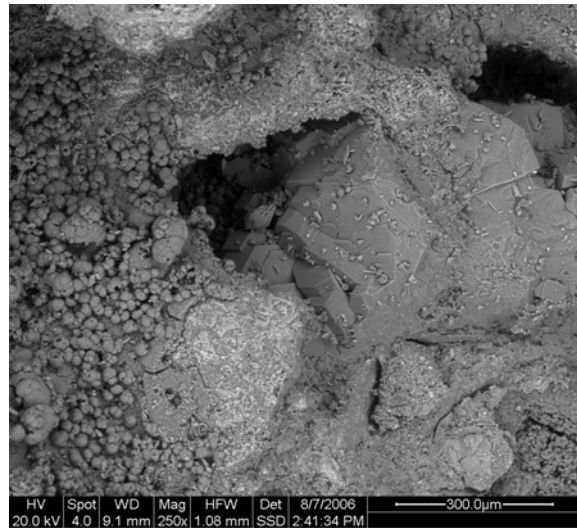


Fig. (15) SEM photo showing assemblages of chabazite from Tall Amir

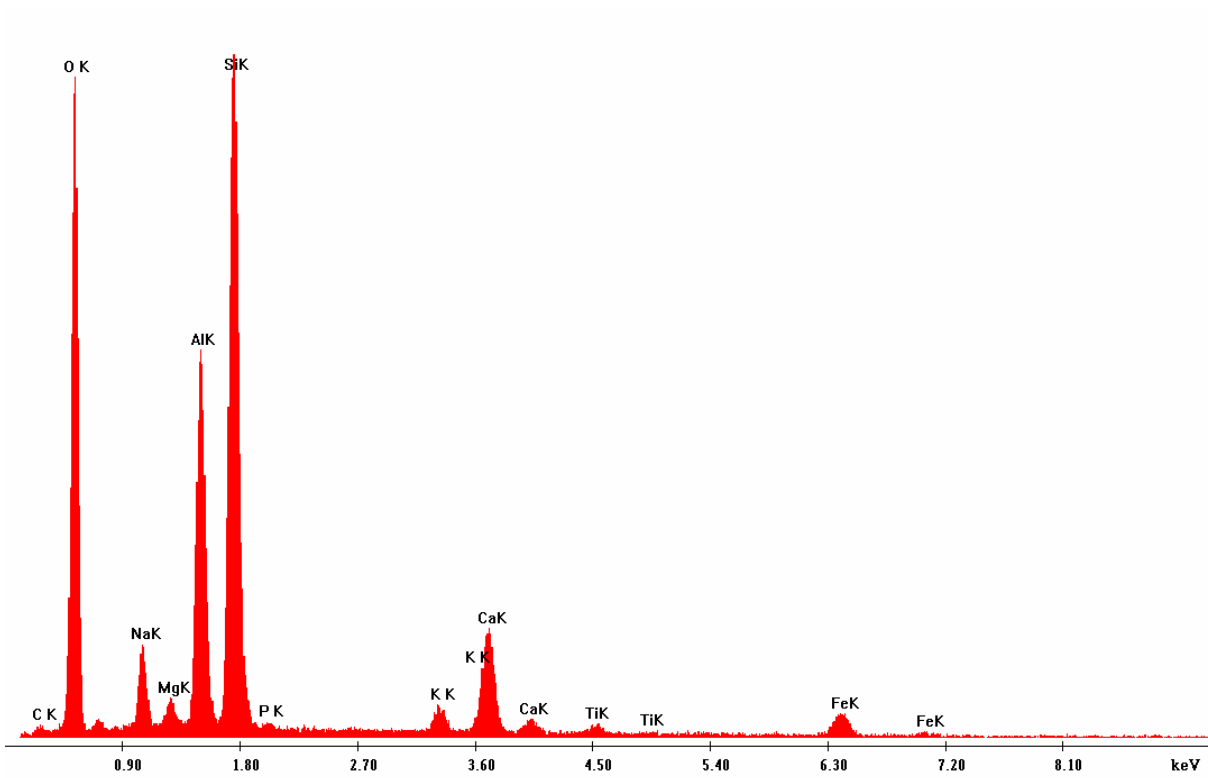


Fig. (16) Energy-dispersive X-ray results of zeolitic tuff (chabazite) for samples from Tall Juhira

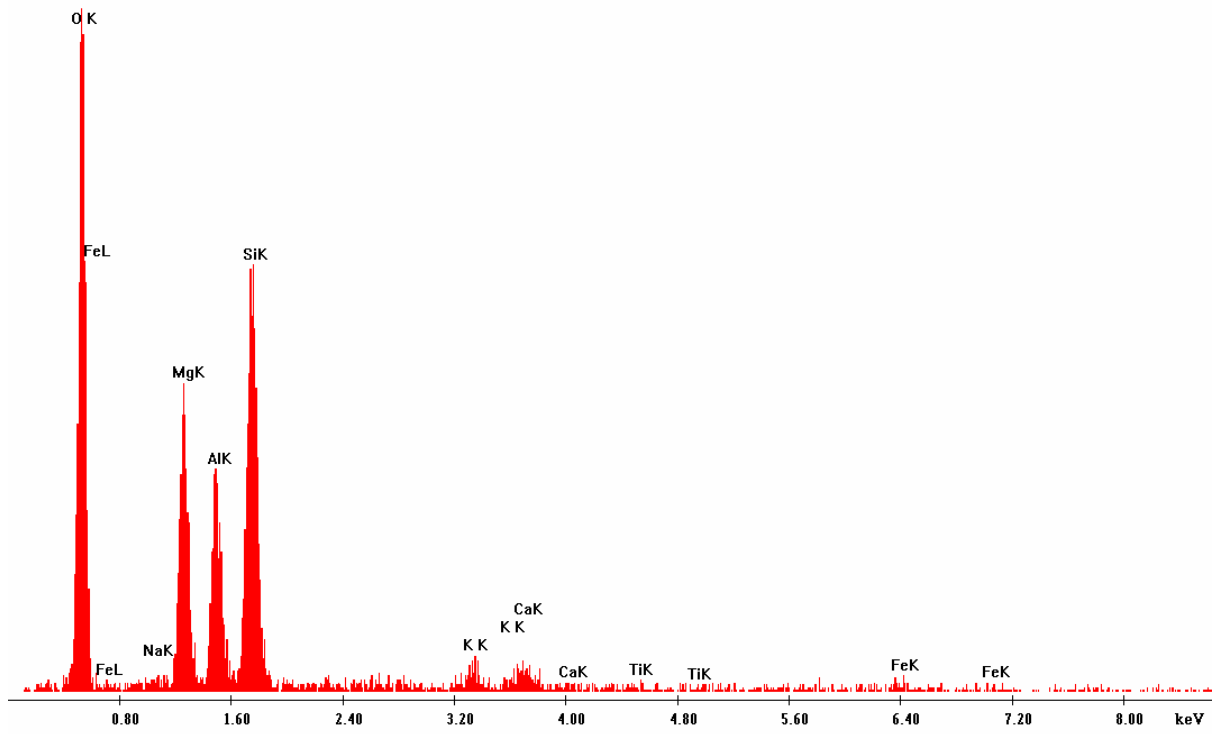


Fig. (17) Energy-dispersive X-ray results of zeolitic tuff (chabazite) the sample from Tall Amir.

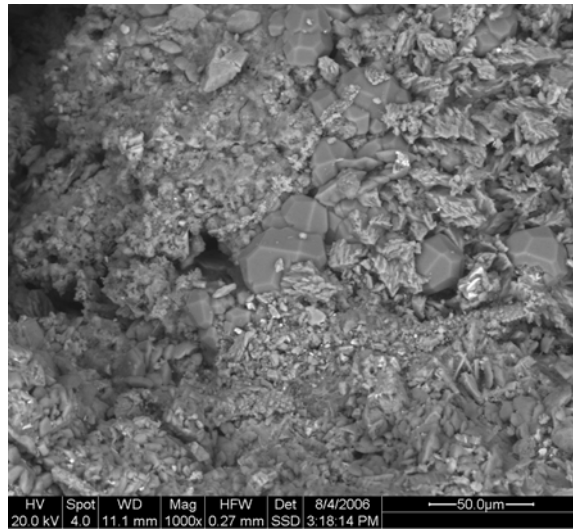


Fig. (18) SEM photo showing assemblages of analcime from Tall Amir.

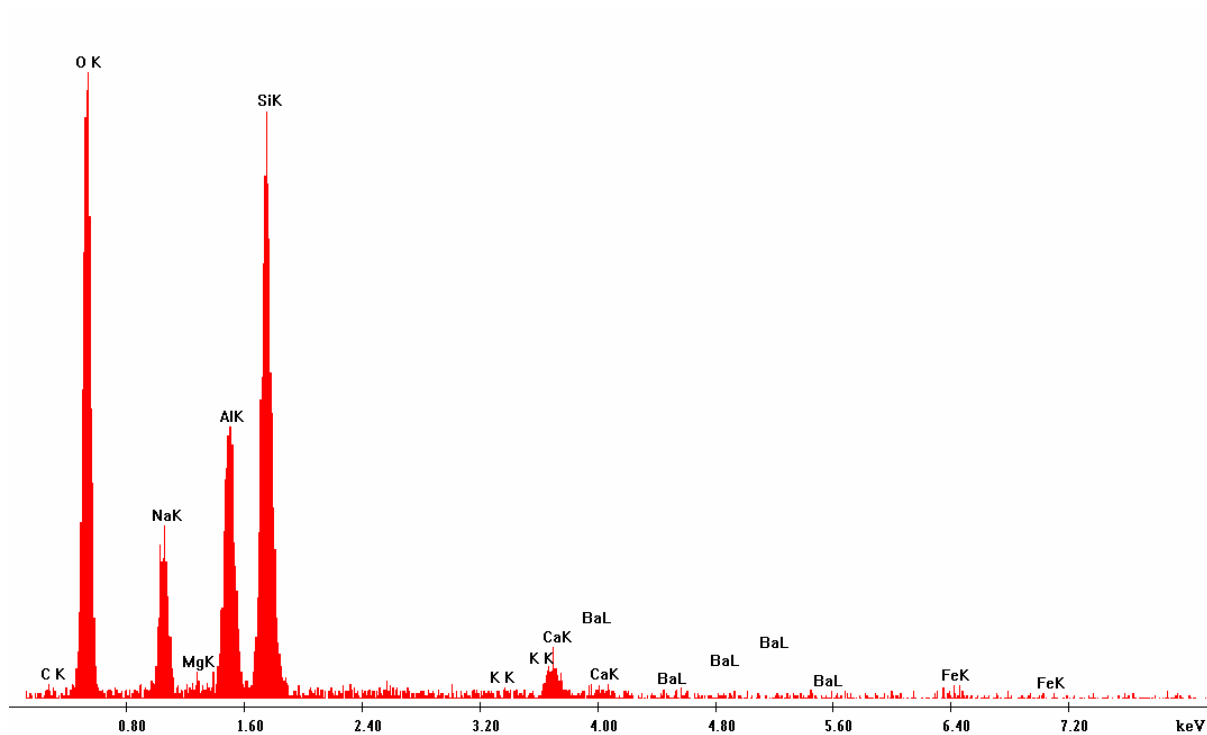


Fig. (19) Energy-dispersive X-ray results of zeolitic tuff (analcime) for sample from Tall Amir.

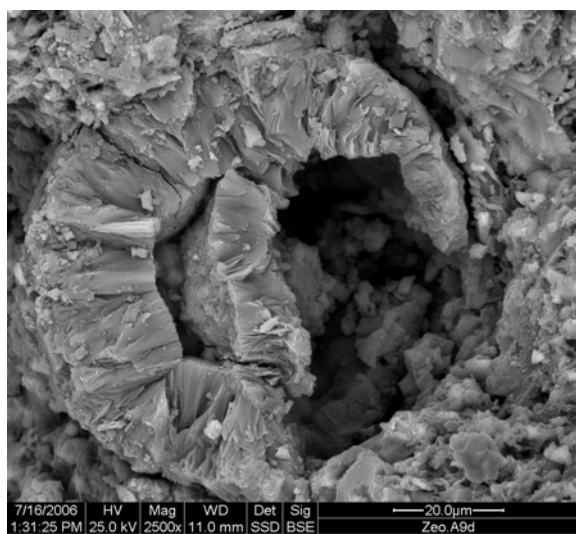


Fig. (20) SEM photo for the smectite colloform structure from Tall Juhira.

4.3 X – Ray Diffraction Results

Figures 21 and 22 are the X-ray diffraction patterns of the zeolitic tuff samples, which indicated the presence of two main groups of minerals zeolites and non-zeolites.

Table (1) illustrates the X-ray diffraction results of all the investigated sites. Table (2) gives the detailed results of the studied samples. The results are in agreement with the published data on zeolites (Breck, 1974)

The X-ray diffraction patterns show that zeolitic tuff samples contain different zeolitic minerals such as phillipsite and chabazite (Table 1). The most abundant mineral is phillipsite; and is present in all of the studied samples while chabazite is present as the second abundant mineral.

Table (1) Minerals of zeolitic tuff identified by XRD

Mineral components	minerals
Zeolitic minerals	phillipsite, chabazite, analcime
Non zeolitic minerals	calcite, olivine, plagioclase, pyroxene (augite and diopside), smectite, gypsum, hematite

Table (2) X-ray diffraction results of Tall Juhira and Tall Amir, south Jordan.

S.No	Ph	Ch	An	He	Ca	F	Di	Fo	Sm
ZTA1	*	*	-	-	*	-	*	*	-
ZTA2	*	*	*	-	*	-	*	*	-
ZTA3	*	*	-	*	*	*	-	-	-
ZTA4	*	-	*	*	*	-	*	-	*
ZTJ1	*	*	-	-	*	-	*	*	*
ZTJ2	*	*	-	*	*	*	-	-	-
ZTJ3	*	-	-	*	*	-	*	-	-
ZTJ4	*	*	-	-	*	-	*	-	*

Ph= phillipsite Ch= chabazite An= analcime He= Hematite Ca= calcite

F= feldspar Di= diopside Fo= forstrite Sm= Smectite

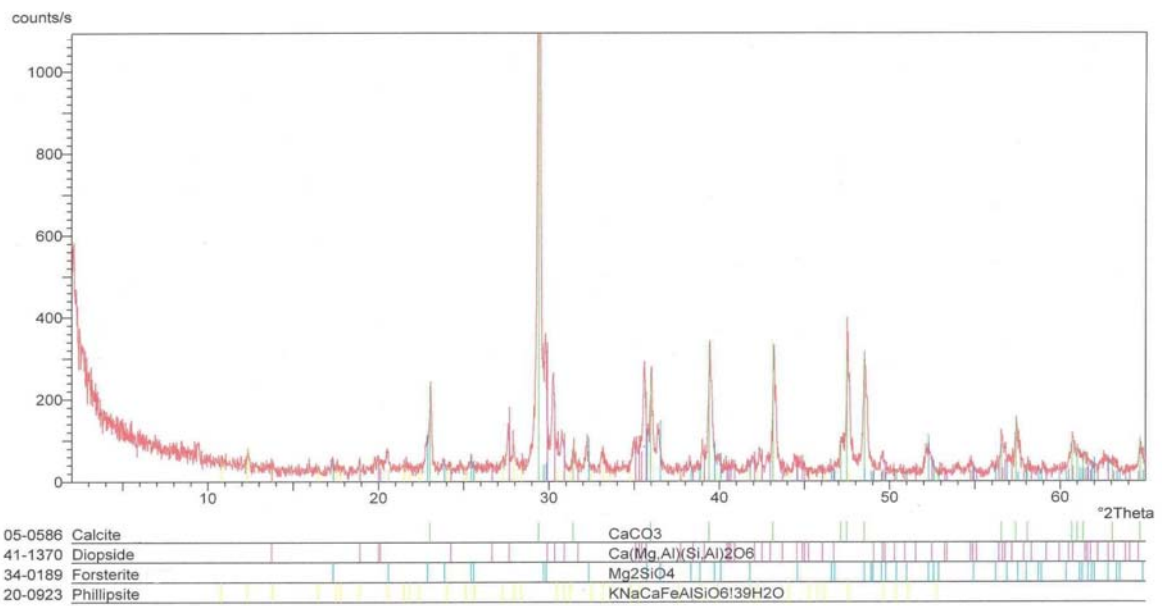


Fig. (21) X R D pattern of the zeolitic tuff sample from Tall Juhira.

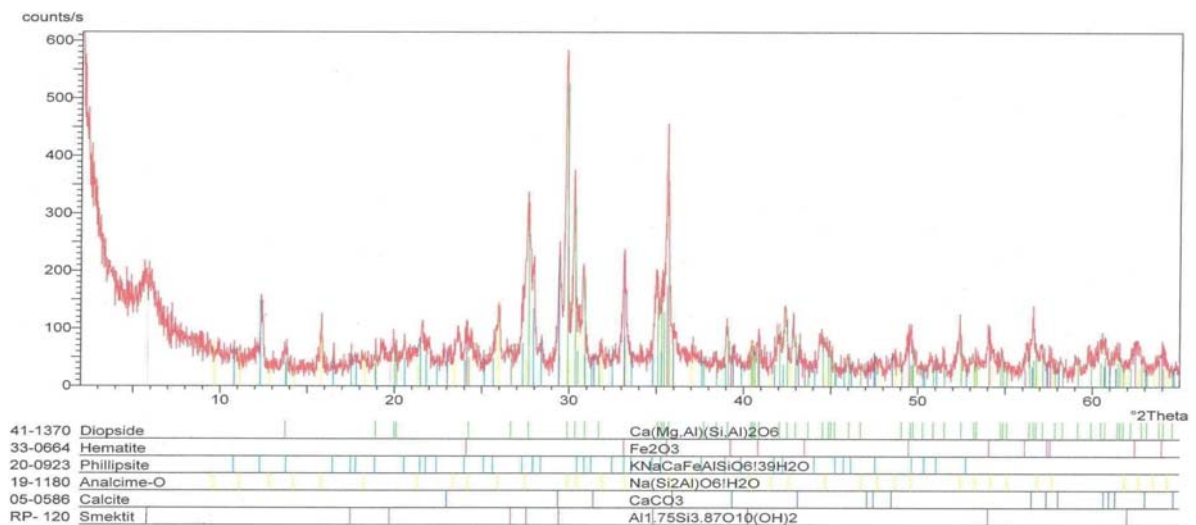


Fig. (22) XRD pattern of the zeolitic tuff sample Tall Amir.

5. Discussion

SEM/EDX, XRD and TS results have indicated that the studied tuffaceous basaltic samples are highly altered volcanic glass. The studied samples are composed of olivine, plagioclase, pyroxene, nepheline and volcanic glass. Olivine is altered to iddingsite. Plagioclase and pyroxene are altered to aluminosilicate and Fe, Mg gels. Nepheline is altered to zeolite. Zeolitic tuff is a weathering product as a result of the reaction of volcanic glass with invading percolating waters. Zeolites are most readily found in alkaline environments (pH>8) because silica is more soluble under these conditions, and thus the supply of most essential reactant is greater. Furthermore, because Ca, K and Na are essential for zeolite structure formation, zeolites tend to form in an environment where these ions are abundant (Hawkins, 1984).

In Jordan, the formation of zeolitic tuff as a result of the alteration of the basaltic tuff was studied by many authors such as (Dwairi 1987 and 1991) who described the zeolitic deposits in Aritayn area. He divided the zeolitic tuff deposits into three types depending on their degree of zeolitization as follows:

- a. Least zeolitized tuff (violet zeolitic tuff).
- b. Moderately zeolitic tuff (brownish zeolitic tuff), and
- c. Highly zeolitic tuff (reddish zeolitic tuff).

The formation sequence of Jordanian phillipsite in Aritayn area was explained by Dwairi, 1987 and 1991 as a reaction process of basaltic glass with alkaline water according to the following steps:

- d. The reaction between volcanic glass and percolating alkaline water has led to the formation of palagonite with a thin film of intergranular phillipsite.
- e. Palagonite has reacted with Mg-rich percolating solutions to form the Mg-clay.
- f. Mg-clay then was altered to aluminosilicate gel.
- g. The reaction of aluminosilicate gel with Na⁺ and K⁺ rich percolating water has led to the formation of in-situ phillipsite.

Ibrahim (1993) has explained the formation of authigenic minerals in Aritayn according to following paragenesis:

[Fresh sideromelane → palagonite → smectite → faujasite → phillipsite → chabazite → natrolite → analcime → calcite]. Hay and Lijima (1968b) reported the following sequence of authigenic minerals:

[Phillipsite → chabazite → thomsonite → gonnardite → natrolite → analcime or faujasite → montmorillonite → calcite → gypsum].

The SEM/EDX and petrographic results aided by X-ray diffraction analysis, the order of paragenesis of the principle authigenic minerals in the different localities are indicated as follow:

[Fresh sideromelane → palagonite → smectite (montmorillonite) → phillipsite → chabazite → analcime → calcite → gypsum].

The above order is similar to the paragenesis of Ibrahim (1993) and Hay and Lijima (1968b). Natrolite was not identified during the current work. Faujasite is restricted to Northeast Jordan, while analcime appears only in South Jordan. Gypsum is shown in South Jordan sequence.

6. Conclusion

1. Tall Juhira and Tall Amir are two important Jordanian zeolitic tuffs outcropping in southern Jordan.
2. The Jordanian zeolitic tuff is highly weathered and is altered mainly to zeolites (chabazite, phillipsite, and analcime), clay minerals, calcite, gypsum, and hematite.

References

- [1] Banfield, J., Barker W., Welch S., and Taunton, A., (1999) Biological impact on mineral dissolution: Application of the lichen model to understanding mineral weathering in the rhizosphere. Proceedings of the National Academy of Science, USA.
- [2] Breck, D., (1974) Zeolite molecular sieves, structure, chemistry and use. Wiley-interscience, New York. 771p.
- [3] Dwairi, I., (1987) A chemical study of the palagonitic tuffs of the Aritayn area of Jordan, with special reference to nature, origin and industrial potential of the associated zeolite deposits, PhD thesis, Hull Univ., UK, 408 P.
- [4] Dwairi, I., (1991) Evaluation of Jordanian phillipsite tuff in removal of ammonia from wastewater: Experimental study. Al- Belga Journal, Vol. 153-66.
- [5] Eggleton, R., (1984) Formation of iddingsite rims on olivine: a transmission electron microscope study. Clays and Clay Minerals, 32, 1_11.
- [6] Hawkins, A., (1984) kinetics of glass dissolution and zeolite formation under hydrothermal conditions. Clay Minerals, 29, 331-340.
- [7] Hay, R., and Lijima, A., (1968) Nature and origin of palagonite tuffs of the Honolulu group on Ohahu. Hawaii, Geol. Soc. America Mem., 116, 331-376.
- [8] Honnorez, J., (1981) The ageing of the oceanic lithosphere. In E. Emiliani (ed). Wiley New York, 7, 525-567.
- [9] Ghir, A., (1998) The distribution, nature, origin, and economic potential of zeolite deposits in Uneiza, Mukawir, and Tell Hassan of Jordan. Unpublished M. Sc. Thesis, University of Jordan, Amman, Jordan. 169 p.
- [10] Ibrahim, K., (1987) Geochemistry and petrology for some of the basaltic outcrops in central Jordan. M. Sc. Thesis, University of Jordan, Amman, 164p.
- [11] Ibrahim, K., (1993) The geological framework for the Harrat Ash-Shaam Basaltic super-group and its volcano tectonic evolution. Natural Resources Authority, Geological Mapping Division, Bulletin 25, Amman, 33 P.
- [12] Kerr, P., (1977) Optical mineralogy. Forth Edition, Stanford University
- [13] Smith K., Milnes A., and Eggleton R., (1987) Weathering of basalt, formation of iddingsite. Clays and Clay Minerals, 36, 418_428.
- [14] Willson, M., (2004) Weathering of the primary rock-forming minerals: processes, products and rates. The Macaulay Institute, UK.

Cementation of Silver Ions on Metallic Copper

Marian Jaskuła

Jagiellonian University, Department of Physical Chemistry & Electrochemistry, 30-060 Cracow (Poland)

Abstract

The silver ion cementation on metallic copper was investigated in the presence or absence of oxygen. The influence of sulphuric acid and copper sulphate concentration on the silver cement morphology was studied in details, and results were linked with the previously determined kinetics data of the process. The morphology of silver deposit was found to be independent of the presence of oxygen in the system as well as the sulphuric acid concentration. Contrary, the concentration of copper sulphate strongly influenced the morphology of silver deposit. Two-stage mechanism of cementation was proposed.

© 2009 Jordan Journal of Earth and Environmental Sciences. All rights reserved

Keywords: Silver ion cementation, cementation on copper, kinetics of cementation, surface morphology.

1. Introduction

One of the oldest and most effective hydrometallurgical processes which allow recovering metals from solutions is cementation. This process is known since the ancient times of human culture, but in Europe the early knowledge of cementation spread only at the beginning of the Middle Ages. The famous medieval work of Agricola *De Re Metallica* should be mentioned here (Fig.1). At that time, the cementation process was used by alchemist in order to perform the transmutation of metals. For several decades, cementation has been commonly used in the industry for the recovery of metals, removal of metal ions from dilute wastes and purification of solutions.

Many new technologies used in the environmental protection and purification are based on cementation. The main advantage of this process is the possibility of removal of ions of very low concentrations (traces) from the great volumes of various electrolytes (i.g. in situation where other methods are much more expensive or unapplicable).

Typical industrial applications of cementation are:

- of copper with iron (for example the production of copper metal in the refinery Rio Tinto in Spain),
- of gold from cyanide solutions with zinc powder,
- of cadmium ions (purification of zinc sulphate solution) during zinc processing.

Intensive investigations on cementation process have been undertaken recently which allowed to attain significant improvement in technology and in apparatus construction like the introduction of industrial practice of the so called cementation towers, instead of leaching tanks used until now.

Although cementation has been used in practice for a long time, the theoretical backgrounds of this process still

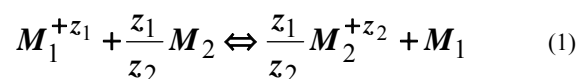
remains questionable. There are lots of papers devoted to cementation of various ions, but usually they are concerned about the kinetics of process and not about the mechanism itself. The problem becomes even more complex when the metal used for cementation of the ions may occur at different states of oxidation.

One of the important fields for the use of cementation is the recovery of noble metals, and we have concentrated our interest on the cementation of silver ion on metallic copper from industrial baths, used for electrowinning and electroplating of copper and containing sulphuric acid and copper sulphate. This problem has a great importance not only for the recovery of silver but also to obtain high purity copper for electronic purposes.

This problem is especially important in Poland, because concentration of silver in Polish copper ores is relatively high.

2. Theory

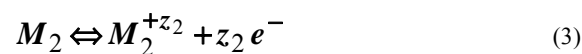
The overall cementation reaction can be expressed by the following equation:



Cementation process present a system of many short-circuited microcells and the overall reaction can be expressed as the sum of half-cell reactions:

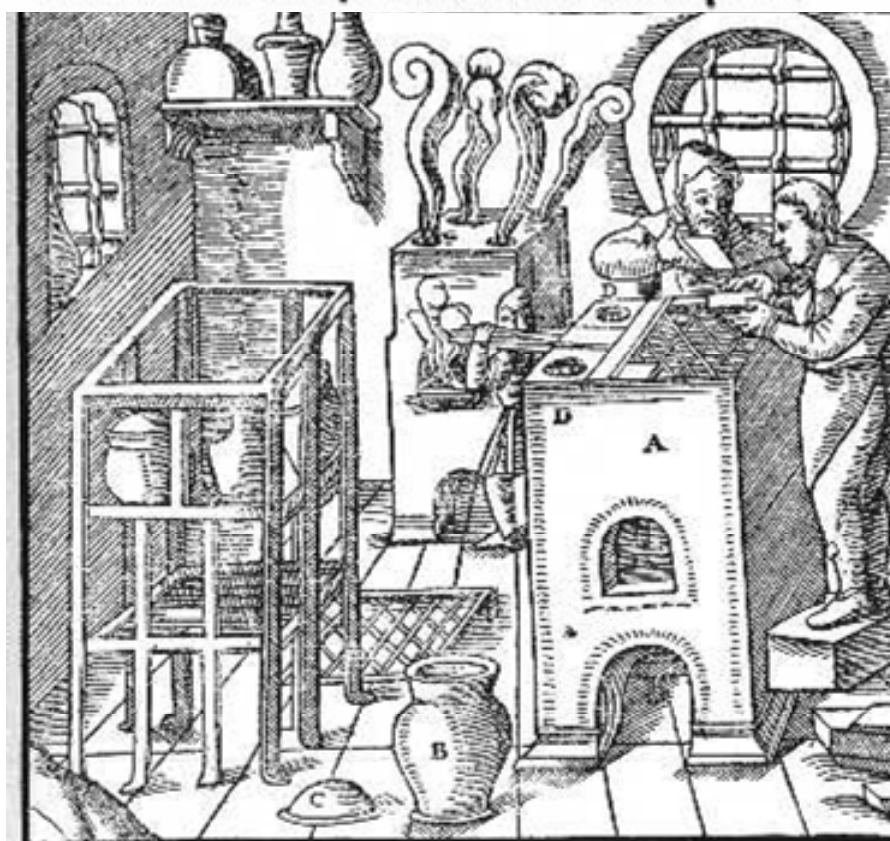


and



Cementation is an electrochemical process, but it differs from the electrolytic deposition where the electrons are supplied from the external source as well as from

GEORGII AGRICOLAE DE RE METALLICA LIBRI XII QVI bus Officia, Instrumenta, Machinæ, ac omnia deniq; ad Metallis tam spectantia, non modo luculentissimè describuntur, sed & per effigies, suis locis insertas, adiunctis Latinis, Germanicisq; appella tionibus ita ob oculos ponuntur, ut clarius tradi non possint.



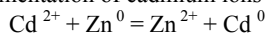
A—FURNACE. B—POT. C—LID. D—AIR-BLOWER.

Fig.1 The reprint of the book De Re metallica from Agricola

electroless plating where the oxidation of an organic additive occurs.

For many cementation reactions, free enthalpy ΔG has very high negative value therefore, from thermodynamic point of view, these reactions go to completion.

The change of ΔG can be evaluated from the standard potentials of given half cells. For example for the cementation of cadmium ions on zinc one has



The change of free enthalpy ΔG is given by

$$\Delta G = -nFE^0$$

where E^0 is the standard emf of the appropriate cell and F and n are Faraday constant and the number of electrons respectively.

Thus

$$\Delta G = -2 \text{ equl/mol} * 23.06 \text{ kcal/volt.equl} * 0.36 \text{ V} = -16,6 \text{ kcal/mol}$$

And one can further calculate that the reaction attains equilibrium if

$$\frac{a_{\text{Zn}^{2+}}}{a_{\text{Cu}^{2+}}} > 10^{12.2} \quad (4)$$

3. The simple model of cementation reaction

The simple accepted model of cementation is based on two assumptions:

1. Appearance of many anodic and cathodic places on the surface of more negative metal (dissolving metal)
2. Reduction of ions of more noble metal in the Helmholtz layer at cathodic places.

For the heterogeneous cementation reaction at the smooth metal surface under well defined hydrodynamic conditions and in the absence of other “impurities”, generally two processes are proposed to take place: 1) surface reactions and 2) mass transport.

Usually the chemical processes (surface reactions) are faster than the transport processes, and therefore the total rate is controlled by the transport process. In such cases of transport limitation, one can expect the kinetics of first order.

The increase in temperature results in increasing the total process rate, independently of limiting stage, but the observed effect is bigger in the case of chemical reaction control. The investigation of the temperature influence is important because it allows one to understand the nature of limiting stage.

Among the various factors that influence the process and its kinetics the following should be also mentioned

- the form and shape of deposit (cementate),
- the presence of “impurities” e.g. compounds which influence the stoichiometry and kinetics of reaction.

Mass transport takes place by convection, migration of ions under electric field, or by diffusion caused by concentration differences. Under given circumstances, it is possible to calculate the mass transport rate and compare it with experimental values. Finding which transfer mode is process-limiting is important to find out whether the surface reaction, which is going slowly, or that the mass transfer through cementate deposit layer, is in control of the process.

The description of kinetics of cementation process is similar to the metal deposition and the process rates may be expressed by the current densities. A more detailed analysis, made by Wadsworth [1], gives the following equation describing the rate of cementation reaction

$$\frac{dc_1}{dt} = c_1 k_0 \left(1 - \frac{c_2^{z_1/z_2}}{c_1} \exp \left[\frac{-z_1(E_2^0 - E_1^0)F}{RT} \right] \right) \quad (5)$$

where

- c_1 - concentration of noble metal ion M^{+z}
- c_2 - concentration of active metal ion M_2
- z - charge of ion
- E^0 - standard half-cell potential
- k_0 - rate constant (the complex function of overpotentials, potential drop in double layer, diffusion coefficients etc).

Based on equation (5), the back reaction is important when

$$\frac{c_2^{z_1/z_2}}{c_1} \exp \left[\frac{-z_1(E_2^0 - E_1^0)F}{RT} \right] > 10^{-2} \quad (6)$$

Usually the above condition (equation 6) is not fulfilled, and the rate of backward reaction is very small. The backward reaction should be taken into account only if the difference of standard potentials is about 0.5 V.

The cementation reaction is of the 1st order with respect to the concentration of metals ions:

$$\frac{dc_1}{dt} = k \frac{A}{V} c_1 \quad (7)$$

and its rate depends strongly on surface area (A) and electrolyte volume (V). Other parameters like initial concentration of ions, temperature, stirring, current density, presence of additives or other complex forming substances influence the magnitude and character of active area of electrode. The influence of these parameters is as follow:

- in thick crystalline, incompact and spongy deposits are created at higher temperatures, higher current densities and higher concentrations of metal ions,
- while the organic additives (like glue, gelatine), lower concentrations of metal ions and lower temperatures prefer deposition of shiny and fine crystalline deposits.

The present review is based on papers published by the author [2-8] concerning the kinetics and mechanism of silver ion cementation on metallic copper, Different results that are devoted to the morphology of the silver deposit were obtained under various experimental conditions. The detailed mechanism of the proposed process is also presented.

4. Experimental Work

Cementation experiments were carried out, using the rotating cylinder system, allowing the controlled hydrodynamical conditions (Fig. 2).

The rotating cylinder, made from stainless steel, had the working surface area of 27.50 cm². The cementation cell has the volume of 200 cm³. All solutions before the use were purged by bubbling with high purity argon or high purity oxygen for 20 minutes. The oxygen free atmosphere or oxygen atmosphere was also maintained over the solution throughout the whole duration of the process. Before each cementation experiment, the surface of the cylinder was covered electrolytically with fresh layer of copper. The copper layer was then polished electrolytically, rinsed and dried.

The changed parameters of cementation experiments were: concentrations of copper sulphate and sulphuric acid, initial concentration of silver ion and temperature.

During the experiment, the samples of solution were taken for the determination of the silver concentration by atomic absorption spectrometry (AAS) using the Philips PU 9100X. Additionally, the concentration of silver ion was monitored during the cementation by measuring the potential of silver ion selective electrode (EMF) immersed into the solution.

After each run, copper with cemented silver was rinsed, dried and carefully separated from the cylinder. The samples were dissolved in nitric acid and analysed for silver content. Also the SEM pictures of the surface

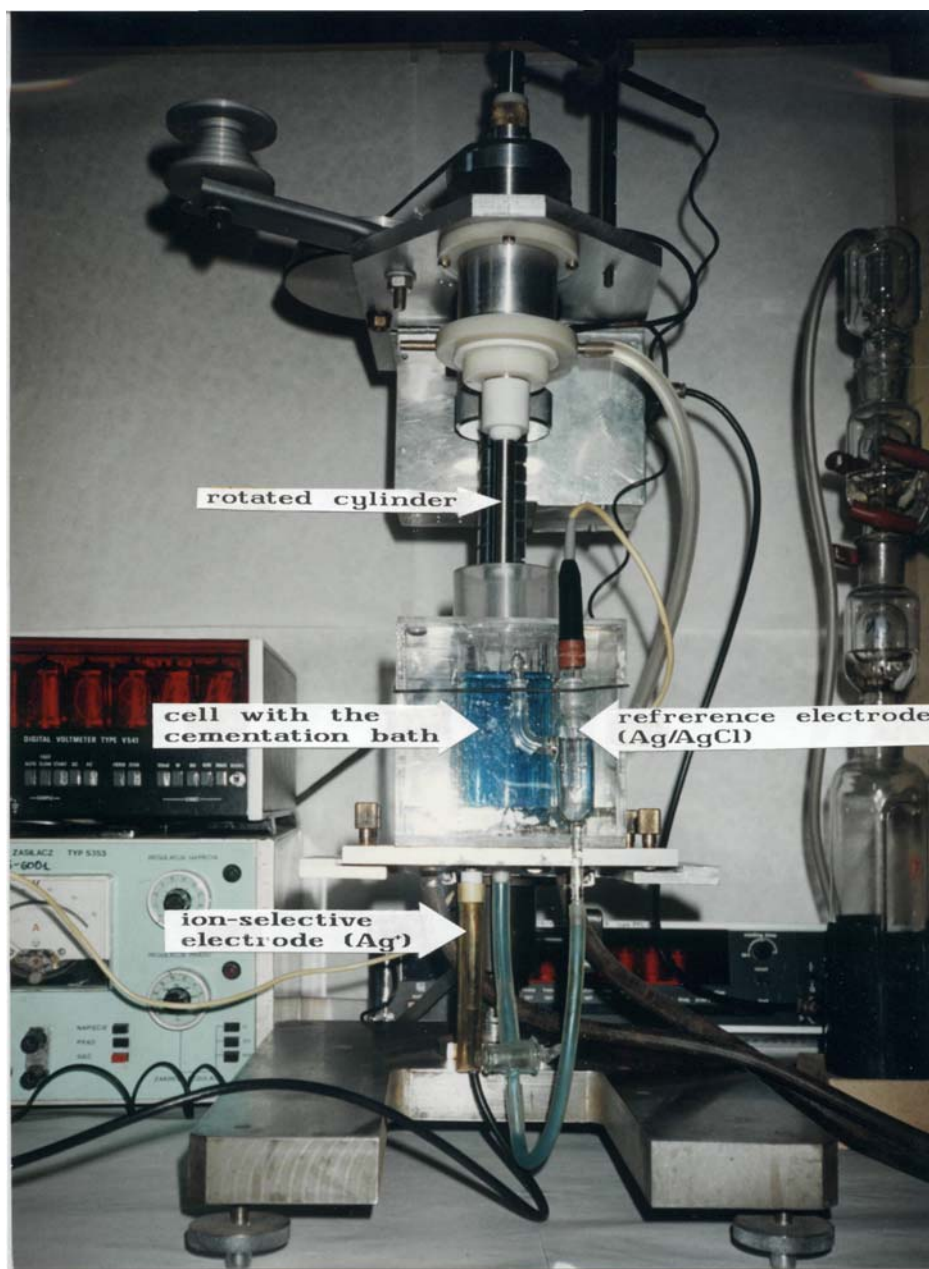


Fig 2 The rotating cylinder system used for investigation of cementation.

deposit were recorded. All details of experiments and used apparatuses were described in details previously [3, 6].

5. Results and Discussion

Fig.3 shows some examples of kinetics plots. It is seen that both used independently analytical methods i.e. atomic absorption spectroscopy (where total silver content was found in solution) and ion-selective electrode where only ionic part gave the same (or similar) results only in the case when the oxygen was presented in the system over the whole duration of the experiment. In the deoxygenated solutions and after first few minutes of experiment, the growing discrepancies were observed.

For the initial period of cementation the linearity of the concentration versus time plot (Fig. 4) was retained. This is in agreement with the assumption about 1st order reaction. Therefore the appropriate rate constants were determined.

Table 1 shows the values of activation energy calculated from the experimental data and compared with theoretical values obtained based on the Pang-Ritchie equation describing the transport to the rotating cylinder [10]. The tabulated values confirm that the cementation process kinetics, at its initial step, is of first-order.

Fig.5 shows SEM images of cemented silver which were formed during the cementation conducted in 0.5 M sulphuric acid without copper sulphate taken from different parts of the surface. The value of Θ denotes the percentage of cemented silver on copper in comparison

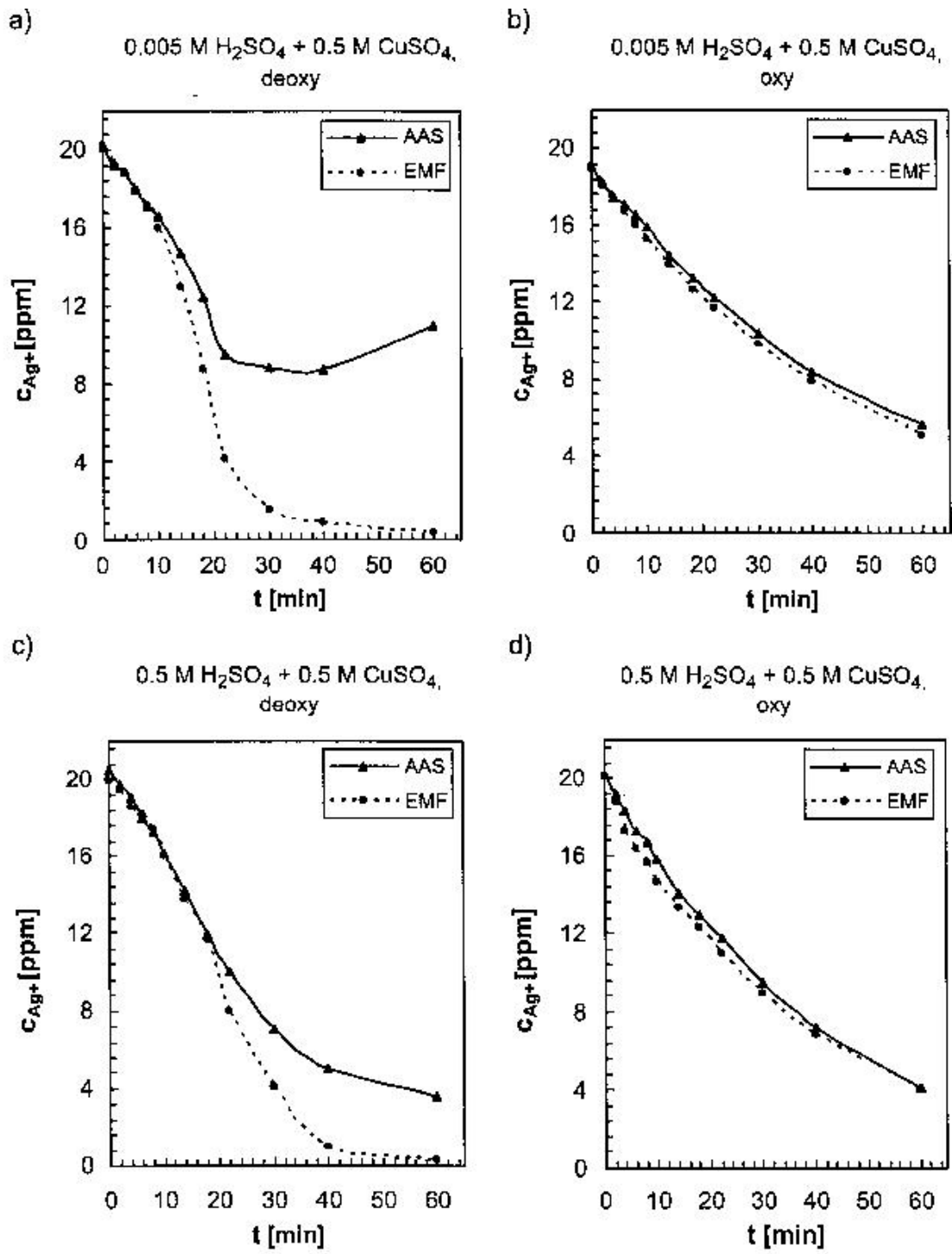


Fig.3 Variations in [Ag⁺] concentrations with time in deoxygenated and oxygenated solutions 298K, [Ag⁺]_{initial} = 20 mg/L, f = 500 rev/min, [CuSO₄] = 0.5 M, [H₂SO₄] = 0.5 M or 0.005M

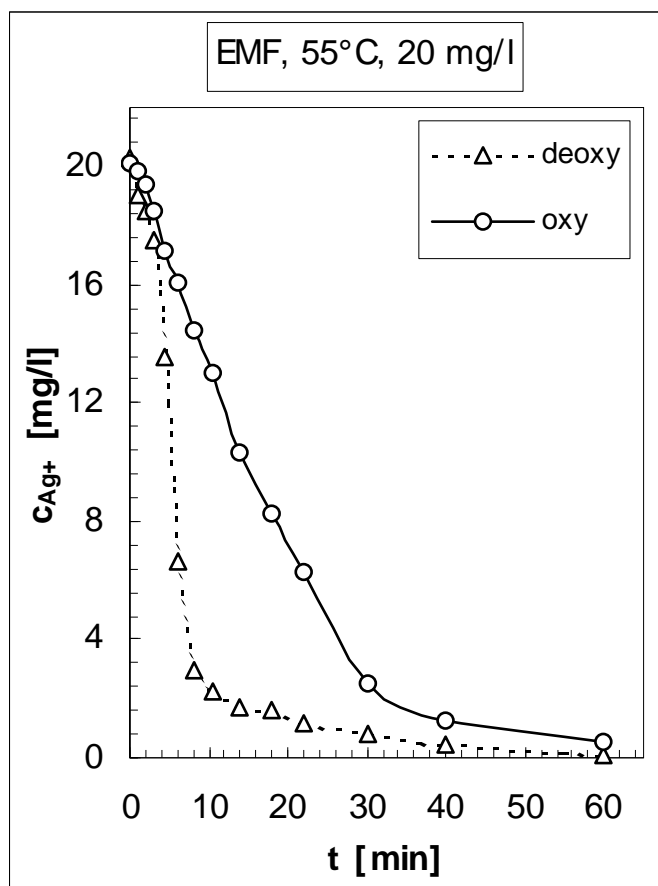


Fig 4. Concentration of silver ion versus time of cementation

Table 1. Activation energy values for the initial period of cementation

Conditions	Temperature range [°C]	E _a [kJ · mol ⁻¹]		
		P-R	AAS	EMF
20 mg/L Ag ⁺				
deoxy	7-55	16.14	21,35 ± 0.38	20.45 ± 0.29
oxy			15.61 ± 0.40	15.78 ± 0.84
100 mg/L Ag ⁺				
deoxy	15-55	16.14	19.36 ± 0.49	19.03 ± 1.04
oxy			18.63 ± 0.45	18.13 ± 0.10

with the initial silver content in solution, determined by the AAS method. It was found that the morphology of cemented deposit is highly non-uniform. Some parts of copper surface are covered with tiny Ag crystals (Figs 5A and 5B), but other parts are occupied by “fern leaf-shaped” dendrites. There is no visible effect of the oxygen presence on the morphology of formed silver deposit.

The presence of oxygen in the system does not modify the tight Ag deposit as well as Ag dendrites. On the relatively smooth parts of silver deposit (Figs. 5A and 5B), germs of pre-dendrites are already visible as white spots. These germs can further develop in huge silver dendrites as we can see in Fig 5C and 5D.

Fig. 6 shows the typical curve log c_t/c₀ versus time and illustrates the moment when in the smooth surface of

cementate, the dendrites start to grow. Moreover, figure 7 shows the dendrites observed in the solution where a little amount of copper sulphate was introduced (concentration of CuSO₄ 0.005 M). When the concentration of copper sulphate in the solution was increased (up to 0.5 M), no dendrites were found on the surface and the surface was smooth (Fig. 8).

In Table 2, the Θ values (percentage of cemented silver found on the surface) are shown. The amount of cemented silver remains constant in oxygenated solution but in the absence of oxygen it depends strongly on the content of copper sulphate and sulphuric acid.

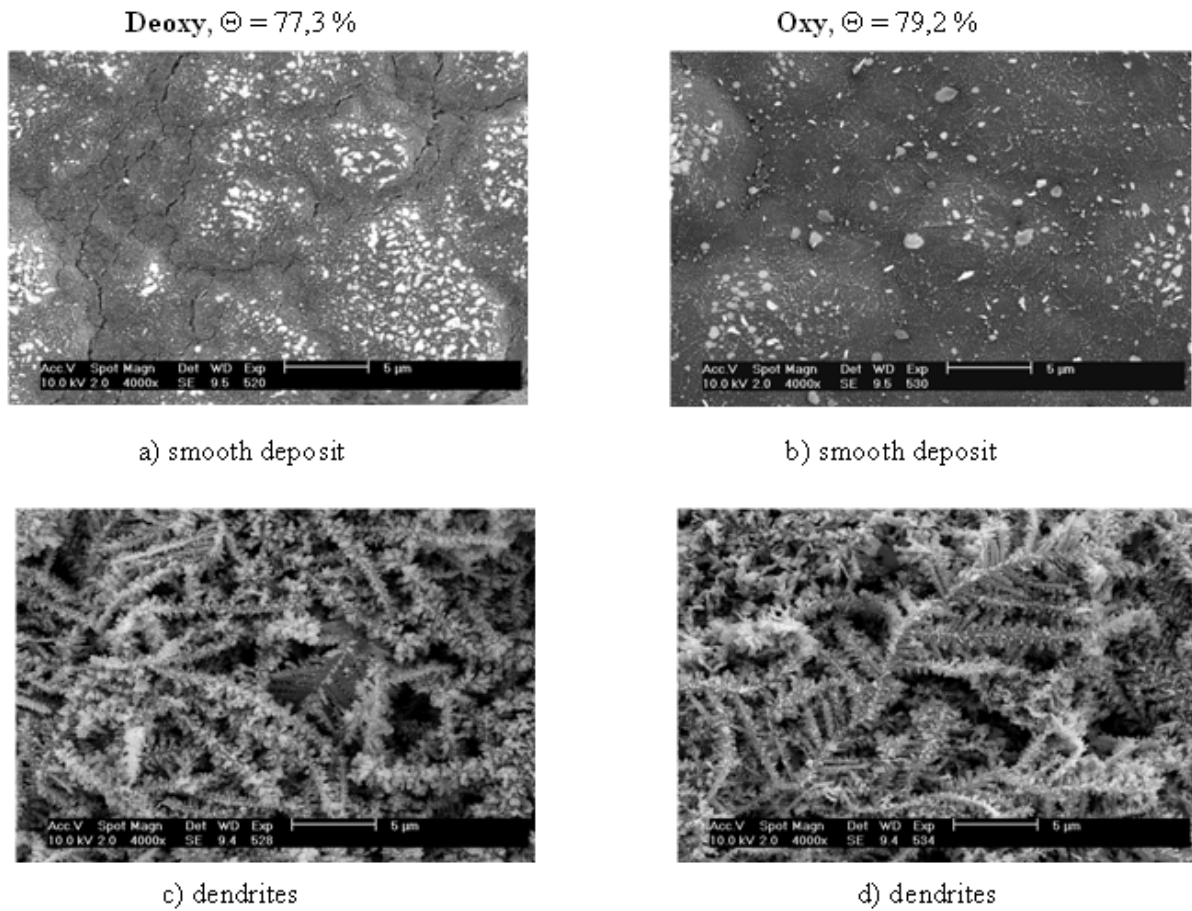


Fig. 5 SEM micrographs of Ag cements obtained from 0.5 M H₂SO₄.

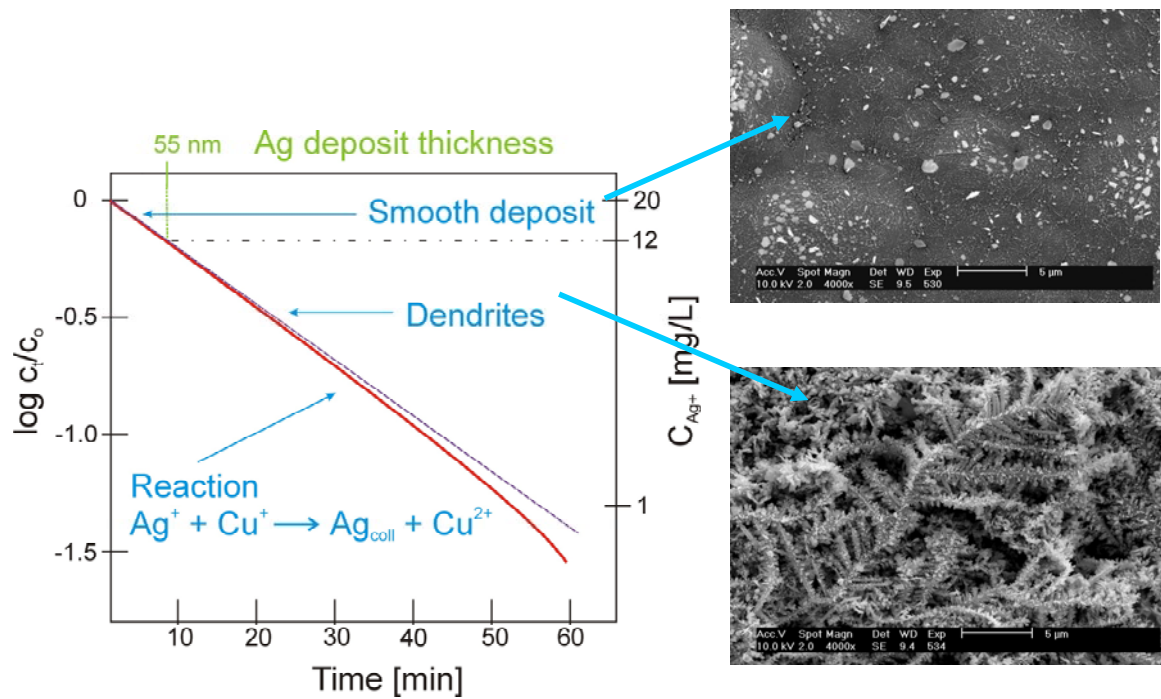


Fig. 6 The growing of dendrites

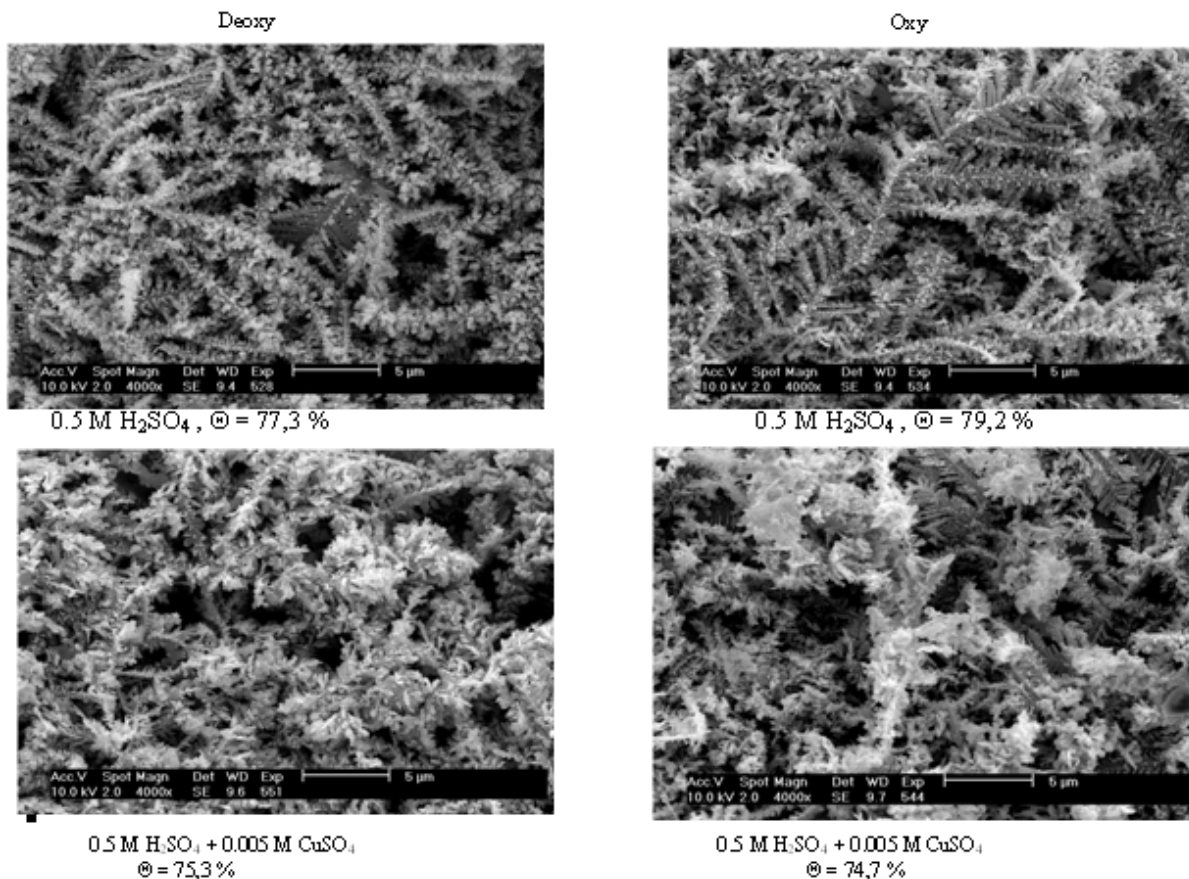
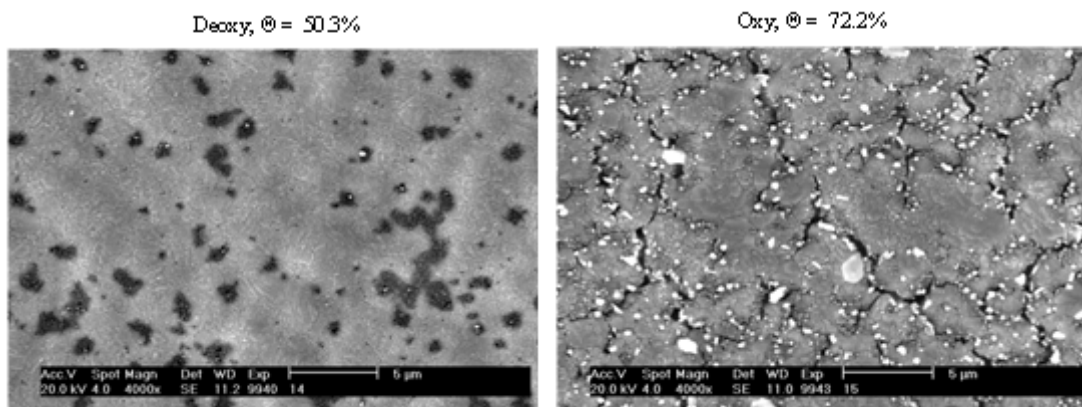


Fig. 7 SEM top-view images of the surface with cemented silver formed in the deoxygenated or oxygenated solution containing 0.5 M H₂SO₄ and 1.85 × 10⁻⁴ M Ag⁺. Cementation was conducted for 60 min at 25°C. (a and b) Smooth deposit and (c and d) Ag dendrites.



Only smooth surface without dendrites

Fig. 8 SEM top-view images of the surface with silver deposited in a 0.5 M H₂SO₄ + 0.5 M CuSO₄

Tab 2. The percentage of cemented silver on copper

Composition of solution		deoxy		oxy	
C _{H2} SO ₄	C _{Cu} SO ₄	n	Θ [%]	n	Θ [%]
0,5	0	3	77.7	3	78.4
0.5	0.005	4	78.0	4	77.5
0.5	0.05	3	64.7	3	71.8
0.5	0.5	9	52.7	6	73.8
0.005	0.5	3	37.6	3	74.8

The above results allow proposing the two-stage cementation process mechanism as shown in Fig. 9 and described by the following steps:

Step 1:

The first step of the cementation reaction generates Cu^+_{ad} ions in both deoxygenated and oxygenated solutions.

Step 2:

The second step is different and depends on presence or absence of oxygen:

- In oxygenated solution, the part of copper (I) ions created during the first step at the copper surface reacts immediately near to this surface with diffusing silver ions. The other part starts to diffuse away into the bulk of solution but on the way the copper (I) ions meet the oxygen and transform to the non reactive copper (II) ions.

- In the deoxygenated solution the copper (I) ions diffuse without obstacles into the bulk and then they react with silver ions creating the silver colloid. In many cases, the subtle haze of silver colloid was observed.

Sulka and Jaskula [3] showed that in the deoxygenated solution containing 0.5M H_2SO_4 and 0.5 M $CuSO_4$ the consumption of about 8 mg/L of silver ions (their concentration at the beginning was 20 mg/L) in cementation process corresponds to the production of about 4.7 mg/L of copper (I) ions. This concentration is high enough to initiate the progress of the reaction between Cu^+ and Ag^+ ions in the bulk of solution. Thermodynamics calculations⁽¹⁾ show that practically all silver ions could be cemented before reaching the equilibrium between copper (I) and copper (II) ions.

Mechanism of cementation

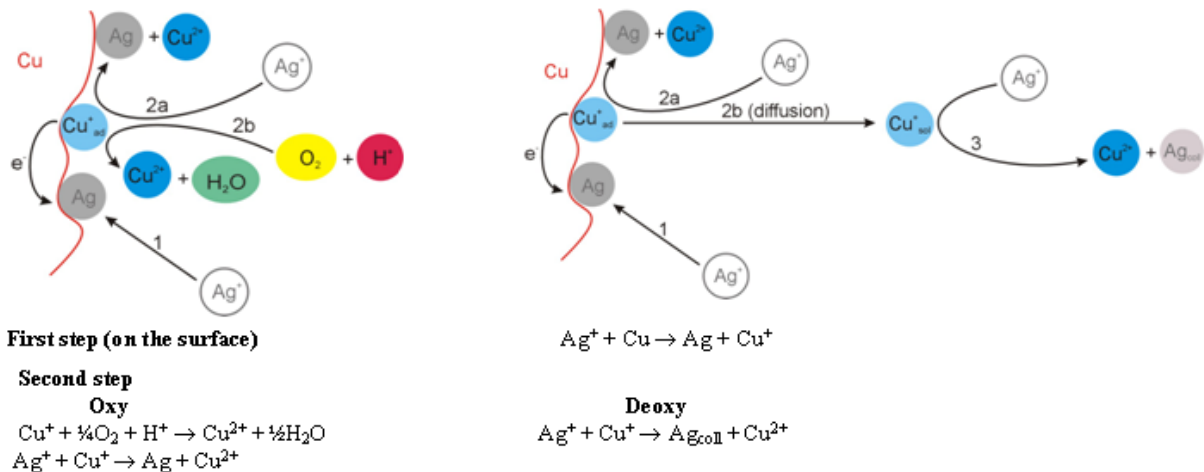


Fig. 9 Mechanism of silver ion cementation.

The SEM images presented in Fig. 10 show formation of cathodic sites on the reacting surface in the cementation process. The images were taken from various sites of the same sample. The study was performed for a cementation test conducted in deoxygenated solutions containing 0.5 M H_2SO_4 . At the beginning of the process, silver covers uniformly the copper surface as shown in Fig. 10A. Ag crystallites are very small and cover surface uniformly and compactly. Regular, hexagonal, sticking out Ag crystals are also visible on the surface. There are germs of dendrite growth.

¹Calculations:

There are two ionic equilibria in the studied system

$$(a) 2Cu^+ = Cu + Cu^{2+}$$

$K_a = [Cu^{2+}]/[Cu^+]^2 = 1.13 \cdot 10^6$ (at 298K). It means that the equilibrium concentration of Cu^+ ions is equal to $6.6 \cdot 10^{-4}$ M. and

$$(b) Cu^+ + Ag^+ = Cu^{2+} + Ag_{colloid} \quad \Delta G^0 = -61.6 \text{ KJ}$$

$$\Delta G^0 = -RT \ln K \text{ since } K_b = [Cu^{2+}]/[Cu^+][Ag^+] = 6.3 \cdot 10^{10}$$

From the above values, equilibrium constants may be calculated that

if $[Ag^+] = 1.85 \cdot 10^{-5}$ M i.e. 90% was cemented

then $[Cu^+] = 4.3 \cdot 10^{-7}$ M

Afterwards, a growth of dendrites is initiated on preferential parts of the surface, usually on small protrusions (Fig 10B). At the early stage of dendrites growth, "twig-shapes" appear on the protrusion (Fig 10C), which are transformed into "lycoperidium twigs-shapes" or "fern leaves-shapes" (Fig. 10D). Their further growth leads to huge crystallite (Fig. 10E). The higher magnification of this crystallite shows tiny silver crystals deposited on the previously formed silver fern leaf (Fig. 10F).

The growing dendrite (Fig.10C) behaves as a cathodic site and promotes a creation of an anodic site in a close neighbourhood.

Finally, the anodic site surrounds a dendrite island and develops in the copper material. Such an anodic site is visible on Fig. 10D as a crack encircling the protrusion.

The close examination of the anodic site is presented in Fig.11. Deposited tiny silver crystals are visible on the edges of the valley. Inside the deep valley much bigger Cu

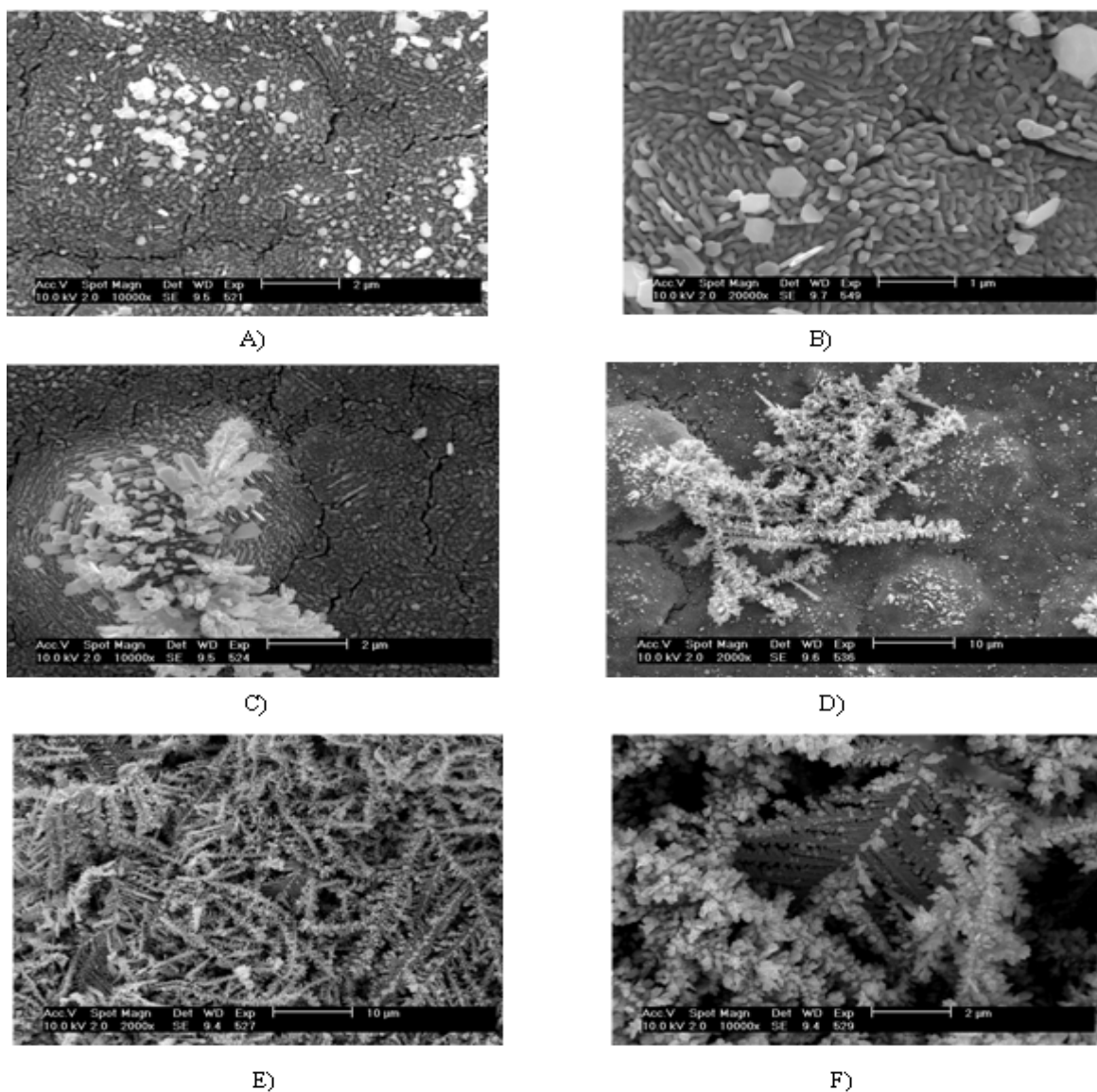


Fig. 10 Growth of the cathodic site in the cementation process conducted in the deoxygenated 0.5 M H_2SO_4 containing 20 mg/L Ag^+ at 25 $^\circ\text{C}$.

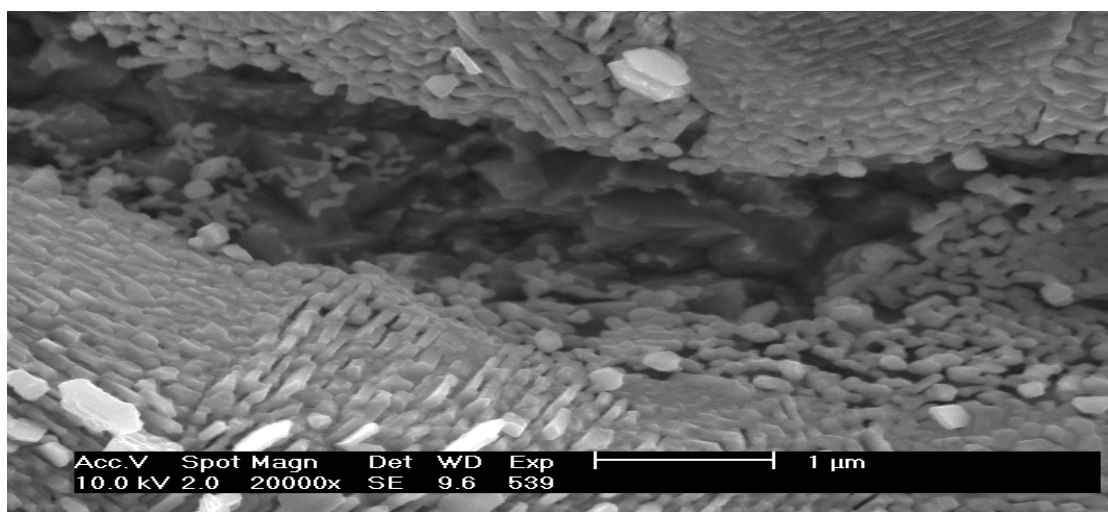


Fig. 11 The anodic site formed in the cementation process (deoxygenated 0.5 M H_2SO_4 , 20 mg/L Ag^+ , 25 $^\circ\text{C}$)

crystals appear. Results showed that anodic sites develop their working surface area in the copper material just under the deposited silver, with a formation of big cavities. The depth of these cavities was estimated to be about 3 μm .

6. Conclusions

1. The morphology of silver cements practically does not depend on oxygen content in solution.
2. The concentration of copper sulfate in the electrolyte has a great impact on the morphology:
 - a) In the solutions containing pure sulfuric acid or acid with small amount of copper (II) ions some parts of the surface are covered with smooth deposit, but other exhibit also huge dendrites.
 - b) The increase in concentration of copper sulfate up to 0.5 M results in a total disappearance of dendrites from the surface. Only tight deposit layer with tiny Ag crystals is observed.
3. The percentage of cemented silver found on the surface after the reaction in oxygen saturated solution remains practically constant whereas in oxygen free solution depends mainly on copper (II) ion concentration. It is caused by parallel side reaction, which produces colloidal silver in the bulk of solution.
4. The observed morphology of the deposits is consistent very well with the results obtained from kinetic.

measurements and confirms the proposed two-stage mechanism of cementation reaction.

References:

- [1] M.E. Wadsworth, *Trans. Met. Soc. AIME*, 254 (1969) 1381-1394.
- [2] M. Jaskula, *Acta Metal. Slov.*, 1 (1995), 3, 184-195.
- [3] G.D. Sulka and M. Jaskula, *Hydrometallurgy* 64 (2002), 13-33.
- [4] G.D. Sulka and M. Jaskula, *Hydrometallurgy* 70 (2003), 185-196.
- [5] G.D. Sulka and M. Jaskula, *Hydrometallurgy* 72 (2004), 93-110.
- [6] G.D. Sulka and M. Jaskula, *Hydrometallurgy* 77 (2005), 131-137.
- [7] G.D. Sulka and M. Jaskula, *Electrochim. Acta* 51 (2006) 6111-6119.
- [8] G.D. Sulka and M. Jaskula, *Helv. Chim. Acta*, 89 (2006) 2764-2773.
- [9] G.D. Sulka and M. Jaskula, *Helv. Chim. Acta*, 89 (2006) 902-914.
- [10] J. Pang and I.M. Ritchie, *Electrochim. Acta* 26 (1981) 1345-1350.

Determination of crystallite thickness and crystal growth mechanisms of Jordanian clays by X-ray diffraction method.

I.M.Odeh ^a, W.A.Saqqa ^b, D.Eberl ^c

^aDepartment of Physics, Yarmouk University, Irbid, Jordan,

^bDepartment of Earth & Environmental Sciences, Yarmouk University, Irbid, Jordan

^cU.S. Geological Survey, 3215 Marine St., Boulder, CO 80303-1066 USA

Abstract

Five mudrock samples were collected at different stratigraphical positions within the rock column of Jordan. They represent the ages of the late Ordovician-lower Silurian (SIL sample), late Permian (UI sample), Lower Cretaceous (MAH sample), Lower Turonian (TAF sample) and Pleistocene (YAM sample). The results of X-ray diffraction (XRD) analysis of clay fraction (particle size < 2 μm) show that the amount of smectite decreases towards more ancient mudrock samples, i.e. towards an increase of burial depth. Smectite totally disappeared in the Silurian claystone (SIL sample) at a depth of 1.6 km more likely as a function of burial diagenesis. The change of smectite into illite, due to burial history, was through a mixed layer illite-smectite intermediate stage of alteration. The shape of crystallite thickness distributions (CTDs) for illite was asymptotic in all study samples. This means that the crystal growth mechanism of illite particles was similar regardless of the burial depth of sediments and was concurrent with nucleation. The XRD patterns showed that the degree of Kaolinite crystallinity increased generally with depth as the 001 reflection becomes sharper and narrower. The CTDs shapes for kaolinite were somewhat different. It was asymptotic in YAM and TAF samples, multimodal in MAH sample, and lognormal in UI and SIL samples. These variations in CTDs distributions reflect the fact that crystal growth mechanism of kaolinite differed with burial depth. Kaolinite crystal growth accompanied with nucleation was only at shallow-moderate depths. This changed to crystal growth without continued nucleation at greater depths.

© 2009 Jordan Journal of Earth and Environmental Sciences. All rights reserved

Keywords :X-ray diffraction, Jordanian clays, MudMaster Program, crystallite thickness distribution, asymptotic shape, lognormal shape.

1. Introduction

The use of X-ray diffraction (XRD) to study the crystallinity of clay minerals, crystallites sizes and the shapes of crystallite thickness distributions (CTDs) have attracted considerable attention over the past years. Dudek et al. (2002) pointed to several mathematical approaches in order to obtain information about crystal size from the XRD peak shapes. Of these approaches is Scherrer equation (Drits et al., 1997), variance method (Wilson, 1963 in Arkai et al., 1996), Bertaut-Warren-Averbach (BWA) method (Eberl et al., 1996; Drits et al., 1998). While Scherrer's equation yields the mean crystallite thickness, variance and Voigt methods give information regarding the mean size and strain (Dudek et al., 2002). The BWA-method however, is most universal because it is capable of measuring the crystallite mean size, strain and crystallites size distributions. The latter method forms the basis of a computer program known as MudMaster, which was produced by Eberl et al. (1996) and later developed by Drits et al., (1998). MudMaster is capable of determining

the particle size, crystallites size distributions and strain for different types of clay minerals such as Illite, kaolinite, smectite, and some other clay minerals. Determination of crystallites thicknesses of illite by either XRD or TEM (Eberl and Velde, 1989; Merriman et al., 1990; Nieto and Sánchez-Navaz, 1994; Lanson et al., 1996; Arkai et al., 1996; Eberl et al., 1996; 1998a, b; Drits et al., 1998; Jaboyedoff et al., 2001; Brime and Eberl, 2002) is as an alternative approach for methods based on measuring illite crystallinity by determining the Kübler index. The evolution of illite in mudrock during burial diagenesis was better explained by applying the BWA-method (Brime and Eberl, 2002). According to the later authors and earlier to (Eberl et al., 1996) the resulting crystallite thickness distributions (CTDs) exhibit asymptotic, lognormal and multimodal shapes. These CTD's can suggest information about nucleation, crystal growth mechanism, and history based on the theoretical approach of Eberl et al. (1998a). The resulting shapes can be used to establish a model for crystal growth of clay minerals.

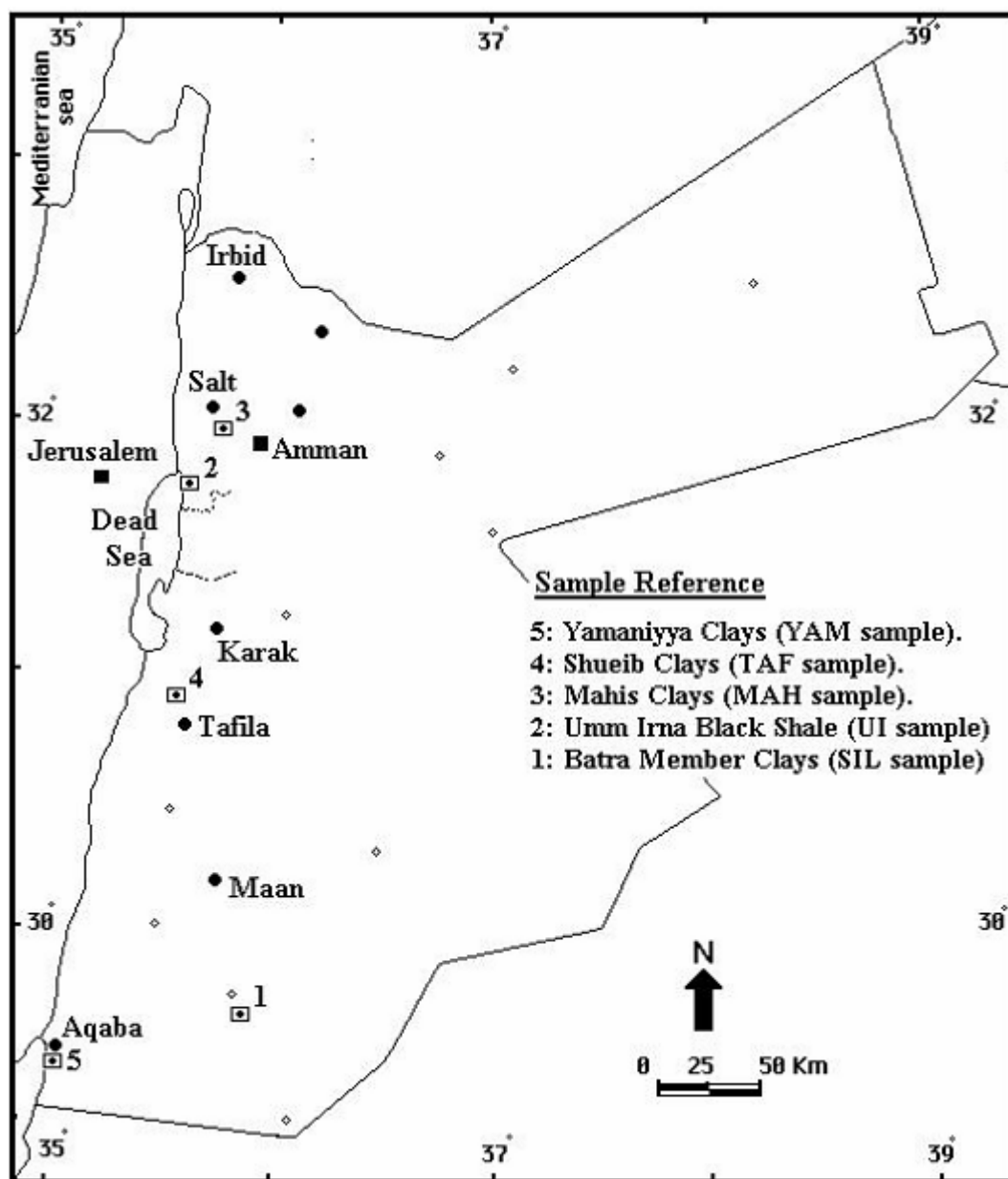
The present study employed the X-ray diffraction and the MudMaster software for measuring the mean crystallite thickness, crystallite thickness distributions (CTDs) of illite and kaolinite in some selected Paleozoic-Pleistocene Jordanian mudrock samples. These measurements aim to determine changes in crystallite size,

* Corresponding author. iodeh@yu.edu.jo

the mean crystallite thickness and the CTDs shapes of illite (I) and kaolinite (K) and to detect their crystal growth mechanisms from measurements of the 001 basal reflections

2. Materials

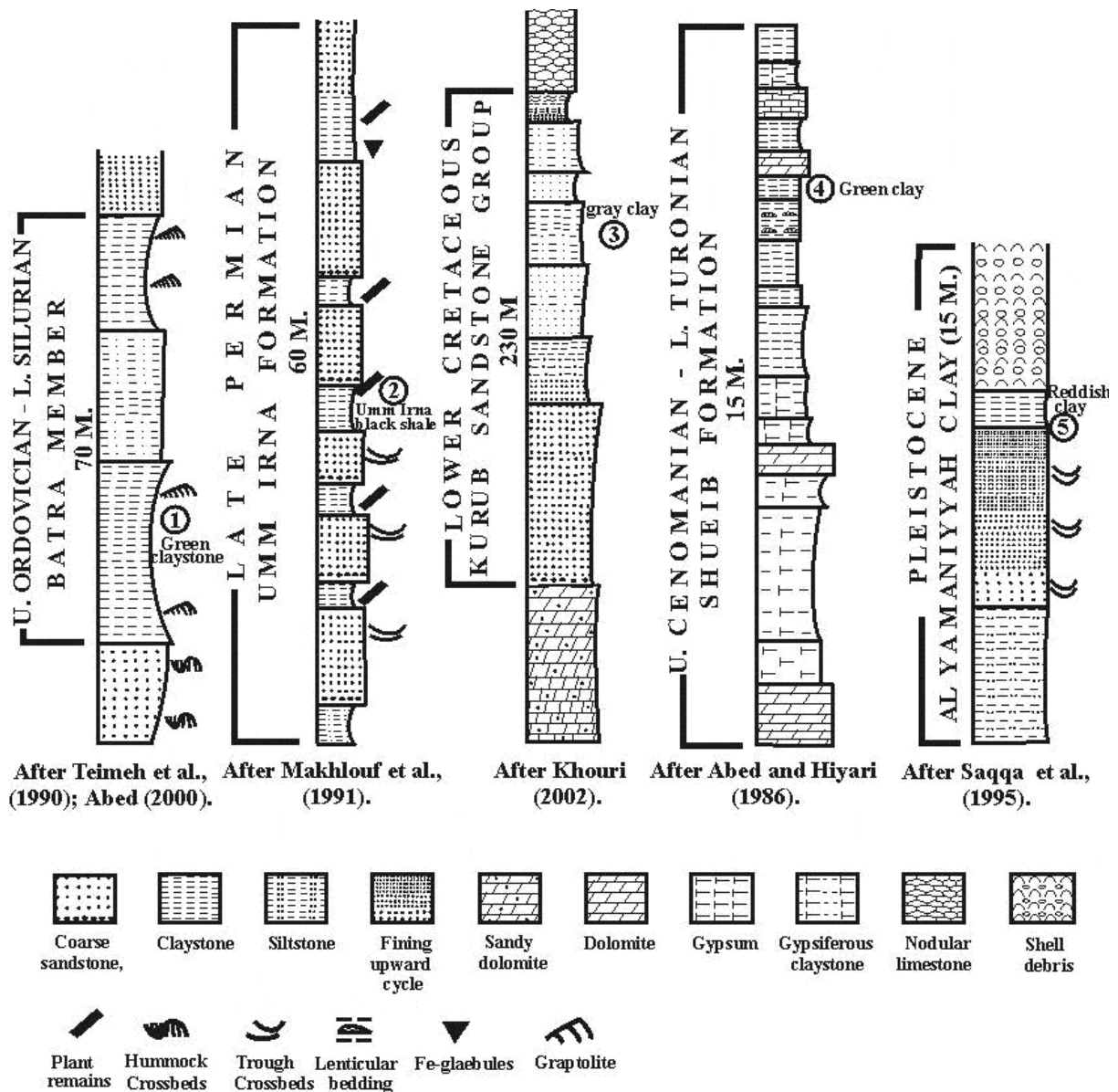
Five mudrock samples were selected for this study (Fig. 1).



Fig(1). Locations of study samples.

The first and most ancient sample (Sample Ref., SIL) refers to the late Ordovician-early Silurian Batra Member grayish-green kaolinitic clay stone with an abundance of Graptolite remains found at bedding planes. Clay stones are interbedded with reddish siltstone-fine sandstone beds (Fig. 2). Batra Member is about 80 m thick and of marine origin (Abed, 2000). The second sample (Sample Ref., UIR) was selected from the black shale horizons with plant remains in the upper parts of the late Permian Umm Irna Formation cropping out close to the northeastern Dead Sea shorelines. The formation consists principally of two quartz arenite sandstone facies (60 m. thick) with fining upward cycles. Each starts with pebbly sandstone at the

base and changes upward into fine sandstone, siltstone and silty clay stone (Fig.2). The uppermost two cycles are distinguished by the presence of reddish-brown and occasionally dark gray paleosol horizons separated from each other by the dark gray-black shale beds (Makhlouf et al., 1991) from which UIR sample was collected. The third sample (Sample Ref., MAH) was selected from the light gray-green kaolinitic clay deposits interbedding a thick sandstone sequence (\approx 200m) of the Lower Cretaceous Kurnub Group, which crops out in Mahis area (Fig. 2). The fourth sample (Sample Ref., TAF) was selected from the Turonian Shueib Formation. This formation crops out in the area between Karak and Tafila, south of Jordan. The



After Teimeh et al., (1990); Abed (2000). After Makhlouf et al., (1991). After Khouri (2002). After Abed and Hiyari (1986). After Saqqa et al., (1995).

Fig.2. Generalized columnar sections from which mudrock samples were selected. (Reference samples denoted in text as :SIL (sample 1), UI(sample 2), MAH (sample 3), TAF(sample 5)).

formation consists principally of dolomitized carbonate rocks and marl interbedded with gypsum layers of different textures with green and red-colored gypsiferous clay stone (Fig. 2). The fifth and the youngest sample (sample Ref., YAM) was selected from the upper red-brownish clay stone horizons of the Pleistocene Al-Yamaniyya clay deposits cropping out 6 km east of the Gulf of Aqaba, not far from Saudi borders with Jordan in the south. The varicolored claystone deposits interbedding sandstone of various sizes from coarse to fine (Fig.2) indicating a near shore environment (Ibrahim and Abdelhamid, 1990; Abu Halima, 1993; Saqqa et al., 1995).

3. Experimental

Mud rock samples were gently crushed, using an agate mortar and pestle. Samples were then treated only with

12% H₂O₂ to remove organic matter. Samples were wet sieved using a test sieve of 45µm to discard coarser fractions. The clay fraction (< 2 µm) was obtained from the pass 45 µ fraction by sedimentation, centrifuging and dialysis. The clay fraction (< 2 µm) was sedimented on a polished silicon-wafer substrate and left to dry at room temperature. After mounting, air-dried samples were heated at two different temperatures 350°C, 550°C. The samples were then ethylene glycolated at 60°C for 16 hours. PVP-10 (Polyvinylpyrrolidone) intercalated air-dried clays (< 2 µm fraction) were prepared, mounted on silicon-wafer substrates and analyzed by XRD for the purpose of measuring the fundamental illite particle thicknesses and their distributions (Eberl et al., 1998a).

In study samples, ratios of PVP to clay intercalations were as follows:

Sample	Ratio PVP : CLAY
YAM	4:1
TAF	3:1
MAH	2:1
UI	2:1
SIL	2:1

Clay fraction was suspended in distilled water (concentration 2.5mg clay/1ml H₂O), then mixed with an aqueous solution containing 5mg PVP/1ml H₂O fully dispersed by ultrasonic treatment. The proportion of clay to PVP used depended on the expandability of clay sample. The larger the proportion of smectite layers, the more PVP is added to obtain good intercalation. Samples presumed to have < 50% smectite content were mixed in proportions of 5 mg PVP to 2.5 mg clay (1 ml PVP solution/1 ml clay suspension), whereas the amount of PVP added for clays containing > 50% smectite was chosen by interpolation between former proportion, and that used for pure smectite (10 mg PVP to 2.5 mg clay or 2 ml PVP solution/1ml clay suspension). The mixtures were shaken by hand, left for a few minutes, sonified and then mounted appropriately for XRD scan (Dudek et al., 2002). The treatment with PVP-10 was applied for measuring sizes of illite particles. For kaolinite, such treatment was not required. The advantage of the PVP-10 intercalation is to remove the effect of peak broadening related to swelling interface of the exposed basal surfaces (containing H₂O and exchangeable cations) of illite. In this way crystallite thicknesses could be calculated accurately by the BWA method. In the meantime the use of silicon wafers as substrates improved significantly the background of the XRD spectra (Eberl et al., 1998a; Drits et al., 1998; Bove et al., 2002). The 001 reflection of PVP-illite and kaolinite was measured by the BWA-method, using the MudMaster computer program (Eberl et al., 1996). The mean crystallite thickness, CTDs, the mean of natural logarithms of thicknesses α , and the variance of natural logarithms of thicknesses β^2 were all determined by applying the foregoing method. The measured CTDs were compared to theoretically calculated shapes of CTDs, using the GALOPER computer program (Eberl et al., 2000). The size of critical nucleus was set to 2nm when the modeling results were compared to BWA-PVP data in case of illite or to BWA data only in case of kaolinite. X-ray analysis was carried out using a Phillips PW1710 Diffractometer equipped with copper tube and a theta compensatory slit assembly. The system was operated under the following experimental conditions: a voltage of 35 kV, beam current of 40 mA, 2θ step size of 0.02°, counting time of 0.01 sec/step, 1 mm receiving slit and a scanning range of 2-65° 2θ . The BWA method adapted in the MudMaster computer program is based on Fourier analysis of the interference function (Eberl et al., 1996; Drits et al., 1998). The peak shape analysis for the purpose of measuring the mean crystallite thickness and the CTDs was for the 001 basal reflection of illite (I) and kaolinite (K).

4. RESULTS

a. XRD Analysis

The XRD patterns (Fig. 3; Table 1) show that illite (I) and kaolinite (K) are the main clay minerals in the Upper Ordovician–Lower Silurian Batra Member clay- stone (SIL sample). In the Late Permian Umm Irna black shale (UI sample) and in the Lower Cretaceous Mahis claystone (MAH sample) asymmetric broad mixed-layer illite-smectite (I-S) peaks of low intensity appear at 7.7° 2θ and 7.2° 2θ together with I and K. The mixed layer I-S peaks collapsed to 8.8° 2θ by heating at 550 °C. In the Lower Turonian Tafila green claystone (TAF sample), a broad peak of I/I-S appears around 8.02° 2θ in the air-dried X-ray pattern (Fig.3; Table 1). After ethylene glycolation, this peak was completely separated into two other peaks: one at 5.4° 2θ referring to Mg-smectite (S) and the second at 8.8° 2θ for illite. Środoń (1980) and Weibel (1999) considered the type of mixed layer I-S which completely separated into two peaks after ethylene glycol saturation as a random one. By heating at 550°C, smectite (S) in the mixed layer collapsed to the position of illite at 8.8° 2θ . Kaolinite (K) was also present in the Tafila claystone.

Mg-smectite (S) dominates other clay minerals in the Pleistocene Al-Yamaniyyah claystone (YAM sample). To a lesser extent is kaolinite (K), illite (I), mixed layer I-S, chlorite (Ch) and mixed layer illite-chlorite (I-Ch). The original 001 peak of smectite (S) at 6.2° 2θ in air-dried sample expanded to 5° 2θ after ethylene glycol saturation (see Fig.3; Table 1). The same peak collapsed upon heating at 550 °C to 9.04° 2θ (9.8X). The display of chlorite (Ch) and mixed layer illite-chlorite were verified after heating at 550 °C as shown in figure 3.

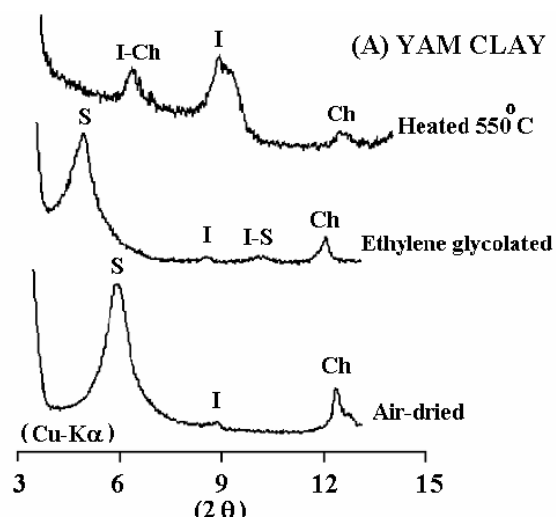


Fig.3 continues next page.....

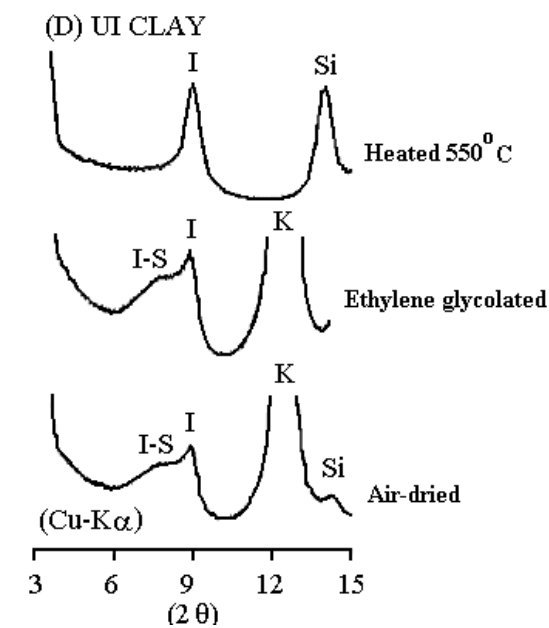
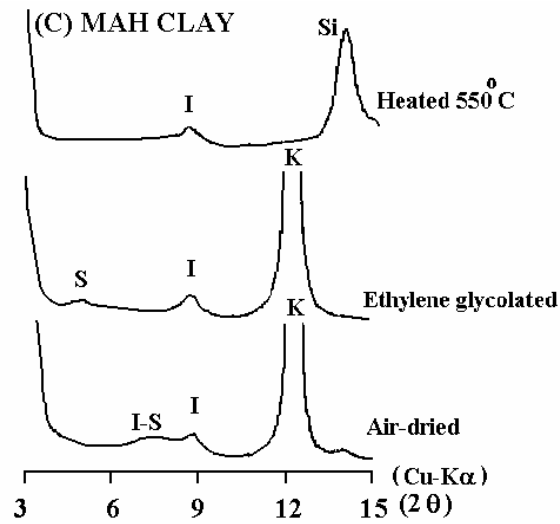
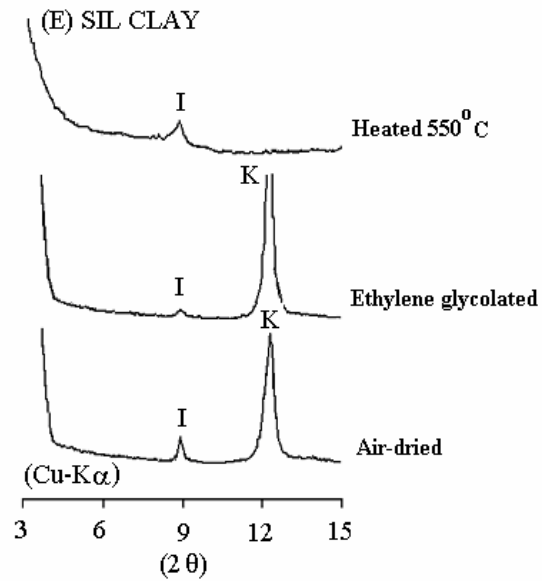
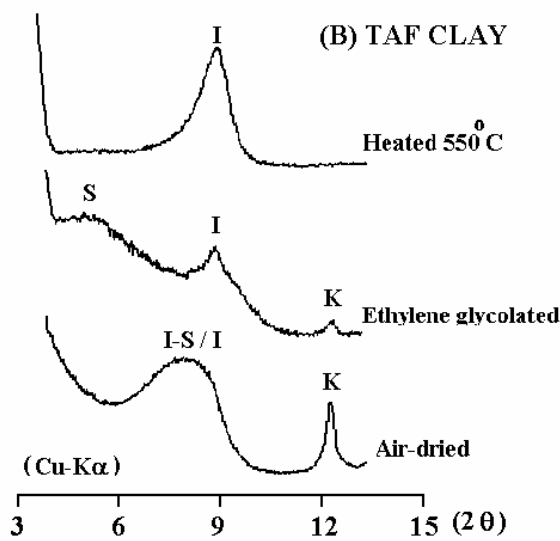


Fig. 3: X-ray diffractograms (air-dried, ethylene glycolated, heated at 550°C) of study samples.

S=Smectite, I-S= mixed layer illite-smectite, I=illite, K=Kaolinite, Ch=Chlorite, I-Ch= mixed layer illite-chlorite, Si=Silicon wafer.

b. Changes in particle size of illite and kaolinite with burial depths:

Table (2) summarizes results of mean particle thickness (T_{mean}), α , β , CTDs shapes of illite (I) and kaolinite (K) with corresponding burial depths and temperatures. For illite (I) the mean particle thickness (T_{mean}) ranges from 2.8 nm - 3.3 nm. Although mean particle thickness (T_{mean}) of illite (I) shows no significant variations with depth, the natural conditions under which the relevant illite (I) formed are quite different.

For Kaolinite (K), the mean particle thickness (T_{mean}) slightly varies from one sample to another. They range in size from 3 nm-10.7 nm. At the beginning, slight increase in the mean particle thickness (T_{mean}) of kaolinite particles from 3 nm-3.7 nm resulted through a change in burial depth from a shallow depth to about 0.95 km. This is followed by a sharp increase from 3.7 nm-9.0 nm only within a small increase in burial depth of about 150 m. Again, a progressive increase in the mean crystallite thickness, 9.0 nm – 10.7 nm, was observed within a burial depth from 1.05 km-1.22 km. Beyond this depth, the mean particle thickness (T_{mean}) flipped toward a slight decrease with mean crystallite thickness difference of 0.7 nm as the burial depth approaches 1.6 km.

c. Crystallite thickness distributions (CTDs) for illite (I) and kaolinite (K):

The CTDs for PVP-illite (air dried samples) and kaolinite (heated at 350°C samples) were calculated as area-weighted in the BWA technique (Eberl, 1998b). Figure (4) illustrates the shapes of crystallite thickness distributions (CTDs) for illite (I). The CTDs of illite (I) in study samples are similar with asymptotic shapes indicating higher influence of simultaneous nucleation and growth except MAH sample which looks lognormal. Illite's T_{mean} is between 3.8 nm-5.2 nm). Figure (5) illustrates the CTDs shapes for kaolinite (K). They look

Table (1). Summary for XRD data between 3°-15 ° 2θ of all studied samples.

Name of Sample	Air-dried (2θ) $d(\text{Å})$		Ethylene-glycolated (2θ) $d(\text{Å})$		Heated (550°C) (2θ) $d(\text{Å})$	Clay mineral
YAM	6.2 14.25	shifted to	5.0 17.67	collapsed to →	9.04 9.8	smectite
	n.d. n.d.	→	n.d. n.d.	→	6.54 13.5	illite-chlorite (Illite 30-40%).
	8.88 10	slightly increased to	8.68 10.10	slightly shifted to	9.04 9.8	illite
	n.d. n.d.	→	10.3 8.6	shifted to	9.04 9.8	illite-smectite (Illite 10%)
	12.42 7.13	→	12.2 7.25	→	12.62 7.02	chlorite
	12.48 7.09	→	12.34 7.17	→	destroyed	kaolinite
TAF	8.02 11.02	separated to two peaks:	1) 5.2 17.0 2) 8.8 10.0	1) collapsed to 2) unchanged	8.8 10.0 8.8 10.0	illite-smectite smectite illite
	12.32 7.18	unchanged	12.32 7.18	→	destroyed	kaolinite
	6.92 12.7	separated to two peaks:	1) 5.4 16.3 2) 7.2 12.3	1) collapsed to 2) →	8.8 10.0 →	illite-smectite smectite illite-smectite
MAH	8.8 10.0	slightly shifted to	9.04 9.78	unchanged	8.8 10	illite
	12.38 7.15	unchanged	12.38 7.15	→	destroyed	kaolinite
	7.7 11.5	unchanged	7.7 11.5	collapsed to	8.8 10	illite-smectite (illite 80%)
UI	8.94 9.89	unchanged	8.94 9.89	unchanged	8.94 9.89	illite
	12.4 7.13	unchanged	12.4 7.13	→	destroyed	kaolinite
	8.92 9.91	v. little change	9.02 9.8	unchanged	8.92 9.91	illite
SIL	12.44 7.12	unchanged	12.48 7.2	→	destroyed	kaolinite

asymptotic for both YAM and TAF samples, multimodal for MAH sample and lognormal for both UI and SIL samples. The distribution shapes indicate changes in crystal growth mechanisms from constant rate nucleation accompanied with growth (shallow-moderate depths) to a state of growth without continued nucleation at greater depths.

d. α versus β^2 diagram

Illite CTDs were characterized further by simulating illite (I) crystal growth using the GALOPER computer program (Eberl et al., 2000). For this purpose the parameter α , the mean of the natural logarithms of thicknesses, was plotted versus the parameter β^2 , the variance of the natural logarithms of thicknesses, together

with theoretical paths of two crystal growth mechanisms. The first is the simultaneous nucleation and surface-controlled growth, and the second is the surface-controlled growth without nucleation (Eberl et al., 1998a; Środoń et al., 2000; Bove et al., 2002). In the first mechanism, new illite (I) nuclei continue to form at a constant rate while previously nucleated crystals continue to grow. During the second mechanism, growth occurs on previously nucleated crystals without new nucleation (Eberl, 1998a). Figure (6) shows that all asymptotic shapes of illite (I) are plotted close to the path line "AB" which reflects the first mechanism, i.e. simultaneous "constant rate" nucleation and surface-controlled growth. This crystal growth mechanism proceeds with constant rate nucleation of 2 nm thick-layered illite (I) which subsequently experiences size

Table (2): Parameters of mean crystallite thickness T_{mean} (best mean), ∞ , β^2 , 2θ , d-spacing and CTDs shapes of PVP-illite and kaolinite as a function of burial depth and the corresponding temperature of all studied samples.

Sample	Burial depth (m)	Temperature (C°)	Best mean, T_{mean} (nm)	∞	β^2	2θ	d-spacing (Å)	CTDs shape
YAM	shallow	surface T.	2.8	0.93	0.16	8.78	10.07	Asymptotic.
TAF	950	45	3	1.01	0.17	9	9.83	Asymptotic
MAH	1050	50	2.9	0.96	0.17	8.74	10.12	Asymptotic
U I	1220	58	3	0.99	0.18	8.82	10.03	Asymptotic.
SIL	1600	70	3.3	1.04	0.23	8.76	10.09	Asymptotic

B. Kaolinite (Heated at 350° samples)

Sample	Burial depth (m)	Temperature (C°)	Best mean T_{mean} (nm)	∞	β^2	2θ	d-spacing (Å)	CTDs shape
YAM	shallow	surface T.	3	0.8	0.44	12.42	7.13	Asymptotic
TAF	950	45	3.7	0.81	0.75	12.34	7.17	Asymptotic
MAH	1050	50	8.9	2.07	0.66	12.34	7.17	Multimodal
U I	1220	58	10.7	2.25	0.29	12.42	7.13	Lognormal
SIL	1600	70	10	2.2	0.36	12.36	7.16	Lognormal

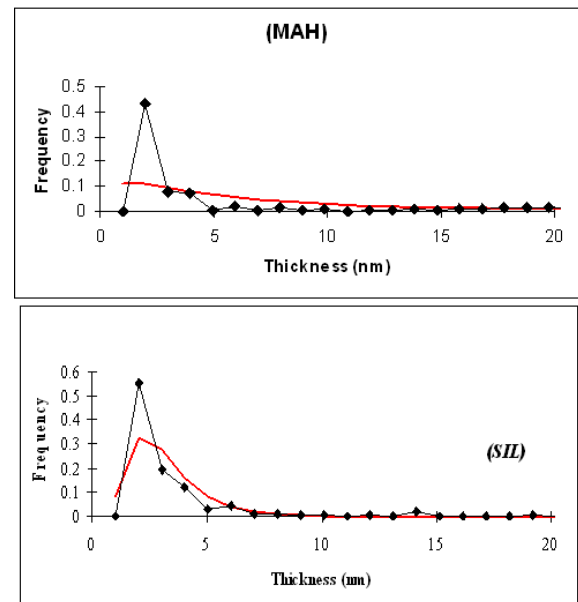
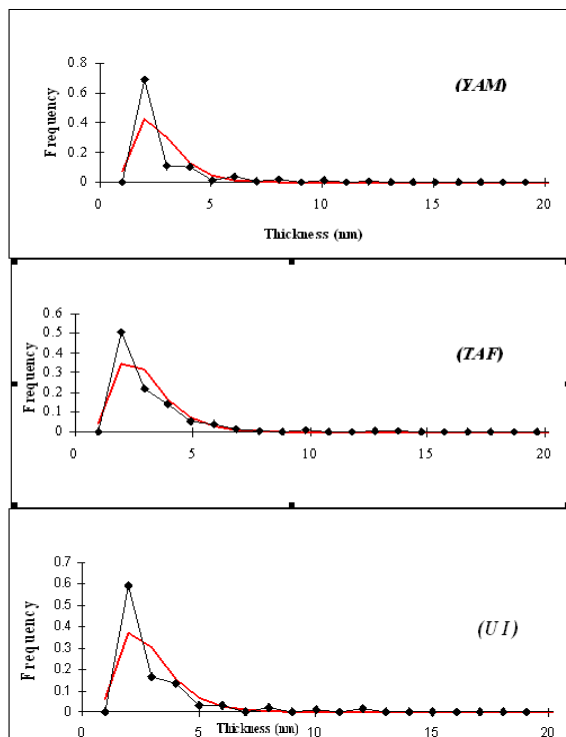


Fig. 4: Shapes of Illite particle thickness distributions in study samples using the BWA-PVP technique.

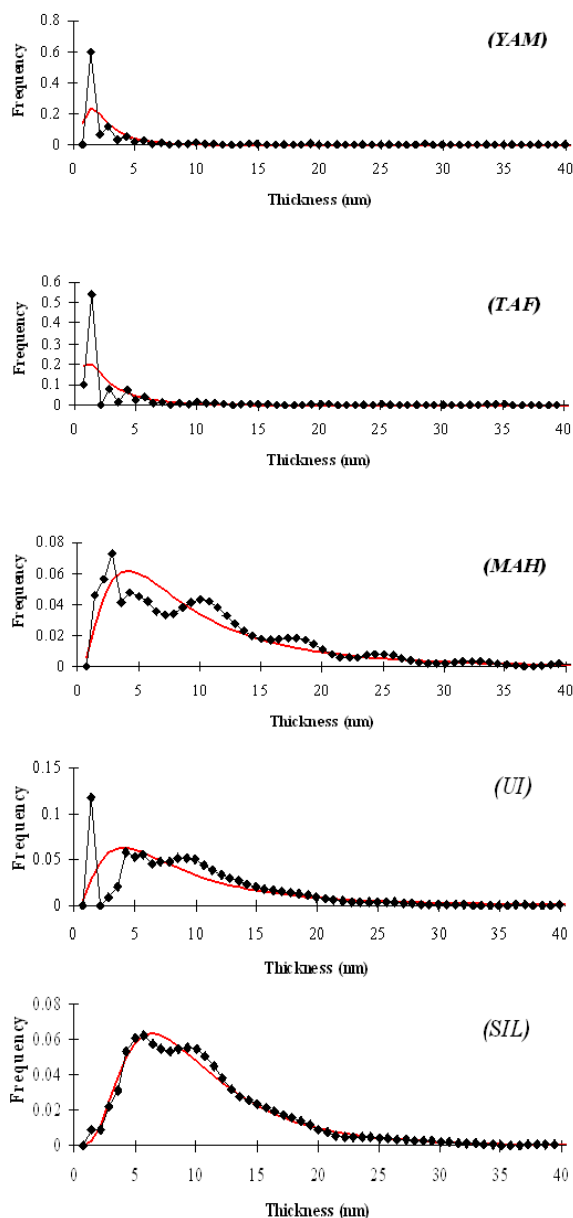


Fig. 5. Shapes of kaolinite particle thickness distributions in study samples using BWA-PVP technique.

dependent growth by the Law of Proportionate Effect "LPE" (Eberl et al., 1998a; Środoń et al., 2000; Bove et al., 2002). The asymptotic shapes of illite (I) to the left of the path line "1" could indicate that the final nucleation was not accompanied by growth.

5. Discussion

Results of raw X-ray data emphasize the fact that diagenetic changes in clay mineral types must take place through geological time. Smectite (S), which predominates other clay minerals in the Pleistocene Al-Yamaniyya surface clay deposits, is no longer abundant in the Turonian Shueib clays, Tafila area (TAF sample) and in the Lower Cretaceous Mahis clays (MAH sample), where the depth of burial approaches 1 km. Smectite (S) began to change into mixed layer I-S. Illite (I) and I-S are chief constituents in Tafila clays with subordinate kaolinite (K) and minor smectite (S). In the Lower Cretaceous

Mahis clays kaolinite (K) predominates other clay minerals and illite (I) is less dominant. Progressive illitization was more likely enhanced after a burial depth of 1 km. Significant peaks of illite (I) and kaolinite (K) are typical in the late Permian black shale of Umm Irna Formation (UI sample) where the burial depth approximates 1200 m and in the Upper Ordovician-Lower Silurian green claystone of Batra Member of a burial depth 1600 m. Based on the obtained results, the distinct appearance of illite (I) peaks in the moderately to deeply buried Paleozoic clays indicates that this mineral was formed from diagenetic alterations of smectite (S) and S-I precursors. The degradation of smectite (S) and its transformation to illite (I) involve the incorporation of potassium (K⁺) ions into smectite structure and loss of interlayer water (Dunoyer de Segonzac, 1970; Hower et al., 1976). Compaction of mud through overburden pressure soon removes much of the water contained in lattices of clay mineral and water adsorbed onto clay surface or the less common pore filled water. At depths greater than one kilometer (temperature ≥ 45 °C), 70-90% of the original volume of water is reduced to about 30%. Further compaction through water loss requires temperature of about 100 °C. These are attained at greater depths (2-4 km). Dehydration of clays then takes place causing some changes in clay minerals types. Final compaction, leading to mudrock with only small percent water needs much longer period of overburden pressure with elevated temperature (Tucker, 1981, 1991). Amireh et al., (1994) studied the diagenesis in Paleozoic-Cretaceous sandstones in Jordan, pointed to the degradation of detrital muscovite into kaolinite and postdating of newly formed kaolinite to quartz overgrowth. They also observed the formation of dickite after kaolinite in the pore spaces of the Cambrian-early Ordovician sandstone (burial depth >2 km). Despite the significance of temperature and burial history as controlling parameters to diagenesis, we can't ignore the role of other controlling parameters such as tectonic uplift and sediment unroofing, which undoubtedly trigger sub aerial weathering for the unroofed sediments through geological time. Another criterion which may complicate the origin of clay minerals is the possible occurrence of the same types of clay minerals in more than one particular environment (terrestrial-marine) with different physical and chemical conditions. Therefore, in this work we attempted to give answers to questions raised about the origin of the investigated argillaceous rocks, giving the issue of primary origin of clay minerals great consideration.

The coexistence of kaolinite (K) and smectite (S) in the Pleistocene Al-Yamaniyya clays can only be explained on the basis of their primary origin after chemical weathering of the source materials. These two minerals very likely originated from a relatively high weathering of the very near Precambrian granitic source rocks intruded by mafic dikes. Weathering products were transported by streams draining granitic terrains and later deposited in a lacustrine environment separated from sea by some beach terraces (Abu Halimeh, 1993; Saqqa et al., 1995; Khouri, 2002). Leaching of iron and magnesium from weathering products leaves behind concentrations of silicon and aluminum to yield kaolinite crystals.

In the Lower Turonian Tafila clays, dolomite and gypsum interbed green and red claystone beds. The whole sediments were deposited in a coastal sabkha after tectonic uplift at the beginning of the Turonian age. The tectonic event caused sea level fall resulting in the development of the sabkha environment (Abed and El Hiyari, 1986). Tafila claystone were more likely deposited during periodic influxes of fresh water (e.g. Droste, 1963) at the time of sedimentation. After deposition, detritus clays were subjected to diagenetic changes, and new clay phases resulted through which smectite (S) altered to I-S and illite (I) under conditions of a saline lake or the sabkha. In most lake brines calcite or aragonite and/or gypsum precipitate early where Mg/Ca ratio is relatively low. The increase in Mg/Ca ratio causes Mg-rich minerals to precipitate such as dolomite, sepiolite and Mg-smectite (Weaver, 1989). Honty et al., (2004) noted that illitization of salt-bearing bentonite was enhanced by the aid of salinity and burial temperature. These authors referred to some studies that focused on the formation of I-S from smectite at surface conditions in sediments of saline lakes. Similarly, in their study, Turner and Fishman (1991) discussed illitization of smectite in altered tuff beds in a Jurassic lake with the absence of the effect of deep burial and lack of hydrothermal alteration. They concluded that solution chemistry was the principal factor controlling illitization of smectite at the surface temperatures. Eberl et al., (1986) realized that illitization of smectite is possible through wet-dry cycles. This is common in saline environments. In the presence of K⁺ ions, wet-dry cycles lead to irreversible fixation of K⁺ ions and formation of illite. Similarly, Stoffers and Singer (1979) described genesis of physils in Lake Albert sediments which reflected the evaporation history of its water. These authors believed that detrital smectite in bottom sediments were produced when the lake was open and the concentration of dissolved ions was low. I-S formed when the lake became closed and its water level was at its lowest. Ionic concentration increased and K⁺ content became high enough to start the process of illitization. With regard to the genesis of the green clays (TAF sample), we may suggest here that these clays were originally developed from the reduction of hematite in red clays by leaching of wet cycles at surface conditions. This idea can be supported by the absence of chlorite from the green clays (not detected in the X-ray data), which can impart green color for clays in nature. In addition to the above discussion about the genesis of green clays, we also believe that these clays were subjected to early diagenetic illitization as a result of surface wet-dry cycles, evaporation, and fixation of K⁺ ions. Absence of halite beds from the rock sequence of the Lower Turonian Shueib Formation (Tafila area) support the lack of NaCl concentrations from the depositional medium. This significantly enhances K⁺ ions fixation in clays (Honty et al., 2004). A burial depth of about one kilometer may help the transformation of smectite to mixed layer I-S.

Mahis clays (MAH sample) which are a part of fluvial system sediments (Abed, 1982; Khoury, 2002) have two origins, detrital (primary) and diagenetic. Some kaolinite produced from degradation of detrital feldspar and mica and some other kaolinite are authigenic. Khouri (2002) reported the presence of small authigenic kaolinite flakes adhered to quartz surfaces as a result of diagenesis after

sedimentation. Intensive leaching of the detritus in acidic medium helps kaolinization process aided by rainfall and surface running water. Field observations confirmed the presence of carbonized plant remains in the gray clays of Mahis. The breakdown of plant remains and release of CO₂ due to compaction caused the creation of acidic medium in the pore water. This initiated the neoformation of kaolinite (K) at depths surpass 1km (T>50 °C). The minor content of I-S and the initial presence of illite (I) suggest that more advanced stages of illitization were enhanced at the same depths.

Coalified plant remains were found also in the Late Permian Umm Irna black shale (UI sample). This again promoted the creation of acidic medium in the pore water as a result of organic matter decay and CO₂ release possibly by thermal maturation at greater depths (> 1200 m). Accordingly, crystal growth of primary kaolinite (K) flakes took place. The strong appearance of illite and kaolinite peaks as viewed from the XRD analysis supports a continued smectite illitization and the increase of kaolinite crystallinity with burial depth.

The marine green clays (SIL sample) of the Upper Ordovician-Lower Silurian Batra Member are intercalated with fine sandstone and siltstone materials with an abundance of Graptolite remains at the bedding planes of green clays. After sedimentation, the compaction of sediments by the overlying rocks (burial depth >1.6 km) caused a set of physical and chemical changes to these sediments. Thus, illitization process proceeded and the crystallinity of kaolinite (K) was increased. This was despite the detrital origin of these clays which were derived from the older highly weathered underlying rocks.

MudMaster analyses showed that the distribution curves (CTDs shapes) of PVP-illite samples were all asymptotic attained at burial depths from a shallow depth to about 1.6 km. These results would explain the diagenetic origin of illite after a detrital source. As discussed earlier, the mechanism of illite crystal growth is expressed as a simultaneous nucleation together with growth where new illite nuclei continue to form at a constant rate while previously nucleated crystals continue to grow. An indication to illite crystals growth can be deduced from the T_{mean} increase obtained when the burial depth exceeded 1.05 km. Eberl (2004) found that the asymptotic shape of illite (I) can be related to sedimentation origin. It can also be obtained for illite (I) from analyzed shale samples and in a hydro thermally-altered wall rock. In the present work, there was no evidence for hydrothermal activities. Hence diagenesis postdating sedimentation process is most likely to be the reason for the asymptotic distribution form and the simultaneous nucleation and growth of illite crystals. This is regardless of the changes in temperature, pressure and time progress within the zone of diagenesis prior to arriving low grade metamorphism. However, the asymptotic CTDs shape also could be due to detrital illite. On the other hand, kaolinite CTDs shapes were asymptotic in the investigated younger sediments at burial depths of less than 1km. This is followed by multimodal distribution at slightly deeper burial depth of 1.05 km. At relatively greater depths of 1.6 km, the distribution changed into lognormal form. The change in distribution forms might be interpreted on the basis of sedimentation and early

diagenesis of kaolinite (K) taking place at a burial depth of 1 kilometer and allowing for simultaneous crystals nucleation and growth. After this depth, kaolinite growth mechanism changed through an intermediate stage of a multimodal thickness distribution shape to lognormal shape at greater depths (>1.6 km) where nucleation ceased and growth only continued. This explanation of the change in CTDs shapes of kaolinite (K) from asymptotic to lognormal could be supported by the fact that the 001 kaolinite peaks are of high intensity, narrow and more symmetric reflecting well-ordered crystals in older deep buried sediments in comparison with more recent sediments buried at moderate-shallow depths.

6. Summary and Conclusions

The present work revealed that diagenetic changes of the identified clay minerals took place at various depths. Smectite (S) decreased and finally transformed into illite (I) through an intermediate mixed-layer I-S after exceeding a burial depth of one kilometer. Transformation of clay mineral species from primary into authigenic was produced under different depositional settings (terrestrial-marine). For instance, illitization process in the Lower Turonian Tafila green clays was enhanced in a saline sabkha environment by the aid of wet-dry cycles and K-ions fixation at surface conditions. This was aided by a tectonic uplift and unroofing of the Lower Turonian carbonate sediments of Shueib Formation. Deep burial was a crucial factor for illite crystallization and the increase of kaolinite crystallinity. Results obtained from MudMaster calculations were consistent with the observed X-ray diffraction data regarding illitization of smectite (S) and mixed layer I-S after sedimentation process. Simultaneous nucleation and continuous growth of illite nuclei interpreted from the asymptotic shape in all samples clearly reflect the effect of illitization of smectite into illite during burial history. The changes in CTD's of kaolinite (K) from asymptotic to lognormal through a multimodal phase reflect the variations in kaolinite crystal growth mechanisms with burial depth.

Acknowledgments

The authors would like to thank Dr. F. Ababneh of the Physics Department, Yarmouk University for operating the X-ray Diffractometer. For the anonymous referees, we extend our appreciation for their comments and critique.

References

- [1] Abed, A. (1982). Depositional environments of the Early Cretaceous Kurnub (Hathira) Sandstones, North Jordan. *Sedimentary Geology*, **31**, 267-271.
- [2] Abed, A. and El-Hiyari, M. (1986). Depositional Environments and Paleogeography of the Cretaceous gypsum horizon in west-central Jordan. *Sedimentary Geology*, **47**, 109-123.
- [3] Abed, A. (2000). *Geology, Environment and water of Jordan (in Arabic)*. Published by Jordanian Geological Association, Scientific Books Series 1, Amman, 571pp.
- [4] Abu Halima, K. (1993). Mineralogy, chemistry and industrial studies of Al-Yamaniyya clay deposits in Aqaba area. M.Sc. thesis, University of Jordan, Amman.
- [5] Amireh, B.S., Schneider, W. and Abed, A.M. (1994). Diagenesis and burial history of the Cambrian-Cretaceous sandstone series in Jordan. *Neues Jahrbuch für Geologie und Paläontologie Abhandlungen* **192**, 151-181.
- [6] Árkai, P., Merriman, R.J., Roberts, B., Peacor, D.R. and Tóth, M. (1996). Crystallinity, crystallite size and lattice strain of illite-muscovite and chlorite: comparison of XRD and TEM data for diagenetic to epizonal pelites. *European Journal of Mineralogy* **8**, 1119-1138.
- [7] Langford, 1978
- [8] Bove, D.J., Eberl, D.D., McCarty, D.K. and Meeker, G.P. (2002). Characterization and modeling of illite crystal particles and growth of mechanisms in a zoned hydrothermal deposit, Lake City, Colorado. *American Mineralogist* **87**, 1546-1556.
- [9] Brime, C. and Eberl, D.D. (2002). Growth mechanisms of low-grade illites based on the shapes of crystal thickness distributions. *Schweizerische Mineralogische und Petrographische Mitteilungen* **82**, 203-209.
- [10] Brindley, G.W., Brown, G. (1980). *Crystal structures of clay minerals and their X-ray identification*. Mineralogical Society, London, 495pp.
- [11] Drits, V., Środoń, J. and Eberl, D.D. (1997). XRD measurement of mean crystallite thickness of illite and illite/smectite: reappraisal of the Kübler index and the Scherrer equation. *Clays and Clay Minerals* **45**, 461-475.
- [12] Drits, V., Eberl, D.D. and Środoń, J. (1998). XRD measurement of mean thickness, thickness distribution and strain for illite and illite/smectite crystallites by the Bertaut-Warren-Averbach technique. *Clays and Clay Minerals* **46**, 38-50.
- [13] Droste, J.B. (1963). Clay mineral composition of evaporitic sequences. *Northern Ohio Geological Society* **1**, 47-54.
- [14] Dudek, T., Środoń, J., Eberl, D.D., Elsass, F. and Uhlik, P. (2002). Thickness distribution of illite crystals in shales. Part 1: X-ray diffraction vs. high-resolution transmission electron microscopy measurements. *Clays and Clay Minerals* **50**, 562-577.
- [15] Dunoyer de Segonzac, G. (1970). The transformation of clay minerals during diagenesis and low grade metamorphism: a review. *Sedimentology*, **15**, 281-346.
- [16] Eberl, D.D., Środoń, J. and Northrop, H.R. (1986). Potassium fixation in smectite by wetting and drying. In *Geochemical Processes at Mineral Surfaces* (Davis and Hayes, editors), ACS Symposium Series, 323, American Chemical Society.
- [17] Eberl, D.D. and Velde, B. (1989). Beyond the Kübler index. *Clay and Clay Minerals* **24**, 571-577.
- [18] Eberl, D.D., Drits, V.A., Środoń, J. and Nüsch, R. (1996). MudMaster: a program for calculating crystallite size distribution and strain from the shapes of X-ray diffraction peaks. U.S. Geological Survey, Open-File Report 96-171.

- [19] Eberl, D.D., Drits, V.A. and Środoń, J. (1998a). Deducing growth mechanisms for minerals from the shapes of crystal size distributions. *American Journal of Science* **298**, 499-533.
- [20] Eberl, D.D., Nüsch, R., Šucha, V. and Tsipursky, S. (1998b). Measurement of illite particle thicknesses by X-ray diffraction using PVP-10 intercalation. *Clays and Clay Minerals* **46**, 89-97.
- [21] Eberl, D.D., Drits V.A., Środoń, J. (2000). User's guide to GALOPER- a program for simulating the shapes of crystal size distribution- and associated programs.
- [22] U.S. Geological Survey Open File Report 00-505, 44pp.
- [23] Eberl, D.D. (2004). Quantitative mineralogy of the Yukon River system: variations with reach and season, and determining sediment provenance. *American Mineralogist*, **89**, 1784-1794.
- [24] Honty, M., Uhlík, P., Šucha, V., Čaplovičová, Franců, J., Clauer, N. and
- [25] Biroň, A. (2004). Smectite-to-illite alteration in salt-bearing bentonites (The East Slovak Basin). *Clays and Clay Minerals* **52**, 533-551.
- [26] Hower, J., Elsinger, E.V., Hower, M.E., Perry, E.A. (1976). Mechanism of burial metamorphism of argillaceous sediment: I. Mineralogical and chemical evidence. *Bulletin of Geological Society of America*, **87**, 725-737.
- [27] Ibrahim, K. and Abdelhamid, G. (1990). Al-Yamaniyya clay deposits. Internal Report, Natural Resources Authority, Amman.
- [28] Jaboyedoff, M., Bussy, F., Kübler, B. and Thelin, Ph. (2001). Illite "crystallinity" revisited. *Clays and Clay Minerals* **49**, 156-167.
- [29] Khouri, H.N. (2002). *Clays and Clay Minerals in Jordan*. Published by University of Jordan, Amman, 116p.
- [30] J. I. Langford, A rapid method for analyzing the breadths of diffraction and spectral lines using the Voigt function, *J. Appl. Cryst.* (1978). **11**, 10-14.
- [31] Lanson, B., Beaufort, D., Berger, G., Baradat, J. and Lachapagne, J.C. (1996). Late stage diagenesis of clay minerals in porous rocks : Lower Permian Rotliegendes reservoir off-shore of the Netherlands. *Journal of Sedimentary Research* **66**, 501-518.
- [32] Makhlof, I., Turner, B. and Abed, A.M. (1991). Depositional facies and environments in the Permian Umm Irna Formation, Dead Sea area, Jordan. *Sedimentary Geology* **73**, 117-139.
- [33] Merriman, R.J., Roberts, B and Peacor, D.R. (1990). A transmission electron microscope study of white mica crystallite size distribution in a mudstone to slate transitional sequence, North Wales, UK. *Contributions to Mineralogy and Petrology* **106**, 27-40.
- [34] Nieto, F. and Sánchez-Navaz, A. (1994). A comparative XRD and TEM study of the physical meaning of the white mica "crystallinity" index. *European Journal of Mineralogy* **6**, 611-621.
- [35] Saqqa, W.A., Dwairi, I.M. and Akhal, H.M. (1995). Sedimentology, mineralogical evaluation and industrial applications of the Pleistocene Al-Yamaniyyah clay deposits, near 'Aqaba, southern Jordan. *Applied Clay Science*, **9**, 443-458.
- [36] Środoń, J. (1980). Precise identification of illite/smectite interstratifications by X-ray powder diffraction. *Clays and Clay Minerals* **28**, 401-411.
- [37] Środoń, J., Eberl, D.D. and Drits, V.A. (2000). Evolution of fundamental particle size during illitization of smectite and implications for reactions mechanism. *Clays and Clay Minerals*, **48**, 446-458.
- [38] Stoffers, P. and Singer, A. (1979). Clay minerals in Lake Mobuto Seso Seko (Lake Albert) – their diagenetic changes as an indicator of the paleoclimate. *Geologische Rundschau*, **68**, 1009-1024.
- [39] Teimeh M., Taani Y., Abu Lihie O. & Abu Saad L. (1990).- A study of the Palaeozoic formations of Jordan at outcrop and in the subsurface including measured sections and regional isopach maps.- Natural Resources Authority, Geology Directorate, Subsurface Geology Division, Bulletin, Amman, 1, p. 1-72.
- [40] Tucker, M. (1981). *Sedimentary Petrology an introduction*. Blackwell Scientific Publications, Oxford, 252pp.
- [41] Tucker, M. (1991). *Sedimentary Petrology an introduction to the origin of sedimentary rocks*. 2nd edition, Blackwell Scientific Publications LTD, Oxford, 260pp.
- [42] Turner, C.E. and Fishman, N.S. (1991). Jurassic Lake T'oo'dichi': a large alkaline saline lake, Morrison Formation, eastern Colorado Plateau. *Geological Society of America Bulletin* **103**, 538-558.
- [43] Weaver, Ch. E. (1989). *Clays, Muds and Shales*. Development in Sedimentology, **44**, Elsevier, Amsterdam, 819pp.
- [44] Weibel, R. (1999). Effects of burial on the clay assemblages in the Triassic Skagerrak Formation, Denmark. *Clay Minerals*, **34**, 619-635.

Adsorption of Thorium (IV) and Uranium (VI) by Tulul al-Shabba Zeolitic Tuff, Jordan

Mona Al-Shaybe and Fawwaz Khalili*

University of Jordan, Chemistry Department, Amman – Jordan

Abstract

Tulul al-Shabba zeolite from Jordan was employed to remove actinides metal ions namely Uranium (VI) and Thorium (IV). The used Jordanian zeolitic tuff is dominated by phillipsite and chabazite. The sorption behavior of the used zeolitic tuff towards Th^{4+} and UO_2^{2+} metal(s) ions in aqueous solutions was studied by batch experiment as a function of pH, contact time and temperature and column techniques at 25.0°C and pH= 3. High initial rate of metal ions uptake was observed after 24 hr of shaking, and the uptake have increased with increasing pH and have reached a maximum at pH = 3. Tulul al-Shabba zeolitic tuff has shown high metal ion uptake capacity toward Thorium (IV) than Uranium (VI). Adsorption data was evaluated according to the Pseudo second-order reaction kinetic.

Adsorption isotherms were studied at temperature 25°C, 35°C and 45°C. The Langmuir, Freundlich and Dubinin-Raduskevich (D-R) adsorption models equations were applied, and the proper constants were derived. It was found that the adsorptivity process is enthalpy driven for Thorium (IV) and Uranium (VI).

Recovery of Thorium (IV) and Uranium (VI) ions after adsorption was carried out by treatment of the loaded zeolitic tuff in the column with 0.1N HNO_3 , 0.1N H_2SO_4 , 0.1 - 1×10^{-4} N EDTA, and 0.1N sodium acetate. The best percent recovery for Thorium (IV) was obtained when 1×10^{-4} N EDTA was used, while for Uranium (VI) when 0.1N H_2SO_4 was used.

© 2009 Jordan Journal of Earth and Environmental Sciences. All rights reserved

Keywords Jordanian zeolitic tuff, Thorium (IV), Uranium (VI), adsorption, isotherm, kinetic, recovery.

1. Introduction

Jordan is rich in industrial rocks and minerals. Zeolitic tuff is widely distributed in Jordan (Khoury et al., 2003). The huge reserves of the zeolitic tuff have encouraged the authors to carry out this work since investment projects of radioactive minerals have a priority in Jordan. Uranium is enriched in the Phosphorite and Chalk Marl Units of central Jordan (Daba-Siwaqa area 60 km south of Amman). The area is currently under investigation by Areva Co., and huge reserves are expected. UO_2 concentrations range between 140 – 2200 ppm in central Jordan. Thorium is associated with the Dubaydib Sandstone Formation, southern Jordan, where the level of thorium oxide reaches 400 ppm (Khoury, 2006).

The methods for separation, collection and detection of radionuclides are similar to ordinary analytical procedures and employ many of the chemical and physical principles that apply to the non-radioactive nuclides. However, some important aspects of the behavior of radionuclides are significantly different, resulting in challenges to the radiochemists to find means for isolation of a pure sample for analysis. There are many methods for the separation and purification of radionuclides. The oldest method, used in the large-scale separation of actinides, is the precipitation

technique. However, this process produces complex products and impure substances.

Many ion-exchange separations of radionuclides are based on the formation of complex species between the metal and an extractant in the organic phase as in the extraction of Europium (III), Thorium(IV) and Uranium(VI) with didodecylphosphoric acid (HDDPA), (Kondo et al.1989); (Nazzal, 2006); (Khaled and Khalili, 1999). The use of solids for removing substances from either gaseous or liquid solution has been widely used since biblical times. This process, known as adsorption, involves nothing more than the preferential partitioning of substances from the gaseous or liquid phase onto the surface of solid substrate. From the early days of using bone char for decolorization of sugar solutions and other foods to the later implementation of activated carbon for removing nerve gases from the battlefield and to today's thousands of applications, the adsorption phenomenon has become a useful tool for purification and separation (Slejko, 1985 and Lazaridis et al., 2004).

Ion exchange is a process by which ions held in a porous, essentially insoluble solid exchange for ions in a solution that is brought in contact with solid. The ion exchange properties of clays and zeolite have been recognized and studied for more than a century (Skoog et al.1994); (Harvey, 2000). The main advantages of ion exchange over chemical precipitation are removal of metal value, selectivity, and less sludge volume produced-meeting the strict discharge specifications. In ion exchange system, polymeric resins as well as zeolite are usually

* Corresponding author. fkhilili@ju.edu.jo

employed. The availability of natural zeolite in many countries provides low-cost treatment by ion exchange systems (Ali and El-bishtawi, 1997).

The adsorption of Thorium (IV) and Uranium (VI) by zeolite isolated from Metaxades (Greece), using batch type method, was studied by Misaelides et al. (2006). They found that NaCl pretreated zeolite material improved the thorium uptake but not the uranium; this can be attributed to the improvement of the ion-exchange properties of the microporous minerals (Misaelides et al. 1995). The adsorption behavior of Th(IV) onto the PAN (Polyacrylonitrile)/zeolite, zeolite isolated from Manisa-Gordes (Turkey), composite adsorbent was investigated. It was found that PAN (Polyacrylonitrile)/zeolite composite adsorbent is economical and an effective sorbent for Th(IV) ions, and the composite adsorbent exhibited an excellent adsorption selectivity for Th(IV) (Kaygun and Akyil, 2007).

The following work aims at studying the adsorption behavior of uranium and thorium by using the zeolitic tuff from Tulul Alshahba of Jordan. The batch technique of removing uranium and thorium from solution was carried out at specific conditions: pH= 1.0, 2.0, and 3.0, at temperatures 25.0°C, 35.0°C and 45.0°C at different contact time (kinetic) and with the same ionic strength (0.1M NaClO₄). The column experiment was carried out at 25.0°C and pH= 3. Analysis of data will be based on adsorption models such as Langmuir, Freundlich and Dubinin–Radushkevich (D–R). Adsorption kinetics was applied in order to determine adsorption mechanism and adsorption characteristic constants. The effective adsorption from column and the coefficient of recovery with different ligands was studied for the adsorbed metal ions on the zeolitic tuff.

2. Methodology

2.1. Materials and Instrumentation

All reagents used in this study were analytical grade. Th(NO₃)₄.5H₂O is from Riedel DeHäen Chemical company Inc, UO₂(NO₃)₃.H₂O, sodium perchlorate, sodium acetate, sulfuric acid and nitric acid are from Merck, EDTA is from PARK, 35% Hydrochloric acid from analytical Rasayan, Arsenazo (III) Indicator from BDH Chemicals Ltd. Infrared spectra of the zeolitic tuff was recorded using a Thermo Nicolet Nexus 870 FTIR. The thermal gravimetric analysis (TGA) of the zeolitic tuff was studied using NETZSCH STA 409 PC. The main and minor composition of zeolitic tuff was studied by X-ray powdered diffraction method (Shimadzu PXR-6000). A pH meter model Cyberscan waterproof PC 300 was used for pH measurements. The analytical balance that was used is Shimadzu and its type is AW120, and its readability is 0.1 mg. Shaking of samples was done by using Clifton Shaker equipped with a thermostat. UV-VIS Spectrophotometer was from Spectroscan model 80DV with software UV Win5 v5.0.5.

2.2. Zeolitic tuff preparation.

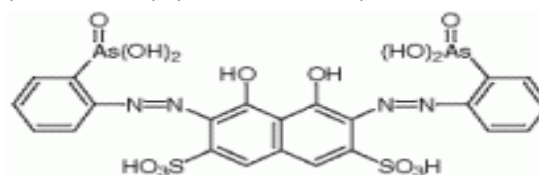
Zeolitic tuff samples have a particle size of (250-500 µm) were chosen for this study. The zeolitic tuffs samples were converted to Na - type, by adding a 250 ml of 2M

NaCl to each 200g of zeolitic tuff, and shaking for 24hr. The exchangeable cations in the zeolitic tuff structure were replaced by Na⁺ ions. After shaking, the zeolitic tuff samples were washed several times with deionized water to get rid of excess NaCl. The samples were dried in an oven at 100°C overnight.

2.3. Spectrophotometric procedure for Thorium (IV) and Uranium(VI).

2.3.1. Preparation of Arsenazo (III) indicator solution.

A 0.10% aqueous solution of Arsenazo (III) was used as a spectrophotometric reagent in the determination of Thorium(IV) and Uranium(VI) ion concentration (Savvin, 1961); (Khalili et al., 2008).



The spectrophotometric determination of Thorium (IV) and Uranium (VI) ions in the aqueous solution was carried out as follows:

Transfer 0.5 ml of Arsenazo (III) indicator to a 10 ml of 9.0 M Hydrochloric acid solution, and add 1.5 ml of the aqueous Thorium (IV) test solution or 2.0 ml in the case of Uranium (VI). Dilute the volume to 25.0 ml by addition of water. Absorption measurement was carried out using a (1.0 cm) quartz cell within one hour of sample preparation at 660 nm wavelength for Thorium (IV) and 650 nm wavelength for Uranium (VI).

2.4. Adsorption experiments

2.4.1. Metal ion-uptake by zeolitic tuff using batch adsorption.

Batch adsorption was carried out using Pyrex glass flasks. Experiments for determination the equilibrium time for the adsorption process involving 0.05 g ± 0.1 mg of the zeolitic tuff, 50.0 ml of metal ion was then added, and the mixed solutions were mechanically shaken. The contact time was varied from 0.25 hour to 24 hours at 25 °C, the concentration of the metal ion remaining was determined with UV- VIS. Similar experiments were also carried out at different pH 1.0, 2.0 and 3.0.

The mass of the adsorbed metal per unit mass of the zeolitic tuff was calculated using equation (1).

$$q = (C_i - C_e) * V / m \quad (1)$$

(Fendorf and Li, 1996; Lee et al., 2000).

q: Metal ion uptake by zeolitic tuff in (mg M / g zeolitic tuff).

C_i: Initial metal concentration (ppm).

C_e: The residual concentration of metal ion in solution at equilibrium in (ppm).

m: Mass of zeolitic tuff (g).

The percentage of metal ion loading by zeolitic tuff expressed as percentage uptake was calculated (Eq. (2)) where

$$\% \text{ Metal uptake} = C_e / C_i * 100 \quad (2)$$

$$K_d = [(C_i - C_f) / C_f] V / m \quad (\text{mL} / \text{g}) \quad (3)$$

Calculations were made by using these data, and adsorption curves were obtained.

2.5. Adsorption isotherm studies.

An accurate mass of 0.05 g of zeolitic tuff measured to the nearest 0.1 mg was shaken with 50.0 ml of metal ion solution at different concentrations, in a thermostatted shaker for 24h (which had been found sufficient to ensure equilibrium) at 25.0°C, 35.0°C, and 45.0 °C. The adsorption isotherms were studied, using similar conditions at different pH=1.0, 2.0, and 3.0.

2.6. Metal ion-uptake by zeolitic tuff using column experiment.

Glass column of 150 mm length and 10 mm inner diameter was used in this experiment. The column was packed with $1.00\text{g} \pm .0001\text{g}$ of zeolitic tuff, a sample volume of 50.0 ml containing U(VI) or Th(IV) of 1000ppm was passed through the column at a flow rate of 1.0 ml/ 2min. The eluate was collected in a 50 ml volumetric flask, and concentration of the metal ion was then determined by using UV-VIS.

2.7. Desorption studies.

Desorption of the U(VI) and Th(IV) was carried under column condition, where zeolitic tuff was loaded with each metal ion as described in (section 3.6). A 50.0 ml of the

following four eluting agents, 0.1N and 0.01N HNO₃, 0.1N H₂SO₄, 0.1 to $1 \cdot 10^{-4}$ N EDTA, and 0.1N CH₃COONa were used for metal ion recovery from adsorbed zeolitic tuff, keeping the flow rate of elution at 1 ml/2min. The concentration of metal ion in the eluate was collected in five 10 ml portions, and then determined using UV-VIS.

3. Results and Discussion

3.1. Characterization of the zeolitic tuff sample.

The obtained zeolitic tuff was characterized by Fourier transform infrared (FTIR) spectroscopy, Thermogravimetric analysis (TGA) and X-ray powder diffraction (XRD) technique.

3.2. Fourier transform infrared (FTIR).

The structural information of the zeolite tuff was obtained by FTIR spectroscopy Figure (1) shows H-bonded O-H stretching at 3443.9 cm⁻¹, H₂O bending at 1640.7 cm⁻¹, 1428.6 cm⁻¹ asymmetric stretching vibrations of the carbonate in the sample, 1019.1 cm⁻¹ strong band due to phillipsite symmetric stretching vibration of silicate group, 610.2 cm⁻¹ symmetric stretching vibration of silicate group for forsterite and 450.6 cm⁻¹ bending vibrations for phillipsite. Calcite and forsterite are normally present in Jordanian zeolitic tuff.

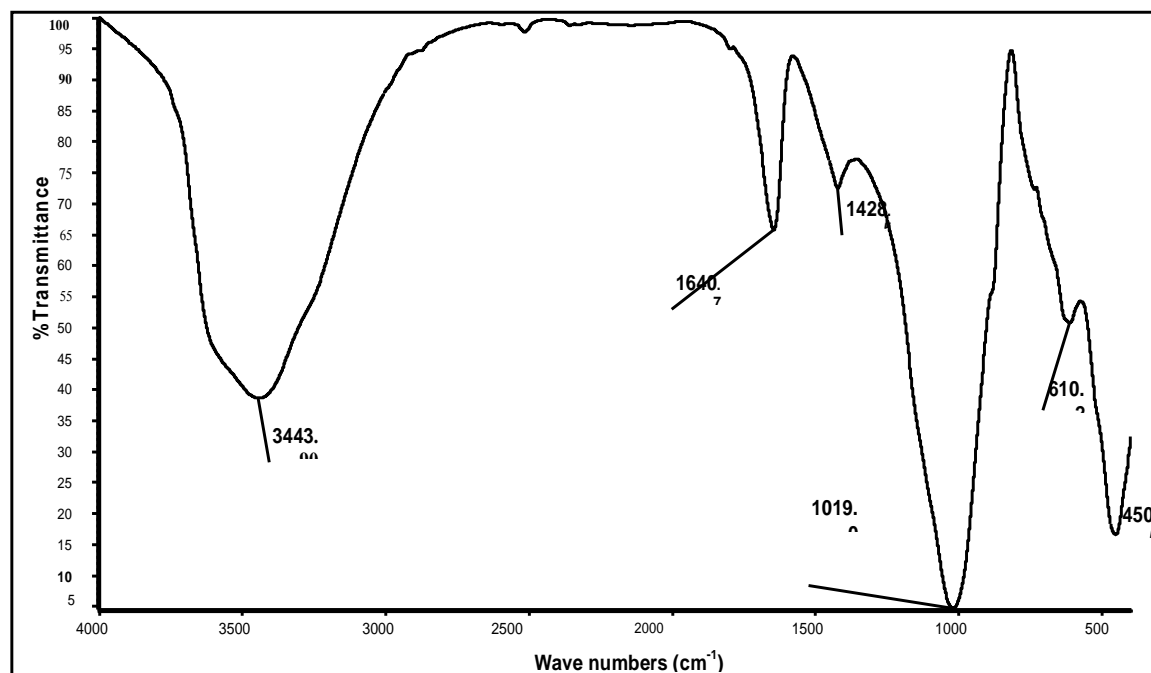


Figure (1): The FTIR spectrum of zeolitic tuff at 25°C.

3.3. Thermal properties.

Thermal behavior of zeolitic tuff was investigated by using TGA. The TGA thermogram is given in Figure (2). The temperature ranges are 45-400, 400-800 and 800-1000°C corresponding to the loss of external, loosely bound and tightly bound water, respectively. The weight

losses were found as 8.64, 3.89 and 13.93% by weight for the external, loosely and tightly bound water for the examined zeolitic tuff (Duvarcı et al., 2006). The 800-1000°C could be also related to the loss of CO₂ as a result of decarbonation of calcite.

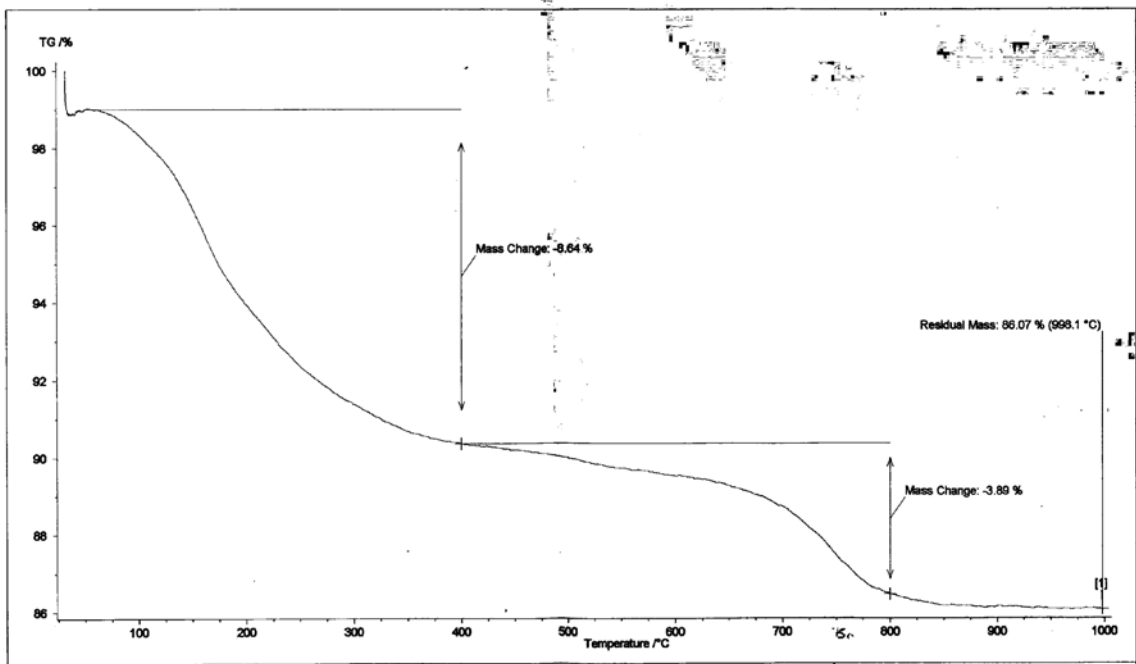


Figure (2): TGA thermogram of zeolitic tuff.

3.4. X-ray powder diffraction analysis.

The X-ray diffraction results have indicated that the examined zeolitic tuff sample is rich in Phillipsite and Chabazite together with calcite and forsterite; the XRD chart is shown in Figure (3).

3.5. Rate of metal ion sorption by zeolitic tuff

The rate of metal ions uptake by zeolitic tuff was determined at different time (0.25, 0.5, 1.0, 2.0, 4.0, 6.0, 18.0 and 24 hr), with three concentrations (5, 10, 35 ppm) at different pH (1.0, 2.0 and 3.0) and 25 °C.

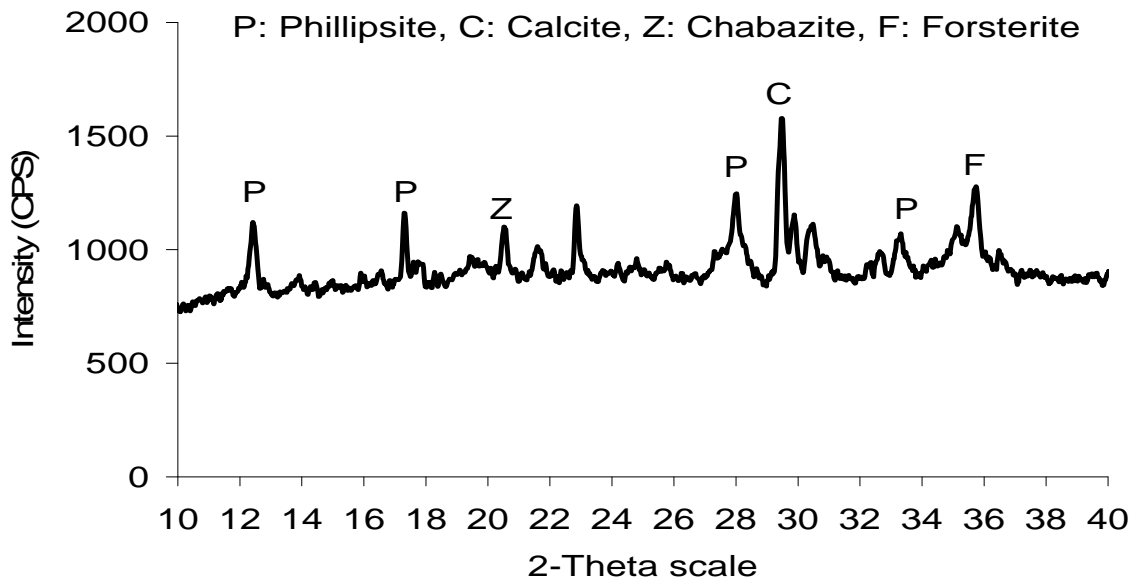


Figure (3): X-ray powder diffraction chart.

Samples of these results are shown in Figures (4 -5). Shaking for 24h has been found sufficient to ensure equilibrium for all the experiments.

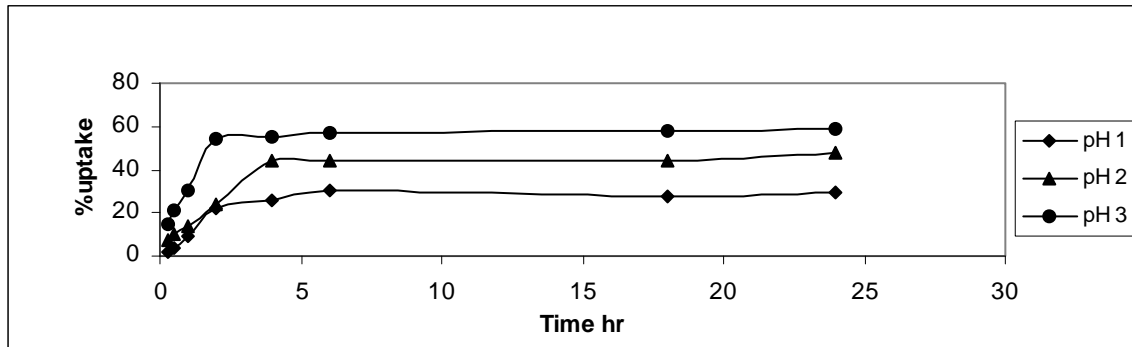


Figure (4): Thorium (IV) percentage uptake by zeolitic tuff at pH 1.0, 2.0 and 3.0 at 25°C and concentration 35ppm.

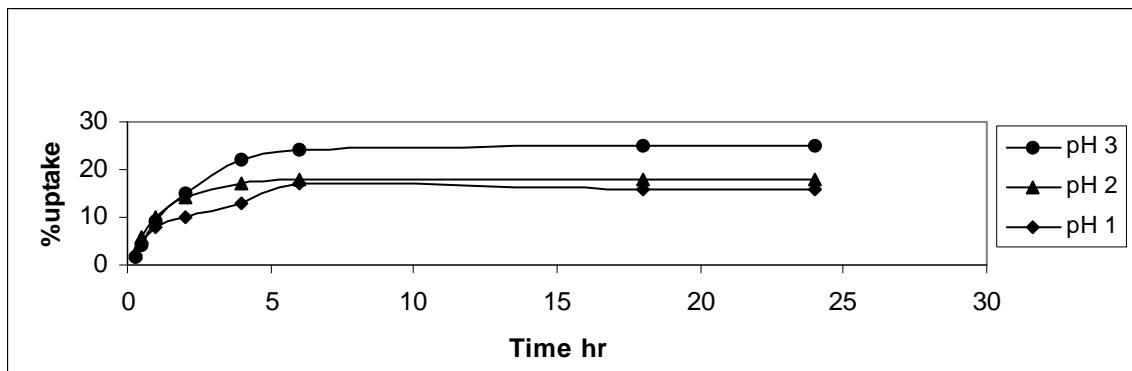


Figure (5): Uranium (VI) percentage uptake by zeolitic tuff at pH 1.0, 2.0 and 3.0 at 25°C and concentration 35 ppm.

3.6. Pseudo-second-order reaction kinetic.

Adsorption data was evaluated according to the Pseudo second-order reaction kinetic proposed by Ho and McKay (1998):

$$dq_t/dt = k_2(q_e - q_t)^2 \quad (4)$$

where k_2 is the second order reaction constant. If Eq. (4) is integrated, the following expression is obtained:

$$1/(q_e - q_t) = k_2 t + C_2 \quad (5)$$

In Eq. (5), C_2 is the integration constant of the second order reaction kinetic. Applying the

initial condition $q_t = 0$ at $t = 0$ we get $C_2 = 1/q_e$ and on elementary rearrangement this equation can be written as

$$t/q_t = 1/k_2 q_e^2 + t/q_e \quad (6)$$

In this study, the initial Thorium (IV) and Uranium(VI) concentrations were determined as 5, 10, 35 ppm . The dependences of these concentrations against time are shown in Fig. 4 and 5 for Thorium (IV) and Uranium (VI) at 25°C and pH = 3 as an example.

For both metals, the curves in the plot of t/q_t against t are linear and k_2 rate constants can be calculated from the slope of these curves as shown on figures (6-7).

The values of q_e , calculated are found from the intersection points of the second order reaction kinetic curves.

Table1. Presents all the data at different pH (1.0,2.0 and 3.0) and 25 °C.

Since the difference between q_e calculated and q_e experimental values is very small and the correlation coefficient (R^2) values for the second order reaction equation plots are high, it is seen that the Thorium (IV) and Uranium (VI) removal by zeolitic tuff is well described by the second order reaction kinetic.

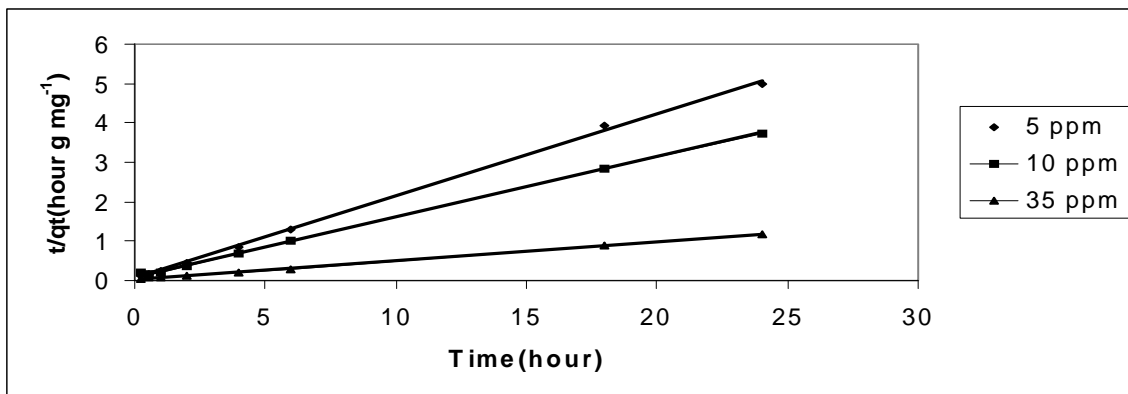


Figure (6): Pseudo-second order sorption kinetics of Thorium(IV) onto zeolitic tuff at various initial concentrations at 25°C and pH = 3 .

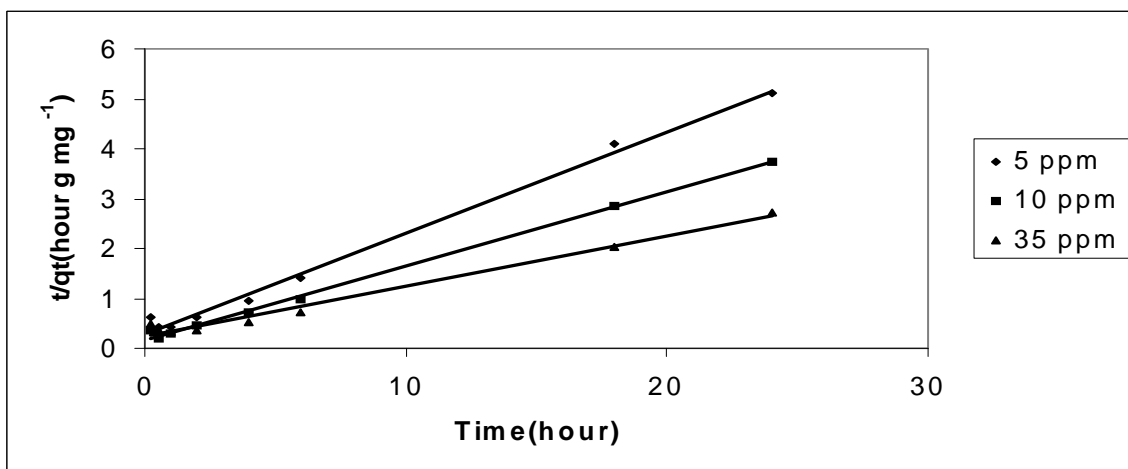


Figure (7): Pseudo-second order sorption kinetics of Uranium (VI) onto zeolitic tuff at various initial concentrations at 25°C and pH = 3.

Table (1): Adsorption rate constants, calculated q_e , experimental q_{exp} and R^2 values for the second order reaction kinetics of removal of Uranium and Thorium by natural clay at pH = 1, 2, 3 and 25 °C.

Initial metal concentration (mg/L)	Pseudo-second order pH = 1			Pseudo-second order pH =2			Pseudo-second order pH =3		
	k_2 (g/mg min)	q_e (mg/g) (q_{exp} (mg/g))	R^2	k_2 (g/mg min)	q_e (mg/g) (q_{exp} (mg/g))	R^2	k_2 (g/mg min)	q_e (mg/g) (q_{exp} (mg/g))	R^2
Thorium(IV)	0.14	4.6	0.99	0.34	4.8	0.98	0.79	4.8	0.99
		4.3			4.6			4.8	
		7.7			7.8			6.5	
10 ppm	0.05	7.0	0.97	0.08	7.8	0.99	0.29	6.4	0.97
35 ppm		11.1			17.7			21.2	
	0.04	10.0	0.99	0.03	16.8	0.99	0.07	20.7	0.99
Uranium(VI)	0.14	2.8	0.96	0.18	4.1	0.98	0.14	4.9	0.99
		2.5			3.8			4.7	
		4.2			4.8			6.7	
10 ppm	0.20	3.9	0.99	0.44	4.8	0.99	0.13	6.4	0.99
35 ppm		6.0			6.6			9.9	
	0.14	5.6	0.99	0.17	6.3	0.99	0.04	8.8	0.98

3.7. Adsorption isotherms.

3.7.1. Langmuir isotherm.

Langmuir isotherm models the single coating layer on adsorption surface. This model supposes that the adsorption takes place at a specific adsorption surface. The attraction between molecules decreases as they are getting further from the adsorption surface (Ünlüa and Ersoz, 2006). Langmuir isotherm can be defined according to the following formulas:

$$q_e = V_m K C_e / (1 + k C_e) \tag{7}$$

Where q_e is the amount of adsorbed heavy metal per unit clay mass (mg/g), V_m is the monolayer capacity, K is the equilibrium constant and C_e is the equilibrium concentration of the solution in (ppm).

Eq. (7) can be written in the following linear form:

$$C_e/q_e = 1/KV_m + C_e/V_m \tag{8}$$

The results obtained from the empirical studies were applied to Langmuir isotherm.

The plot of the linear form of Langmuir equation for Thorium (IV) and Uranium (VI) adsorption on zeolitic tuff is shown in Figures (8-9) as an example, and the values for K and V_m are shown in Tables (2-3).

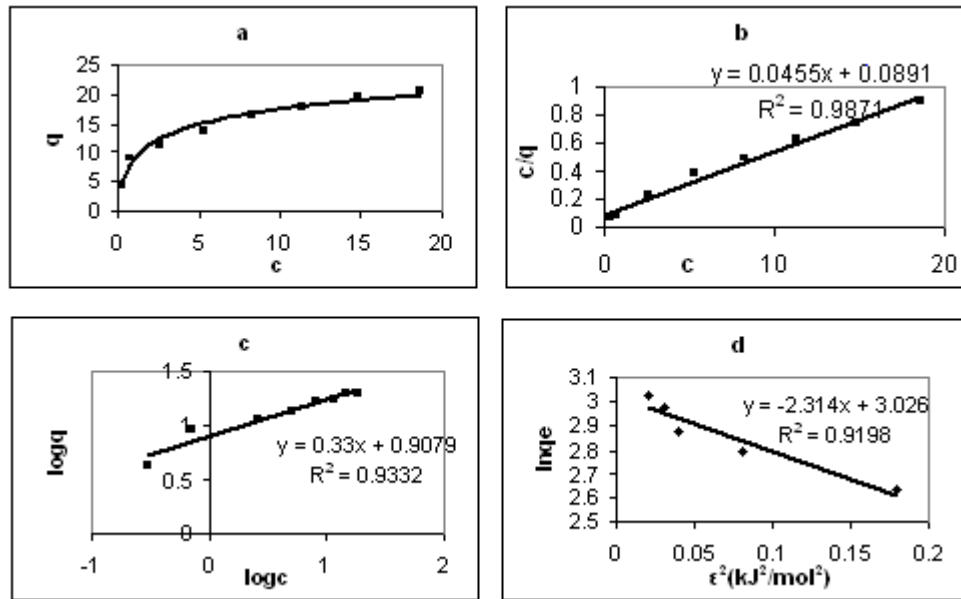


Figure (8): Plot of (a) adsorption isotherm of Th(IV), (b) linearized Langmuir (III), (c) linearized Freundlich (d) D-R at pH=3 and 25°C.

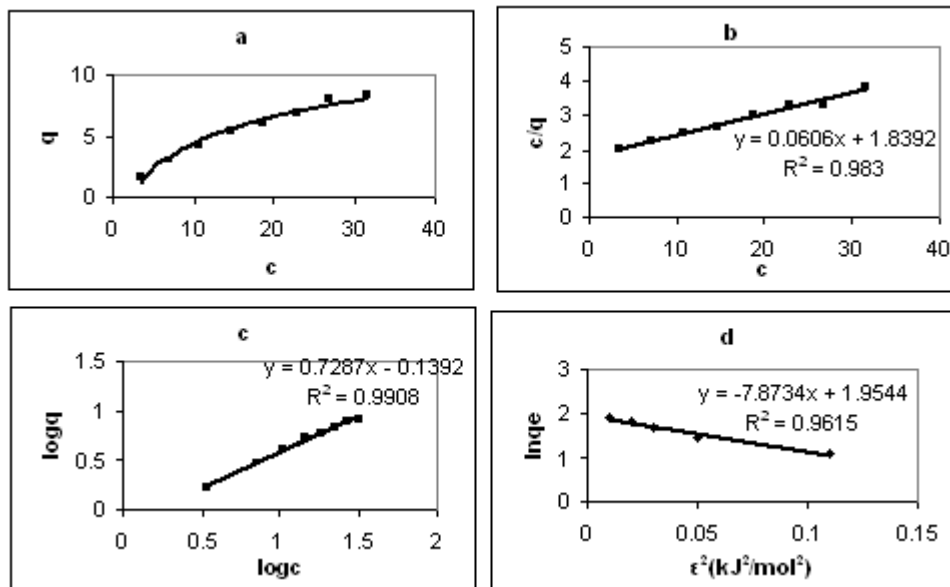


Figure (9): Plot of (a) adsorption isotherm of U(VI), (b) linearized Langmuir (III), (c) linearized Freundlich (d) D-R at pH=3 and 25°C.

3.8. Freundlich isotherm.

Freundlich isotherm (Freundlich, 1932) is used for modeling the adsorption on heterogeneous surfaces. This isotherm can be explained by the following equation:

$$q_e = K_f C_e^{1/n} \tag{9}$$

where K_f is the Freundlich constant (mg/g), and $1/n$ is the adsorption intensity:

The linear form of the Eq. (9) can be written as:

$$\log q_e = \log K_f + 1/n \log C_e \tag{10}$$

It is seen that the Freundlich isotherm curves are linear both in Thorium(IV) and Uranium(VI) adsorption. The Freundlich constant K_f and adsorption intensity $1/n$ for Thorium(IV) and Uranium(VI) are calculated from the slopes of these curves (Tables 2-3).

3.9. Dubinin–Radushkevich (D–R) isotherm.

Langmuir and Freundlich isotherms are insufficient to explain the physical and chemical characteristics of adsorption. Dubinin and Radushkevich (1947) isotherm is commonly used to describe the sorption isotherms of single solute systems. In previous studies, D–R isotherm was used to express the adsorption processes of bentonite (S. Tahir, and R. Naseem, 2006). The D–R isotherm, apart from being analogue of Langmuir isotherm, is more general than Langmuir isotherm as it rejects the homogeneous surface or constant adsorption potential (Kilislioğlu and Bilgin, 2003).

The D–R isotherm is expressed as:

$$\ln q_e = \ln V_m - K' \epsilon^2 \tag{11}$$

Where q_e is the heavy metal amount (mg/g) that is removed per unit clay mass, V_m is the D–R adsorption capacity (mg/g), K' is the constant related with adsorption energy (mol^2/kJ^2), and ϵ is the Polanyi potential.

The Polanyi potential ϵ can be given as (Polanyi, 1963):

$$\epsilon = RT \ln(1 + 1/C_e) \tag{12}$$

Where R is the gas constant ($\text{kJ K}^{-1} \text{mol}^{-1}$), and T is the temperature (K).

The main energy of adsorption (E) is calculated by using the following formula:

$$E = (2K')^{-0.5} \tag{13}$$

Where E gives information about the physical and chemical features of adsorption.

The D–R isotherm is applied to the data obtained from the empirical studies. A plot of

$\ln q_e$ against ϵ^2 is given in Figures (8-9). As it is seen in Figures (8-9), the D–R plot yields a straight line.

In the D–R isotherm, adsorption capacities (V_m), adsorption energy constants (K') and the main adsorption energies (E) are calculated for Thorium(IV) and Uranium(VI) removal.

All of the isotherm model parameters for the adsorption of Thorium(IV) and Uranium(VI) are provided in Tables (2-3).

Table (2): The R^2 , q_m , K_L , K_F and n values obtained from Langmuir (L), Freundlich (F) and Dubinin-Radushkevich (D-R) plots for Thorium(IV).

pH	T °C	R ²	L		F			D-R		R ²	K _d (mL/g)	
			q _m (mg/g)	K _L (L / mg)	R ²	K _F	n	K' (mol ² /kJ ²)	V _m (mg/g)			E (kJ/mol)
1.0	25	0.9515	17.0	0.17	0.9777	4.22	2.69	0.2451	10.85	1.43	0.9684	840
	35	0.9455	14.0	0.14	0.9559	3.50	2.88	-	-	-	-	680
	45	0.9251	13.5	0.12	0.9578	3.08	2.74	-	-	-	-	450
2.0	25	0.9614	21.0	0.59	0.9185	8.16	3.60	0.0632	16.5	2.81	0.8703	940
	35	0.9753	18.8	0.62	0.9118	7.49	3.37	-	-	-	-	900
	45	0.9258	17.7	0.34	0.9258	6.64	3.58	-	-	-	-	520
3.0	25	0.9871	21.9	0.51	0.9332	8.09	3.03	0.0967	16.49	2.27	0.7962	980
	35	0.9790	19.4	0.46	0.9123	7.49	3.37	-	-	-	-	930
	45	0.9520	18.1	0.41	0.9753	7.42	3.87	-	-	-	-	600

Table (3): The R², q_m, K_L, K_F and n values obtained from Langmuir (L), Freundlich (F) and Dubinin-Raduskevich (D-R) plots for Uranium(VI).

pH	T °C	R ²	L		F			D-R				
			q _m (mg/g)	K _L (L / mg)	R ²	K _F	n	K'(mol ² /kJ ²)	V _m (mg/g)	E (kJ/mol)	R ²	K _d (mL/g)
1.0	25	0.8342	10.8	0.04	0.9737	0.72	1.66	2.4956	8.16	0.45	0.939	400
	35	0.9918	8.3	0.06	0.9894	0.72	1.69	-	-	-	-	340
	45	0.9858	5.3	0.08	0.9859	0.56	1.85	-	-	-	-	270
2.0	25	0.9481	15.0	0.05	0.9964	1.05	1.55	2.3345	6.86	0.46	0.8961	440
	35	0.9219	13.0	0.04	0.9979	0.74	1.53	-	-	-	-	360
	45	0.9740	11.0	0.06	0.9801	0.98	1.55	-	-	-	-	300
3.0	25	0.9619	17.7	0.05	0.9849	1.16	1.48	3.8657	6.64	0.35	0.9615	480
	35	0.9885	17.1	0.04	0.9737	0.72	1.66	-	-	-	-	400
	45	0.9830	16.5	0.03	0.9908	0.73	1.37	-	-	-	-	320

3.10. Comparing adsorptivity between Thorium(IV) and Uranium(VI).

The correlation coefficient (R²) values for the three types are very close, so we cannot assume that the adsorption behaviour fit one of them better, and it is a homogeneous or a heterogeneous one. Depending in the values of q_m and n in Tables (2-3), the adsorption of Thorium(IV) is more favourable than Uranium(VI) metal ions on zeolitic tuff at the same pH and temperature. The D-R isotherm showed the E values for Thorium(IV) are higher than Uranium(VI), but both values are less than 8 kJ/mol, which means that it is a physisorption process.

These observations can be explained in terms of the following two factors:

1. Hydration energy.

The adsorptivity of metal ions (q_m) on zeolitic tuff was found to be directly proportional to the ionic radius. This is due to the decrease of hydration (-ΔH_h) as the ionic radius increases (Hunt, 1965). Increasing the hydration energy due to increase in the hydration shell makes it more difficult for metal ion to discharge the water of hydration. The formation of aqua complex [M(OH₂)_m]ⁿ⁺ takes place (where m is larger than six, perhaps eight or nine), the aqua complex, having m H₂O molecules surrounding the central ion, has a definite structure and the cloud of water molecules (hydration shell) has another geometry than the rest of the water. Thus, when M(NO₃)_n salts are dissolved in water there will be very little attraction between [M(OH₂)_m]ⁿ⁺ and the solvated NO₃⁻ ion. Unless the other ions or ligands have a strong structure breaking influence, the sheath of water molecule will protect the metals ions from influence of other anions or ligands. When complexes are formed, the approach of a ligand will interfere with the hydration shell, and the ordered geometry will break down (Sinha, 1966). A stronger hydration shell will surround small metal ion, which has smaller radius than the metal ion with larger radius. The adsorptivity of an ion of large radius is larger than small radius.

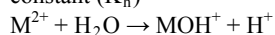
Large charge-to-size ratio results in an increase in hydration energy, which means that the hydrated ion

prefers the solution phase, where it may satisfy its hydration requirements. Ions with lower hydration energy prefer the zeolitic tuff phase. Table (4) shows that Thorium has lower hydration energy than Uranium- this means Thorium can exchange easily at the zeolitic tuff surface.

The values of electronegativity for Uranium and Thorium are shown in Table (4). Thorium(IV) is more electropositive than Uranium(VI). This means that Thorium(IV) binding onto the negative surface and q_m should be stronger and higher respectively, than Uranium(VI).

2. Hydrolysis Reaction.

Hydrolysis reaction can be represented by a hydrolysis constant (K_h)



From the value of K_h in Table (4), the following sequence was observed:

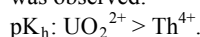


Table (4): Chemical properties of Thorium(IV) and Uranium(VI).

Metals	Th(IV)	U(VI)
Ionic radius (Å)	1.19	0.97
Electronegativity	1.30	1.38
Hydrolysis constant at 0.1M NaClO ₄ (pK _h)	4.00	4.69
Hydration energy (kJ / mol)	-3332	-3958

This indicates that at lower pK_h value the metal ion can diffuse easily and has a stronger binding strength at the zeolitic tuff surface. Thorium(IV) has a lower pK_h, so a lower resistance to reach the active sites. As a conclusion: the binding strength of Th⁴⁺ > UO₂²⁺ at the zeolitic tuff surface due to the hydration and hydrolysis behavior.

3.11. Effect of pH.

Tables 2 & 3 show that as the pH increases the q_m values increase for Thorium(IV) and Uranium(VI). This can be explained by the following:

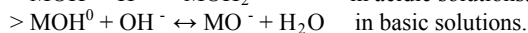
In solutions of pH less than 3, Thorium shows a small tendency to hydrolyze, and the exchangeable Thorium ion (Th⁴⁺) dominates. In pH 3 and greater, mononuclear (e.g., [ThOH]³⁺, [Th(OH)₂]²⁺ and [Th(OH)₃]⁺) as well as polynuclear-polymeric (e.g., [Th₂(OH)₂]⁶⁺) hydrolysis

products of the general type $[Th_x(OH)_y]^{(4x-y)+}$ are formed. The hydroxyl number of these species depends on the Thorium concentration and rises rapidly with increasing pH. Most of the hydrolysis species can be exchanged or adsorbed on the zeolitic tuff. Thorium(IV) is the least hydrolyzed tetravalent ion when compared with other tetravalent actinides. In the case of uranium, the uranyl ion $(UO_2)^{2+}$ is the most dominant species in low pH solutions and Uranium uptake is mainly due to uranyl ion adsorption.

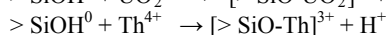
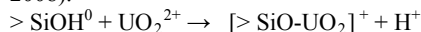
The radius of the hydrated uranyl cation can be assigned to determine how closely the centers of two ions actually approach each other in solid substances, and then to assume that such a distance is equal to the sum of the radii of the two ions. Theoretically, a rough estimation of the ionic radius of a complex ion ML_n is given as the sum of the ionic radius of the cation M and the mean diameter of the ligand L. Since the ionic radius of the uranyl ion is equal to 1.8 Å and the atomic radii of oxygen and hydrogen are 0.74 Å and 0.37 Å respectively, a rough estimation of the hydrated uranyl ion diameter gives a result higher than 6.5 Å. The estimated size of hydrated uranyl cation $[UO_2(H_2O)_5]^{2+}$ is much greater than the mean dimension of the zeolitic tuff channels; therefore the uranium (VI) attenuation by natural zeolitic tuff cannot be attributed to the cation exchange mechanism (Krestou et al. 2003). Hydrolysis of the uranyl ion practically begins at pH 3 and mononuclear (e.g., $[UO_2(OH)]^+$) as well as polynuclear (e.g., $[(UO_2)_2(OH)_2]^{2+}$, $[(UO_2)_3(OH)_3]^{2+}$) hydrolysis products of the general type $[UO_2)_x(OH)_y]^{(2x-y)+}$ are formed. The occurrence of species such as $U_2O_5^{2+}$, $U_3O_8^{2+}$ and polymeric species of the type $UO_2(UO_3)_n^{2+}$ has also been suggested. The $(UO_2)^{2+}$ hydrolysis products can be adsorbed on zeolitic tuff. However, the formation of phases such as $UO_2(OH)_2$, which can be precipitated, is also possible. The metal species, present in the aqueous solutions, strongly depend on the pH.

The adsorption of some species by ion exchange processes can be considered to take place at the microporous minerals (zeolitic tuffs, clay minerals and micas). Where individual metal species penetrate into the lattice through the micropores and replace exchangeable ions (mainly Na^+ and K^+) but adsorption (surface uptake) takes place both on the microporous and the non-microporous minerals (feldspars, SiO_2 phases) (Misaelides et al., 1995).

In Zeolitic tuff, the silanol ($> Si-OH$) and Aluminol ($> Al-OH$) groups are formed on the edge surface of the material. Depending on the solution pH, these groups behave as basic or acidic solutions according to the following reactions:



The Uranium(VI) and Thorium(IV) species are preferably adsorbed on the silanol groups, which are not protonated at pH equals 3 rather than on the aluminol groups, and which are strongly protonated in the same pH region (Talip et al., 2008).



So as the pH increases the amount of deprotonated SiOH increases. Therefore, the negative charge on the surface increases, and the adsorbed metal ions increase.

3.12. Effect of temperature.

From the data in Tables (2&3), the relation $\ln K_d$ vs. $1/T$ was plotted and from the van't Hoff equation, ΔH and ΔS were calculated for Th(IV) and U(VI) as shown in Table (5). The adsorption process is enthalpy and entropy driven for Thorium(IV) and Uranium(VI). The negative values of enthalpy show that the sorption of Thorium(IV) and Uranium(VI) on zeolitic tuff is an exothermic process. Values of the free energy (ΔG) of adsorption for the adsorption of Thorium(IV) and Uranium(VI) on zeolitic tuff are negative, showing that adsorption processes are spontaneous in nature.

Table (5): Enthalpy, entropy and free energy (298 K) values for the adsorption of Thorium(IV) and Uranium(VI) on zeolitic tuff.

Metal	Th(IV) pH=1	Th(IV) pH=2	Th(IV) pH=3	U(VI) pH=1	U(VI) pH=2	U(VI) pH=3
ΔH (kJ/mol)	-23.8	-22.7	-18.9	-14.7	-14.6	-15.1
ΔS (J/mol.K)	-23.7	-18.5	-5.6	0.4	1.1	0.6
ΔG (kJ/mol)	-16.7	-17.2	-17.1	-14.6	-14.3	-14.9

3.13. Column Experiments.

3.14. Metal Ion Uptake by Zeolitic tuff.

The metal ion uptake by zeolitic tuff using column experiment for Thorium(IV) and Uranium(VI) were

determined at pH= 3, 25°C, initial concentration of 1000 ppm and a flow rate of 1 ml /2 min. The percent uptake for metal ions is represented in Table (6).

Table (6): Metal ion uptake using column experiment at pH= 3, 25°C.

Metal Ion	C _i (ppm)	Final concentration (ppm)	Loaded concentration (ppm)	% Uptake
Thorium(IV)	1000	69.0	931	93.1
Uranium(VI)	1000	118.0	882	88.2

It can be seen that the uptake capacities of the metal ions fall in the order Th(IV) > U(VI).

3.15. Desorption studies.

A four eluting agents, 0.1N HNO₃, 0.1 H₂SO₄, 0.1-1*10⁻⁴N EDTA (pH= 3.0), and 0.1N CH₃COONa were used for removal of metal ions, keeping the flow rate of elution at 1 ml /2 min. The eluate was collected in five

portions, 10 ml each; the results are expressed as percent recovery and represented in Tables (7& 8).

Depending on the values of percentage of accumulative recovery, in Table (7) and Table (8), the following trend was observed for the eluting agents of Th(IV) from zeolitic tuff:

1*10⁻⁴N EDTA > 0.001N EDTA > 0.01 N EDTA > 0.1N HNO₃ > 0.1N CH₃COONa

Table (7): Desorption of Th(IV) ions from zeolitic tuff.

Eluting agents	%Recovery first portion	%Recovery second portion	%Recovery third portion	%Recovery fourth portion	%Recovery fifth portion	%Cumulative recovery
0.1N HNO ₃	4.0	3.5	3.5	1.9	1.7	14.6
0.1N H ₂ SO ₄	-	-	-	-	-	-
1*10 ⁻⁴ N EDTA	11.0	8.5	8.3	7.6	5.4	40.8
0.1N EDTA	-	-	-	-	-	-
0.01N EDTA	4.3	3.7	3.6	3.6	3.2	17.5
0.001N EDTA	8.9	7.2	5.1	2.3	1.5	25.0
0.1N NaC ₂ H ₃ O ₂	7.1	2.9	0.4	0.0	0.0	10.4

Table (8): Desorption of U(VI) ions from zeolitic tuff.

Eluting agents	%Recovery first portion	%Recovery second portion	%Recovery third portion	%Recovery fourth portion	%Recovery fifth portion	%Cumulative recovery
0.1N HNO ₃	10.5	8.5	2.9	2.9	2.3	27.1
0.1N H ₂ SO ₄	10.5	7.9	5.4	2.8	2.8	29.4
1*10 ⁻⁴ N EDTA	8.0	5.2	3.5	3.0	2.0	21.7
0.1N EDTA	-	-	-	-	-	-
0.01N EDTA	2.3	2.1	1.7	0.5	0.3	6.9
0.001N EDTA	5.7	3.9	2.4	1.2	0.7	13.9
0.1N NaC ₂ H ₃ O ₂	9.1	7.3	4.2	3.6	3.3	27.5

While the following trend was observed for eluting agents of U(VI) from zeolitic tuff:

0.1N H₂SO₄ > 0.1N CH₃COONa > 0.1N HNO₃ > 1*10⁻⁴N EDTA > 0.001N EDTA > 0.01 N EDTA.

It can be noticed that the best desorption for Th(IV) was observed for 1×10^{-4} N EDTA, but the best desorption for U(VI) was observed for 0.1N H_2SO_4 .

Desorption yield for zeolitic tuff decreased with increasing the desorption stages (Akyil and Yusan, 2008). When concentration of EDTA is increased, desorption of Uranium(VI) and Thorium(IV) decreased. Thorium sulfate precipitated in the column ($K_{sp} = 9.6 \times 10^{-15}$) while Uranium(VI) form two successive soluble complexes with sulfate



Stability constant ($\log \beta_M$) for equation (14) equal 1.96 ± 0.06 but stability constant ($\log \beta_M$) for equation (15) equal 2.97 ± 0.03 (Tian and Rao, 2008).

4. Conclusion

The used size fraction (250-500 μm) of Tulul al-Shabba zeolitic tuff from Jordan is dominated by phillipsite and chabazite. The sorption behavior of the used samples towards Uranium(VI) and Thorium(IV)⁺ metal ions has indicated high initial rate of metal ions uptake. This study recommends the use of Jordanian zeolitic tuff to remove Uranium(VI) and Thorium(IV) from acidic solution in the expected mining or purification processes. Further work should be carried to enhance the desorption of Uranium(VI) and Thorium(IV) from zeolitic tuff.

References

- [1] Akyil, S., and Yusan, S., 2008. Sorption of Uranium (VI) from Aqueous Solutions by Akaganeite, Journal of Hazardous Materials, 160: 388-395.
- [2] Ali, A., and El-bishtawi, R., 1997. Removal of Lead and Nickel Ions Using Zeolite, J. of Chem. Tech. Biotech, 69: 27-34.
- [3] Dubinin, M. M., L. V. Radushkevich., and Dokl. Ak., 1947. A Theoretical Isotherm for Adsorption on Heterogeneous Surface, Nauk SSSR, 55: 331- 333.
- [4] Duvarcı, Ö., Akdeniz, Y., Özmişçi, F., Ülkü, S., Balköse., and M. Çiftcioğlu, M., 2006. Thermal Behavior of a Zeolitic Tuff, Ceramics International, 33: 795-801.
- [5] Eral, T.Z., and Hicsonmez, M. U., 2008. Adsorption of Thorium from Aqueous Solutions by Perlite, Journal of Environmental Radioactivity, 2: 1-5.
- [6] Fendorf, S.E., and Li, G., 1996. Kinetics of Chromate Reduction by Ferrous Iron, Environ. Sci. Technol, 30: 1614-1617.
- [7] Freundlich, H., 1932. Of the adsorption of gases. Section II. Kinetics and energetics of gas adsorption. Introductory paper to section II, Trans, Faraday Soc, 28: 195 - 201.
- [8] Harvey, D. 2000. Modern analytical chemistry. 1st Ed., McGraw-Hill, U.S.A.
- [9] Ho, Y.S., and McKay, G., 1998. Sorption of Dye from Aqueous Solution by Peat, J.
- [10] Chem. Eng, 70: 115–124.
- [11] Hunt, J.P. 1965. Metal Ions in Aqueous Solutions. 2nd Ed., Benjamin Inc, New York. Kaygun, A., and Akyil, S., 2007. Study of the Behavior of Thorium Adsorption on PAN / Zeolite Composite Adsorbent, Journal of Hazardous Materials, 147: 357-362.
- [12] Khaled, M. M., and Khalili, F.I., 1999. Solvent Extraction of Uranium(VI) by Didodecylphosphoric acid, Science and Technology, 4: 15-21.
- [13] Khalili, F., Al-Taweel, S.A., Yousef, Y.Y., and Al-Tarawneh, S.A., 2008. Synthesis, Characterization and Solvent Extraction Properties of New Thiophene Based Trifluoromethyl-Substituted β -Diketones for Thorium (IV) and Uranium (VI) Ions, Journal of Saudi Chemical Society, 12(2): 165-176.
- [14] Khoury, H., Ibrahim, K., Ghir, A., and Ed-Deen, T. 2003. Zeolites and zeolitic tuff in Jordan. Published by the University of Jordan, amman - Jordan.
- [15] Khoury, H. 2006. Industrial rocks and minerals in Jordan. 2nd Ed., Published by the University of Jordan, Amman - Jordan.
- [16] -Kilislioglu, A., and Bilgin, B., 2003. Thermodynamic and Kinetic Investigation of Uranium Adsorption on Amberlite IR-118-H Resin, Appl. Radiat. Isot, 50: 155 - 170.
- [17] Konodo, K., Momoto, K., and Nakashio, T., 1989. Equilibrium of Solvent Extraction of Lanthanides with Didodecylphosphoric, Solvent Extraction and Ion Exchange, 7(6): 1027-1041.
- [18] Krestou, A., Xenidis, A., and Panias, D., 2003. Mechanism of Aqueous Uranium(VI) Uptake by Natural Zeolite Tuff, Minerals Engineering, (16):1363-1370.
- [19] Lazaridis, K., Peleka, N., Karapantsios, D., and Matis, A., 2004. Copper Removal from Effluents by Various Separation Techniques, Hydrometallurgy, 74: 149-156.
- [20] Lee, D.C., Park, C.J., Yang, J.E., Jeong, Y.H., and Rhee, H.J., 2000. Screening of Hexavalent Chromium Biosorbent Marine Algae, Biotechnol, 54: 445-448.
- [21] Misaelides, P., Godelitsas, A., Filippidis, A., Charistos, D., and Anousis, I., 1995. Thorium and Uranium Uptake by Natural Zeolitic Materials, Sci. Total Environ, 173/174: 237-246.
- [22] Nazzal, M.K. 2006. The Effect of Ionic Strength on the Extraction of U(VI) from Perchlorate, Nitrate and Phosphate Solution by Didodecylphosphoric acid(HDDPA), M. Sc. Thesis, The University of Jordan.
- [23] Polanyi, M., 1963. The potential Theory of Adsorption, Science, 141: 1010 – 1013.
- [24] Savvin, S. B., 1961. Analytical Use of Arsenazo(III) Determination of Thorium, Zirconium, Uranium and Rare Earth Elements, Talanta, 8: 673- 679.
- [25] Sinha, S.P. 1966. Complexes of the Rare Earths. 1st Ed., Pergamon Press, London.
- [26] Skoog, A. West, M. and Holler, F. 1994. Analytical Chemistry an Introduction. 6th Ed., John Vondeling, U.S.A.
- [27] Slejko, L. 1985. Adsorption Technology. Marcel Dekker, New York.
- [28] Tahir, S., and Naseem, R., 2006. Removal of a Cationic Dye from Aqueous Solution by Adsorption onto Bentonite Clay, Chemosphere, 63:1842–1848.
- [29] Tian, G., and Rao, L., 2009. Spectrophotometric and Calorimetric Studies of U(VI) Complexation with Sulfate at 25C° to 70C°, J. Chem. Thermodynamics, 41: 569-574.
- [30] Ünlüa, N., and Ersoz, M., 2006. Adsorption Characteristics of Heavy Metal Ions onto a Low Cost Biopolymeric Sorbent from Aqueous Solutions, J. Hazard. Mater, B136: 272–280.



الجامعة الهاشمية



المملكة الأردنية الهاشمية

المجلة الأردنية
لعلوم الأرض والبيئة

JJEES

مجلة علمية عالمية محكمة

العدد الخاص

<http://jjees.hu.edu.jo/>

ISSN 1995-6681

المجلة الأردنية لعلوم الأرض والبيئة

مجلة علمية عالمية محكمة

المجلة الأردنية لعلوم الأرض والبيئة : مجلة علمية عالمية محكمة أسستها اللجنة العليا للبحث العلمي في وزارة التعليم العالي والبحث العلمي، الأردن، وتصدر عن عمادة البحث العلمي والدراسات العليا، الجامعة الهاشمية، الزرقاء، الأردن.

هيئة التحرير

رئيس التحرير

الأستاذ الدكتور عبد الرحيم أحمد حمدان
الجامعة الهاشمية، الزرقاء، الأردن.

الأعضاء

الأستاذ الدكتور سامح غرايبة
جامعة اليرموك.
الأستاذ الدكتور أحمد أبو هلال
جامعة اليرموك.
الأستاذ الدكتور عيسى مخلوف
الجامعة الهاشمية.

الأستاذ الدكتور عبد القادر عبد
الجامعة الأردنية.
الأستاذ الدكتور هاني خوري
الجامعة الأردنية.
الأستاذ الدكتور زهير العيسى
الجامعة الأردنية.

فريق الدعم

تنفيذ وإخراج

الدكتور وائل زريق م.أسامة الشريط

المحرر اللغوي

ترسل البحوث إلى العنوان التالي:

رئيس تحرير المجلة الأردنية لعلوم الأرض والبيئة
عمادة البحث العلمي والدراسات العليا
الجامعة الهاشمية

الزرقاء ١٣١٣٣ - الأردن

٠٠٩٦٢ فرعي ٤١٤٧ هاتف : ٣٩٠٣٣٣٣

Email: jjees@hu.edu.jo

Website: www.jjees.hu.edu.jo